12-2020

Water-Soluble Polymers with Ceramic/Metal Nanoparticles for Use as Anode Materials in Lithium-Ion and Sodium-Ion Batteries

Roberto Orrostieta Chavez
The University of Texas Rio Grande Valley

`

WATER-SOLUBLE POLYMERS WITH CERAMIC/METAL NANOPARTICLES FOR USE

AS ANODE MATERIALS IN LITHIUM-ION AND SODIUM-ION BATTERIES.

A Thesis

by

ROBERTO ORROSTIETA CHAVEZ

Submitted to the Graduate College of
The University of Texas Rio Grande Valley
In Partial Fulfillment of the Requirements for the Degree of

MASTER OF SCIENCE IN ENGINEERING

December 2020

Major Subject: Mechanical Engineering

WATER-SOLUBLE POLYMERS WITH CERAMIC/METAL NANOPARTICLES FOR USE

AS ANODE MATERIALS IN LIBS AND SODIUM ION BATTERIES.

A Thesis
by
ROBERTO ORROSTIETA CHAVEZ

COMMITTEE MEMBERS

Dr. Mataz Alcoutlabi
Committee Chair

Dr. Karen Lozano
Committee Member

Dr. Horacio Vasquez
Committee Member

Dr. Robert Jones
Committee Member

December 2020

`

`

ABSTRACT

Orrostieta Chavez, Roberto., <u>Water-Soluble Polymers with Ceramic/Metal Nanoparticles for Use as Anode Materials in Lithium-Ion and Sodium-Ion Batteries.</u> Master of Science (MS), December 2020, 110 pp, 9 tables, 49 figures, 136 references, 78 titles.

Aqueous solutions of poly(vinylpyrrolidone) (PVP) with 20, 25, and 28 wt.% concentrations were successfully spun into fibers by centrifugal spinning. The pristine PVP fibers were annealed and carbonized to produce flexible carbon fibers for use as binder-free anodes in lithium-ion and sodium-ion batteries. These flexible carbon fibers were prepared by developing a novel three-step heat treatment to reduce the residual stresses in the pristine PVP precursor fibers and to prevent fiber degradation during carbonization. The average diameters of the pristine, annealed, and carbonized fibers were obtained using scanning electron microscopy (SEM), which showed that the average diameter of the carbon fibers increased with increasing polymer concentration. Thermal characterization of the pristine and annealed fibers was carried out by thermogravimetric analysis (TGA). The TGA results showed that the annealed fibers yielded a residual mass percentage of 36.0 % while the pristine PVP fibers suffered a higher mass loss and only retained 26.5% of the original mass above 450 °C in an inert gas. The electrochemical performance of the carbon-fiber anodes was evaluated by conducting galvanostatic charge/discharge cycles, rate performance, cycle voltammetry experiments, and impedance tests. The 20, 25, and 28 wt.% derived binder-free anodes were tested in Li-ion and Na-ion half-cells.

`

TiO$_2$/C and Sn/C composite fibers were prepared by the centrifugal spinning of TiO$_2$/PVP and Sn/PVP solutions and subsequent heat treatment.

The successful preparation of centrifugally spun composite fibers from aqueous solutions was only achieved with TiO$_2$. Based on existing results in the literature, a higher vapor pressure leads to faster solvent evaporation and promotes fiber formation. Thus, a mixture of 1:1 water:ethanol (wt./wt.) was used to prepare the Sn/PVP precursor fibers as well as TiO$_2$/PVP precursor fibers. Nonetheless, the centrifugally spun Sn/C and TiO$_2$/C composite fibers prepared with the PVP/water/ethanol precursor solutions had a larger average diameter than those prepared from PVP aqueous solutions, which affected their electrochemical performance. In order to understand the constraints impeding the formation of Sn/C composite fibers from aqueous solutions, the viscosity and surface tension of aqueous Sn/PVP and TiO$_2$/PVP precursor solutions were investigated using a programable rheometer (BROOKFIELD, RVDV-III U) and Goniometer, Kyowa-DropMaster, respectively. The results showed that the addition of particles to the PVP aqueous solutions did not play a significant role in the viscosity nor the surface tension of the PVP aqueous solutions. Thus, other causes such as particle dispersion were investigated. It was observed that an inferior particle dispersion was obtained in water when compared to that in ethanol. Finally, alternative methods to produce composite fibers from polymer aqueous solutions are discussed for future research endeavors

`

DEDICATIONS

This work, every achievement leading up to this moment, and any new endeavors I venture in are dedicated to my family. You will always be the most precious people to me.

`

ACKNOWLEDGMENTS

My research work could not have been possibly done without the guidance and support of my committee chair, Dr. Mataz Alcoutlabi. I am thankful for his mentoring, patience, and wiliness to share knowledge. He truly is a role model hard working person passionate about his work. I am also thankful to my committee members, Dr. Karen Lozano, Robert Jones, and Dr. Horacio Vasquez, for their feedback, guidance, and support with my research and academic progress. I had the opportunity to attend classes with each of them and truly became inspired and motivated to learn in each of their classes. I am also very grateful to Dr. Victoria Padilla. I could not fit in a single page the many skills and ideas I learned from her. She is a great leader and role model for all of us in the PREM group. To my research group, Ramiro Gonzales, Jonathan Ayala, and Gabriel Gonzales, I would like to thank you for lifting me up even on the most adverse days. I could not have asked for better laboratory mates and friends.

TABLE OF CONTENTS

`

`

LIST OF TABLES

LIST OF FIGURES

`

xiii

CHAPTER I

INTRODUCTION

In today's modern society, up to 68% of the world's energy supply is derived from fossil

fuels (coal (42%), natural gas (21%), and oil (5%)) while only 3% is generated by renewable

energy technologies and the remaining 29% energy percentage is divided between nuclear

(14%), and hydro (15%) energy production methods [1]. However, there are several reasons why

society should walk away from fossil fuels as its main source of energy. For example, green

gasses generated from fossil fuels deteriorate air quality, harming the health of those exposed to

it, and increase the Earth's temperature (Global Warming) [2]. In order to overcome challenges

such as the ever-growing energy demand, the increasing scarcity of non-renewable fossil fuels,

and the negative environmental impact of these energy sources, environmentally friendly

alternatives are being improved (solar cells, wind turbines, etc.) [1]. Nonetheless, to fully achieve

the positive impact of these renewable energy sources, energy storage technology must

ambitiously progress alongside renewable energy technologies to fulfill the aspiration of a

cleaner energy production industry. A potential candidate for electrical energy storage is lithium-

ion batteries (LIBs). LIBs are already vastly adopted in applications such as consumer

electronics and, more recently, electric vehicles because of their high energy density and long

cycle stability [3].

Perhaps, one of the best examples of the implementation of LIBs for renewable grid energy storage is the "energy farm" in South Australia. In 2007, Tesla and Neoen partnered to construct the world's largest LIB (100 MW, 129 MWh) [4]. A simulation study on the deployment of stored energy in Australia shows that energy storage can reduce the levelized cost of electricity by 13 - 22% and reduce energy spillage by 76% [4]. It is evident that storage devices, such as LIBs, can help with energy regulation, contingency reserves, and adaptability from peak to off-peak periods. However, the relatively low abundance, geometrically-constrained mineral reserves of lithium, and its high demand make the depletion of lithium sources a possibility within the foreseeable future [5], [1], [6], [7]. Because of this scarcity, potential ion alternatives such as sodium-ion (Na^+) are good candidates to replace lithium, especially in larger-scale battery applications. Sodium, in contrast to lithium, is widely recognized as an abundant and low-cost metal [5], [8]. For comparison, lithium is found in 20 parts per million (PPM) while Sodium is found in 23,600 PPM [9]. Unfortunately, sodium-ion batteries (SIBs) face intrinsic challenges due to the larger size of the sodium ion (0.98 Å radius) compared to that of a lithium-ion (radius of 0.69 Å) [10]. Such a larger size prevents intercalation of Na^+ with graphite anodes [5], [9]. Currently, work is being conducted to achieve the intercalation of Na^+ with graphite. For example, hard carbon (HC) is being extensively studied as a potential negative electrode for SIBs [9]. HC is non-graphitizable and has turbostratic domains spaced by curved graphene nanosheets that create larger interlayer spacings than the well-defined interlayer spacing in graphite (3.3 Å). Hence, the complex molecular-level structure of HC can reversibly accommodate large size ions such as Na^+ [11]. Moreover, composite materials are being developed to improve the electrochemical performance of SIBs. Among the approaches selected, composite fiber anodes have been explored in some detail. Conventionally, electrospinning is adopted to fabricate such

composite fiber at a laboratory scale. However, due to the low fiber production yield of this method ($< 0.3\frac{g}{min}$), higher fiber yield production methods such as centrifugal spinning ($1\frac{g}{min}$) have gained attention to effectively produce these composite materials at a larger scale [12]. Thus, this work strives to develop a high fiber yield procedure from aqueous precursor solutions via centrifugal spinning for use in LIB and SIBs.

1.1. Objectives & Contributions

Composite materials have enabled engineers to pursue technologies otherwise limited by material performance. Substantial improvements in material properties (e.g., mechanical, thermal, electrical, etc.) can be achieved by the addition of fillers in polymer matrices [13]. Due to their high surface area to volume ratio, composite nanofibers have been extensively used in applications such as biomedical, filtration, tissue engineering, and energy storage [14], [15], [16], [17]. In particular, carbon fibers prepared by electrospinning and subsequent heat treatment of polymer-fiber precursors have been widely used in energy storage applications [18]. The carbon phase in these carbon fibers (CFs) can be either amorphous or graphitic, depending on the heat treatment performed during the carbonization process. Graphite is the commercially available anode material for lithium-ion batteries (LIBs) due to its low working potential, long cycle life, and low cost. However, the low theoretical capacity of the graphite anode (372 mAh g^{-1}) fails to satisfy the increasing demand for high-performance LIBs, particularly for hybrid and electric vehicles [19]. Li-alloys embedded in flexible CFs with amorphous carbon can be directly used as binder-free anodes in LIBs. The flexible amorphous carbon phase can buffer the volume change of the Li-alloy phase [19]. In addition, amorphous carbon fibers with many structural defects can accommodate more Li$^+$ than the ordered lattice in graphite [20]. Composite CFs can be prepared to contain ceramic and/or metallic fillers and can be directly used as anode materials in LIBs

3

with improved electrochemical performance such as rapid Li^+ diffusion, long cycle life, and high

specific capacity. Currently, polyvinylpyrrolidone (PVP), polyvinyl alcohol (PVA), and

polyacrylonitrile (PAN) are the most used polymer precursors to produce carbon fibers for LIB

applications [21]. Among these, PAN is the most exploited polymer to produce CFs due to its

high melting point and high carbon yield of more than 80% [22], [23]. Centrifugally spun PAN-

derived CF anodes have delivered a steady charge capacity (Li-disinsertion) of 297 mAh g^{-1} after

100 cycles at 100 mA g^{-1} [24]. Unfortunately, PAN has a high cost [25] and its most frequently

used solvent, dimethylformamide (DMF), has been linked to cancer and birth defects [26].

Nevertheless, the demand for CFs continues to increase. Therefore, researchers and industry

need to turn their attention to less hazardous and more environmentally benign carbon precursors

such as PVP and PVA. Both PVP and PVA, in contrast to PAN, are water-soluble and have been

used in energy storage applications [23], [26], [12], [27], [28], [29]. However, PVA has a

relatively lower carbon yield and in the case of PVP severe shrinkage is observed after

carbonization [28, 30] [26]. PVP is considered a potential carbon precursor alternative due to its

low cost and higher carbon yield (~87). Electrospun CFs derived from PVP have delivered a

reversible specific capacity as high as 450 mAh g^{-1} at the 100th cycle [23]. Moreover, high

production rates of PVP fibers have been achieved via the centrifugal spinning of PVP/ethanol

solutions [27, 28].

There are reports about the successful preparation of composite CFs derived from aqueous

PVA solutions. For example, Si/C composite-fiber anodes prepared by the centrifugal spinning

of aqueous Si/PVA precursor solutions and subsequent heat treatment delivered a steady capacity

of 758 mAh g^{-1} after 50 cycles, while PVA-derived CFs delivered 178 mAh g^{-1} [12]. [26].

Although the centrifugally spun PVA fibers had smaller diameters than centrifugally spun PVP

fibers, the lower fiber yield of aqueous PVA solutions during centrifugal spinning could become a challenge for the adoption of PVA-based carbon fibers at a large-scale. PVP, on the other hand, has a much higher fiber yield than PVA during centrifugal spinning, and, to the best of our knowledge, there have not been studies on the use of centrifugally spun CFs derived from aqueous PVP precursor solutions for use as anodes for LIBs nor SIBs. However, hematite α-Fe_2O_3 short fibers have been synthesized from centrifugally spun aqueous PVP/Fe $(NO_3)_3 \cdot 9H_2O$ precursor solutions and implemented in PAN/DMF solutions to fabricate Fe_3O_4/C composite-fiber anodes for LIBs [31]. These Fe_3O_4/C composite fiber anode delivered a capacity of 505 mAh g^{-1} at the 100th cycle at 100 mA g^{-1} [31]. The synthesized α-Fe_2O_3 short fibers had a hollow multiwalled structure with a wall thickness of 55 ± 15 nm and an outer diameter of 850 ± 90 nm, suggesting the feasibility of the successful CFs with hollow structures derived from PVP aqueous solutions [31]. PVP is less commonly used to produce CFs due to its large volume shrinkage after carbonization [30]. However, it has been shown that the carbon yield from PVP can be increased by adopting a more complex heat treatment [22], [32]. This study strives to maximize the production of CFs by optimizing the PVP concentration in aqueous solutions for centrifugal spinning and implementing a novel heat treatment that aims to decrease the large volume shrinkage observed in PVP fibers at higher carbonization temperatures. Based on the results obtained in this work, a feasible pathway towards large-scale production of CFs from 100% aqueous PVP solutions can be achieved via centrifugal spinning and subsequent three-step heat treatment.

CHAPTER II

LITERATURE REVIEW

The following subsection will introduce the working principle on metal-ion batteries, a description of the use of composite fiber electrodes, and the working mechanisms of the materials used as anodes in LIBs and SIBs.

2.1. Working Principle of Metal-Ion Batteries

The main active components in a LIB include the cathode, anode, electrolyte, and separator. These components are shown in the schematic in Fig. 1.
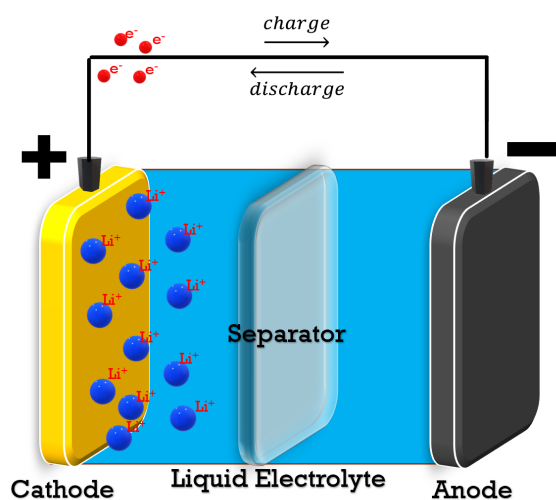
Fig. 1. Schematic of active components in lithium-ion batteries.

During the charging process, Li-ions move from the cathode, through the ionically conductive electrolyte, and react with the active material in the anode. During discharge, the Li-ions move back to the cathode passing once again through the separator, which is permeable to

ionic flow but prevents short-circuits in the battery from direct contact of the electrodes [33], [34], [35]. The working principle of SIBs is similar. The main difference is that the cathode is composed of sodium-containing layered oxides (Na_xCoO_2 where Na^+ is the ion moving between the electrodes [2], [9] [36].

The most used cathode materials in LIBs are $LiCoO_2$ and $LiFePO_4$, which are commercially available in the form of a slurry dispersed on a collector (aluminum foil) [37]. Similarly, anode materials, such as the commercially available graphite, can be prepared in slurry form and coated on a copper current collector (copper foil). Graphite remains the dominant anode material for LIBs, because of its flat potential profile, high coulombic efficiency, and good cycling performance. However, alternative anode materials with theoretical capacities higher than that of graphite (372 mAh g^{-1}) are being studied to satisfy the demand for superior energy storage devices. Slurry-based anodes possess the advantage over binder-free anodes of being loaded with higher percentages of active materials that determine the energy density of the electrode. Moreover, a conductive agent that improves the transport of electrons (e.g., carbon black), and a polymer binder that maintains the slurry paste adhered to the current collector are added to the active material to improve the performance of the electrode [1]. Homogeneous slurries can be prepared with a high loading of active material (>70%) and dispersed on the copper collector. Nonetheless, slurry-based electrodes face challenges of their own. If a binder does not maintain the slurry in contact with the current collector, the active material will gradually lose physical contact with the current collector [38]. Loss of physical contact is usually caused by the volume change during the insertion/disinsertion of Li^+ into the anode. In slurry-based anodes, the nanostructure of the active material can be modified to buffer any volume change of the electrode. Nanofibers, on the other hand, can endow active materials with

enhanced matrix nanostructures in which they are dispersed to further improve the volumetric buffering capabilities of the anode. Thus, composite fibers with high active material loading and good dispersion in the carbon-fiber matrix can result in binder-free anodes with improved electrochemical performance compared to slurry-based anodes. Centrifugal spinning (CS) has proven to be capable of producing beneficial structures such as hollow and porous fibers that facilitate Li^+/Na^+ transport, shorten electron pathways, and buffer volume changes [39], [40], [41], [42].

Separators based on composite fibers can also be fabricated from nonwoven nano/microfibers. Several factors must be considered when designing a separator. Some key requirements include minimal ionic resistance, mechanical and dimensional stability, and electrolyte uptake [33], [34]. Currently, polyolefin microporous membranes are the separators used in commercial LIBs because of their electrochemical stability, adequate thickness, and good mechanical strength [43], [44]. However, polyolefin separators are known for poor wettability and dimensional instability at elevated temperatures; such dimensional instability could eventually lead to internal short-circuiting and thermal runaway [33], [43], [44]. Thus, research is also being conducted to overcome these issues by using nonwoven nanofibers as separator materials.

Another important aspect that determines the performance of electrodes is the solid electrolyte interphase (SEI). When carbon intercalates with lithium, exposed carbon reacts with the electrolyte to form an ionically conductive passivation layer known as solid electrolyte interphase (SEI) [45], [46]. Most of the SEI layer forms during the first cycle (formation cycle) in which not only the constituents of the anode material are consumed, but also Li-ions [46]. Mitigating the effect of the SEI layer formation on the irreversible capacity and electrochemical

8

performance of metal-ion batteries has been a challenge to overcome by the scientific community [46]. Nanostructured materials with high surface area, such as carbon nanofibers, can produce a thin and stable solid electrolyte interface (SEI) layer which can result in electrodes with high charge-discharge rates, thus improving the specific power and energy density of the battery [19]. Another aspect that causes the formation of SEI is the use of anode materials with lower working voltage than the electrolyte used in the battery. The lower and upper working voltages of electrolytes are known as the lowest unoccupied molecular orbital (LUMO) and the highest occupied molecular orbital (HOMO), respectively. For commercial organic electrolytes such as dimethyl carbonate/diethyl carbonate (DMC/DEC), the LUMO and HOMO have values of 1.2 and 4.2 eV, respectively [47]. When the working voltage of an anode is below the LUMO of the electrolyte, such as in the case of graphite (0.2 V vs Li/Li$^+$) and DMC/DEC, the electrolyte will be reduced to reach the anode's working voltage and form SEI in the process [3]. In carbon fibers, the low working voltage can be ameliorated by introducing active materials with a higher working voltage. Some examples of these materials are introduced in the following sections. Also, the application of nanofibers in metal-ion batteries will be further discussed.

2.2. Application of Nanofibers in Batteries

Flexible binder-free anodes can be prepared with active materials (e.g., nanoparticles) embedded in a carbon-fiber (CF) matrix to produce composite CFs. The use of these composite CFs can decrease the cost of battery fabrication because CFs can directly be used as binder-free anodes without the need for conductive fillers or a current collector (copper foil) [48]. Moreover, composite CFs have attracted attention due to their high surface-area-to-volume ratio and high-rate of Li$^+$ insertion when structural or surface defects are present [49], [50]. The specific surface area of the CFs can be enhanced by different preparation methods. For example, the fiber

9

morphology has been improved by the generation of pores, which can increase clearance space for volume change and Li$^+$ diffusion on the electrode surface [51]. Additionally, non-calcinated non-woven fibrous mats can also be used as battery separators [33]. To improve efficiency, the separator must feature small volume and high porosity [52]. Non-woven fibrous mats usually have a thickness between 100 to 200 μm and base density between 9 and 30 g cm^{-2} [53]. Fiber-based battery separators must have a fiber diameter smaller than 5 μm [53]. Fibers with a larger diameter can cause the presence of locally open spaces that could not properly prevent direct contact between the electrodes [53]. For this reason, non-woven membranes are used as a support layer for separators impregnated with gel polymer electrolytes [53] [46]. Nevertheless, fibers with diameters smaller than 5 μm can be prepared with current manufacturing technologies such as electrospinning and centrifugal spinning. PVDF is the most commonly used polymer in the preparation of separators, but polymers such as PAN and PMMA are also implemented to improve the thermal stability and mechanical strength of non-woven membrane separators [54], [55]. Moreover, composite nanofibers can also be prepared to improve the performance of nanofiber-based separator membranes. Some commonly added fillers to the polymer fiber matrix include Al_2O_3, SiO_2, and TiO_2 because these materials can increase mechanical strength, thermal stability, and ionic conductivity [44], [55].

2.3. Anode Materials for Metal-Ion Batteries

Graphite is the primary commercial anode material for LIBs owing to its flat potential profile, stable capacity during prolonged charge/discharge cycles, and high coulombic efficiency. However, graphite anode exhibit relatively low theoretical capacity (372 mAh g^{-1}) and low specific power caused by the low Li$^+$ diffusivity (10^{-8} cm^2 s^{-1}) [56]. Extensive research efforts have been made to overcome the deficiencies of graphite anodes. Metals, semimetals, metal

oxides, and metal sulfides have been proposed as alternative anode materials to address the challenges facing the commercial graphite anode. These materials are based on lithiation-delithiation mechanisms such as intercalation, alloying, and conversion reactions (23) [19]. The intercalation, alloying, and conversion reaction mechanisms, which determine the behavior of active materials during the charge/discharge cycles, will be discussed in the following sections. Then, an overview of other manufacturing methods to produce separator membranes and CFs will be provided.

2.4. Intercalation Reaction Anode Materials

Anodes based on the Li^+ intercalation-deintercalation reaction (e.g., graphite, layered structures of TiO_2, MoO_2, and metal sulfides such as MoS_2, WS, TiS_2, etc.) undergo a process in which the ions are incorporated as a guest within the host crystal lattice without destroying the active material structure [57]. Even though the limited intercalation sites lead to relatively low capacities, the intercalation mechanism is capable of retaining capacity over many cycles because it does not modify the structure of the host material [37]. Nonetheless, the insertion of ions results in a volume expansion, which ultimately leads to loss of contact between the active material and current collector [40]. In this regard, composite CFs possess an advantage since their conductive structure functions as a current collector as well. As an illustration of this mechanism, the intercalation reaction of Li^+ in graphite in a commercial LIB is illustrated in reactions (1), (2), and (3). During battery charging, Li^+ is released (oxidation reaction 1) from the cathode ($LiCoO_2$), travels through the separator aided by the electrolyte, and intercalates in to the graphite (reduction reaction 2) [58]. During battery discharging the opposite occurs. Here, the Li^+ intercalates within the graphite without altering its structure (reaction 3) [2].

11

Cathode:

$$LiCoO_2 \xrightleftharpoons[discharge]{charge} Li_{1-x}CoO_2 + xLi^+ + xe^- \quad (1)$$

Anode:

$$6C + xLi^+ + xe^- \xrightleftharpoons[discharge]{charge} Li_xC_6 \quad (2)$$

Overall:

$$LiCoO_2 + 6C \xrightleftharpoons[discharge]{charge} Li_xC_6 + Li_{1-x}CoO_2 \quad (3)$$
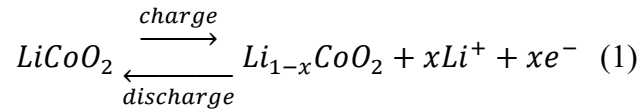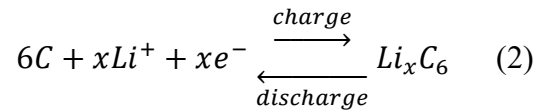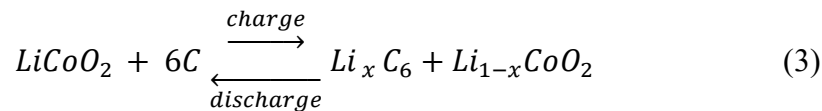
2.5. Alloying Reaction Anode Materials

Anode materials based on the alloying mechanism are not limited by their atomic framework; this allows this type of materials to host a larger number of Li-ions [37]. Since the ions break the bonds of the hosting material, higher specific capacities are achieved. Silicon, for example, is capable of forming metallic alloy phases such as $Li_{13}Si_7$, $Li_{13}Si_4$, $Li_{10}Si_3$, and $Li_{22}Si_5$, among others [59], with $Li_{22}Si_5$ (or $Li_{4.4}Si$) having a theoretical capacity of 4200 mAh g^{-1} [60]. Nonetheless, the addition of 4.4 Li-ions per Si atom leads to a volume increase greater than 400%. Hence, even though alloying reaction materials are in principle capable of offering higher specific capacities, their commercialization has been deterred due to their large volume changes occurring after repeated charge/discharge cycles.

Metal oxides can react with Li^+ via alloying, insertion, or conversion mechanisms. In alloying-based metal oxides, lithium oxide and metal are formed in the initial lithiation cycle. In

subsequent cycles the newly available metal alloys with lithium. For example, chemical reactions 4 and 5 show the alloying reaction of SnO_2 metal oxide.

$$SnO_2 + 4Li^+ + 4e^- \rightarrow Sn + 2Li_2O \qquad (4)$$

$$Sn + 2Li_2O + 4.4Li^+ + 4.4e^- \leftrightarrow Li_{4.4}Sn + 2Li_2O \qquad (5)$$
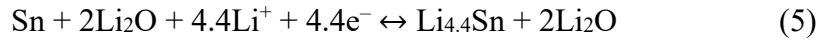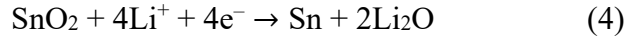
In this reaction, a steady reversible capacity is achieved once the formation of lithium oxide has been completed (reaction 1) by exhausting the oxygen in tin oxide [57], [60]. In the subsequent lithiation cycles, the newly formed inactive lithium oxide no longer reacts with the Li^+. However, Sn is now capable of alloying with the remaining available Li^+ supply (reaction 2).

Despite their large volume expansion, materials based on the alloying mechanism are extensively sought after because of their greater specific capacities. Multiple approaches have been explored to alleviate the strains caused by the volume expansion of the electrode. It has been shown that the large volume change is an intrinsic characteristic of materials that react based on alloying, and attempts to repress this volume change will come at the price of a lower capacity [61]. For composite CFs, one of the approaches used to allow volume expansion of silicon or other metalloids without highly increasing the overall anode volume is the production of porous or hollow structured nanofibers. For example, porous Sn/SnO_x nanoparticles have been successfully inserted in the pores within CFs [62]. This allows free space within the pore to be filled by the active material when it expands. In another example, Si nanoparticles were encapsulated in folded graphene cylinder-like structures [26]. The folded graphene network not only increased the overall conductivity of the CFs but also buffered the volumetric expansion of silicon that provoked mechanical stresses that in turn lead to the pulverization of fibers.

13

2.6. Conversion Rection Anode Materials

Transition metal oxide and metal sulfide anodes exhibit improved electrochemical performance compared to graphite anodes due to their redox catalytic properties [63]. Transition metal oxides based on a conversion mechanism (redox reaction) are of great interest for anode materials. During the conversion reaction, the formation of decomposed lithium oxide (Li_2O) is accompanied by the formation of metal nanoparticles via oxidation-reduction reactions [19]. This mechanism is illustrated in reaction 6 [64].

$$M_xO_y + 2_y\,Li \leftrightarrow yLi_2O + x \quad (6)$$
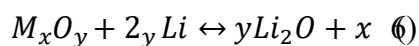
During a conversion reaction, the ability to partially reversibly decompose Li_2O back into a metal oxide leads to high reversible capacities and high energy densities [19]. Unfortunately, metal oxide anodes based on a conversion reaction mechanism suffer from low coulombic efficiency during the first cycle, unstable SEI layer formation, large potential hysteresis, and capacity fading during cycling [65].

CHAPTER III

STATE OF THE ART

3.1. Nanofibers Manufacturing Processes and Electrochemical Performance of Centrifugally Spun Composite Carbon Fibers

In this section, we discuss some of the top-down processing methods capable of producing fibrous structures for battery applications with emphasis on the centrifugal spinning method. These methods include melt blowing, biocomponent fiber spinning, phase invention, electrospinning, and centrifugal spinning. Short introductions to their production procedures and working mechanisms are presented with emphasis on the use of fibers in battery applications. A more detailed discussion is offered for the centrifugal spinning method since it is the selected method to fabricate carbon fibers in this work. Subsequently, a collection of all composite-fiber anodes for LIBs and SIBs prepared via centrifugal spinning is presented.

3.1.1. Melt Spinning

Melt blowing is a process in which a molten polymer is extruded through a small die and stretched by pressurized hot air to form microfibers (Fig. 2) [66]. The technology was first developed by the American Naval Research Laboratory and further designs such as Exxon's commercial-scale melt blowing mechanism emerged thereafter [67]. With this method, fibers with diameters ranging between 0.5 and 2 μm can be produced [67], [66].
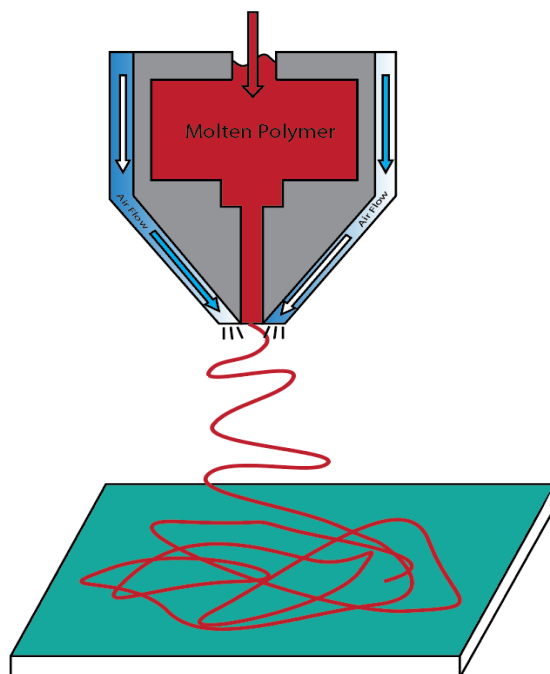
Fig. 2. Single-orifice melt-blowing process schematic.

One of the main advantages of melt blowing is that there is no need to use a solvent to liquify the polymer. For this reason, melt blowing can be a relatively low-cost manufacturing process to produce separators for metal-ion batteries [66]. The implementation of melt blowing has been proposed to fabricate thin, but strong, separators with materials such as polyesters, polyamides, and polymethyl pentene [68]. Of these polymers, polymethylpentene showed tolerance to high temperatures while polyester and polyamide exhibited excellent dimensional stability at high temperatures [68]. Finally, derived novel technologies are emerging to enable the production of nanofibers. An example is blow spinning. This hybrid approach combines electrospinning with melt-blown spinning. In this process, polymer solutions, with or without active materials, are prepared using volatile solvents. A high-speed airflow is then applied alongside a needle where the solution is being injected. The airflow forms the solution jet that ultimately forms fibers [69]. Although this method brings solvents back into the process, blow

spinning can produce fibers with a smaller average diameter than melt blowing, ranging from

100 to 1000 nm, thus making them appealing for battery applications [69].

3.1.2. Bicomponent Fiber Spinning

In the bicomponent fiber spinning process, two melted polymers are co-extruded through

a coaxial spinning head, or nozzle, to form filaments with designed cross-sectional profiles [70].

Fig. 3 shows a schematic of the fiber melt spinning line.
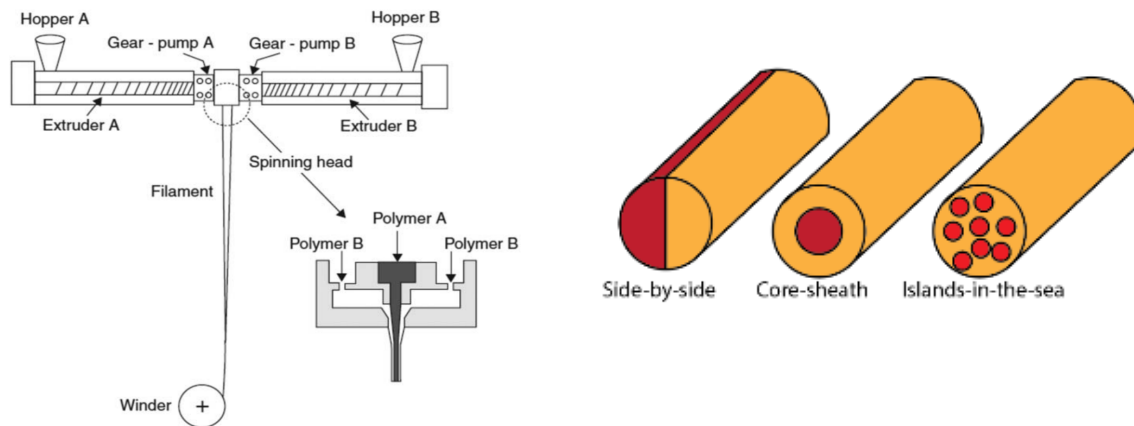
Fig. 3. Schematic of a bicomponent fiber melt spinning line [71].

Among the available cross-sectional profiles, side-by-side, core/sheath, and islands-in-

the-sea are the most common (Fig. 3) [71]. These profiles can be obtained by simply changing

the spinning head die. This versatility in cross-sectional profiles can potentially enable

optimization of fiber parameters such as mechanical strength, surface area, and thermal stability.

In battery applications, hollow and finned fibers (Fig. 4) are remarkably attractive since

they increase surface area. Thus, this processing method could also be explored to produce

nonwoven fiber membranes for use as battery separators. However, some challenges must be

overcome before achieving the manufacturing capability to produce these complex fiber profiles

for battery applications. To begin with, fibers with these cross-sectional profiles have a diameter

ranging between 0.5 to 20 μm [72] and, as mentioned before, fibers used as separators must have

an average diameter of less than 5 μm. These novel structures indeed increase the surface area of

the fibers, but they remain too large for battery applications. However, the reduction of their

dimensions for the benefit of battery applications is a goal worth exploring.
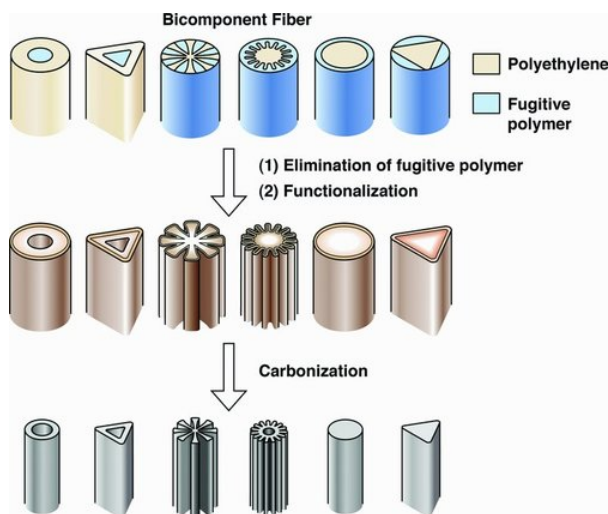
Fig. 4. Schematic describing the method for creating novel CF structures [72].

3.1.3. Phase Inversion

Phase inversion is a mainstream method to prepare membranes because it can

conveniently be adapted for large scale production [73]. However, it involves the implementation

of large amounts of organic solvents which are a safety hazard due to their toxic and/or

flammable nature [73]. The two main types of phase inversion are thermally induced phase

separation (TIPS) and non-solvent induced phase inversion (NIPS). During the TIPS process, a

thermodynamically unstable polymer solution forms two phases, one being polymer-rich and the

second being polymer-lean [74]. The phase separation process is induced by either cooling below

the binodal solubility curve or by adding an immiscible solvent to the solution [75]. After

removing the solvent and drying the polymer-rich and polymer-lean phases, a porous structure is

formed due to the difference in density between the two phases [74]. Similarly, during NIPS, a

homogeneous dope solution is exposed to a coagulation bath where the solution becomes

thermodynamically unstable. The unstable solution then traverses a binodal curve which leads to a polymer-rich and polymer-lean phases that become the membrane structure and pores, respectively [76]. Membranes manufactured via phase inversion are used in applications such as food industries, wastewater treatment, and energy storage. Recently, polymer fiber membranes have been developed by the NIPS method for use as separators in LIBs. For example, PVDF/PAN fibrous membranes have been produced via TIPS with controllable morphology (pore size), tensile strength, thermal stability, electrolyte uptake, and ionic conductivity via the composition of PAN:PVDF ratios [77]. In that work, the results showed that PAN:PVDF separators enhanced the resistance to shrinkage due to high temperatures (160 °C) although the ionic conductivity decreased from ~3.5 mS/cm in the 100% PVDF separator to ~2.0 mS/cm in the PVDF70/PAN30 blend. Moreover, the phase inversion process also enables the production of composite membranes such as Al_2O_3/PVDF-HFP, and PVDF/PAN/SiO_2 for battery separator applications [78], [79]. For these composite membranes, a PVDF70/PAN30 with 1 wt.% SiO_2 separator exhibited an improved ionic conductivity compared to the PVDF separator [79].

3.1.4. Electrospinning

The electrospinning process has been known since 1900 when it was first introduced by Cooley [80]. Electrospinning is capable of producing fibers with dimensions down to the nanoscale, but it was not until the 1990s that the nanotechnology field realized the potential of using nanofibers [81]. Today, the fabrication of nanofibers via electrospinning is broadly employed at the laboratory scale because of its simplicity, cost-effectiveness, and versatility [82]. Moreover, electrospinning possesses unique advantages such as improved dispersion and tangential alignment of nanowires and single-walled carbon nanotubes (SWCNTs) within the nanofibers [83]. During electrospinning, a high voltage is applied to a needle from which the

polymer solution (or melt) is drawn. The charge difference between the needle and collector induces tension forces that eject a thin solution thread and aligns nanofibers with 1D nanostructured active materials. Soon after the solution is ejected, the solvent evaporates and forms nanofibers in the form of a Taylor cone (Fig. 5) [35], [80]. For these reasons Electrospinning has been widely used to prepare composite membranes and composite CFs for applications in LIBs and SIBs [35], [84]. In the following section, centrifugal spinning will be discussed and compared to the electrospinning method.
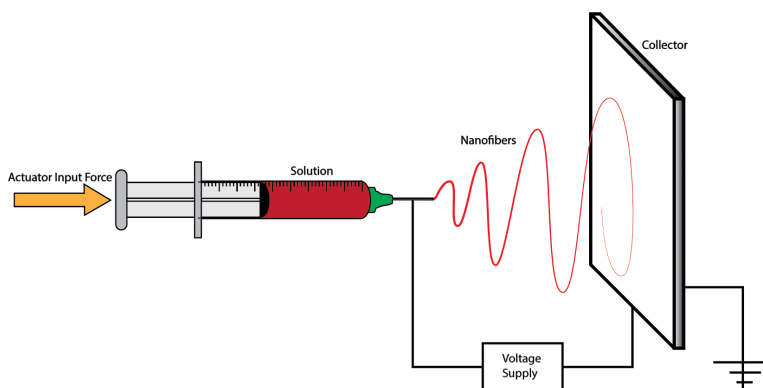
Fig. 5. Electrospinning set up.

3.1.5. Centrifugal Spinning

Centrifugal spinning (CS) is a low-cost and operationally safe manufacturing alternative that is gaining momentum in the production of fibers for multiple applications, mainly due to its much higher fiber yield [85], [86]. Moreover, CS overcomes some disadvantages that electrospinning faces such as the use of a high voltage (<10 kV) to stretch the fibers during processing, and solvent limitations due to insufficient dielectric constant [87], [24], [41]. In CS, centrifugal forces are applied to a polymer solution or melt, to overcome its surface tension and stretch the polymer droplet (jet) to form nanofibers [41]. The process begins when a fluid is loaded into a spinneret. Then, centrifugal forces are applied to the solution/melt at high rotational

speeds resulting in a polymer jet ejected from the needles attached to the arms of a spinneret. This curved jet is subsequently stretched by extensional forces to form thin fibers deposited on the collectors [85], [88], [41]. Finally, nonwoven fibers are collected in discrete steps to form a multilayered membrane. Fig. 6 shows the CS setup with the spinneret at the center and 8 collectors equally spaced around the spinneret.
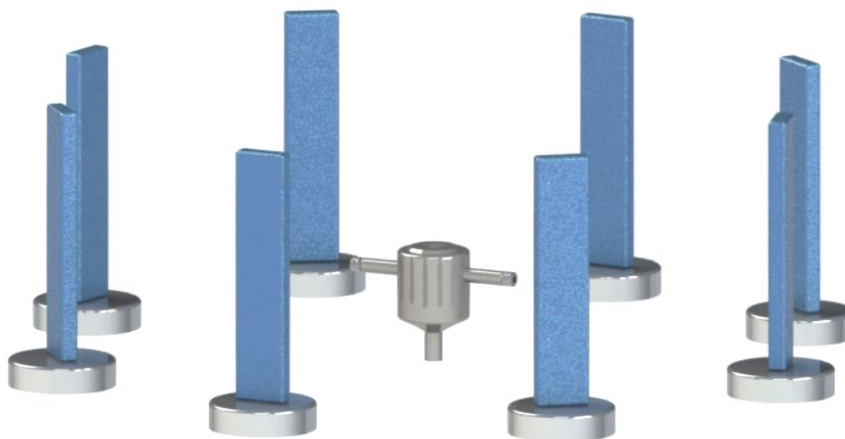
Fig. 6. Centrifugal spinning spinneret and collector schematic.

While parameters such as viscosity (polymer concentration) and evaporation rate (for solutions) play important roles in the production of both electrospun and centrifugally spun fibers [49] [88], temperature (for melts) and rotational speed are parameters that only apply for centrifugal spinning. These CS exclusive parameters enable researchers to have greater control over the centrifugally spun nanofiber structure. A further crucial difference between centrifugal spinning and electrospinning is that the drawing forces applied to the solution during centrifugal spinning are not affected by the collection distance as in the electrospinning method due to the distance-dependent voltage [88]. Thus, choosing the optimum collection distance for centrifugal spinning depends only on the solvent evaporation rate. If the fiber collection distance is small,

the diameter of the fiber will be larger but once the critical distance for solvent evaporation is reached, the collection distance becomes less relevant [88]. In CS, there is a critical rotational speed that must be reached to eject the solution from the spinneret. Furthermore, a second critical angular velocity exists after the solution jet has been initiated. This velocity is reached once the extensional forces on the solution jet have achieved steady-state forces. As a consequence of this constant pull, the solution exits the spinneret at a higher rate and the jet diameter is reduced well below that of the outlet nozzle [88].

It is important to note here that the elongation of the polymer jet during the centrifugal spinning of binary systems (polymer/solvent) can initiate phase separation. When the solution jet is formed and elongation begins, flash vaporization, decompression of the polymer solution, and cooling due to the consumption of heat during vaporization accompany the process [89]. During this process, the polymer jets become thermodynamically unstable and phase separation takes place by forming polymer-rich and solvent-rich phases [89]. In this aspect, this process can be considered a TIPS method, and evaporation of solutions with solvent mixtures can lead to porous structures due to phase separation. For solvent mixtures, the solvent with a higher vapor pressure evaporates more rapidly, leaving behind the solvent with lower vapor pressure. As the higher vapor pressure solvent evaporates, the lower vapor pressure solvent clusters and becomes the solvent-rich phase that eventually forms pores in the fibers [41]. In the case of a centrifugal spinning of polymer solutions containing solid nanoparticles, one can assume that if the particles are found in the polymer-rich phase, then this can result in the agglomeration of nanoparticles in the fiber matrix prevent lithiation with the active material. Similarly, particle agglomerations could be found in the solvent-rich phase, but in this case, the particles will be placed in the pores, which is beneficial for battery applications to reduce the volume expansion of the electrode.

3.2. Centrifugally Spun Anode Materials for Lithium-ion Batteries

The electrochemical design of anodic materials widely varies based on multiple parameters. Such parameters include coatings, nanoparticle addition, binder material. Etc. In the case of nanofiber production for anodic purposes, nanofibers saturated with metal, metal oxide, ceramic, and composite nanoparticles have seen an increased interest in recent years because of their attributes: controllable fiber diameter, high surface area – to volume ratio, low density and high pore volume [90]. Thus, In the following sections, the up-to-date materials added to centrifugally spun nanofibers to enhanced anodic performance in LIBs and SIBs will be presented.

3.2.1. Carbon Nanofibers for LIBs

Carbon nanofibers (CNFs), a nanostructured material have produced excellent cycling performance results after 50 cycles [91]. Carbon fibers can be prepared from different polymer precursor solutions or melts. Solutions made with polymers such as PAN, PVP, PVA, polyvinylidene fluoride (PVDF), among others [92], have been used as CFs precursors. Currently, 95 % of CFs are produced from PAN precursor nanofibers due to their high carbon yield after carbonization [93], [94]. When used in LIBs, carbon-fiber anodes prepared from centrifugally spun PAN precursor fibers have delivered a reversible capacity of 297 mAh g^{-1} after 100 cycles at 100 mAg^{-1} [24]. The performance of carbon nanofibers can be enhanced by adding additives such as metal oxides, metal sulfites, metal nanoparticles, ceramic nanoparticles, etc. In the following section, active materials used in LIBs are compiled and presented in groups based on their insertion mechanism.

3.2.2. Alloying Based Materials for LIBs

Common characteristics of alloying based materials include their high theoretical capacity accompanied by a large volume change during charge/discharge cycles, which can lead to anode fracture and crumbling. To retain the higher capacity offered by alloying based materials, volume buffering structures need to be implemented in centrifugally spun fibers. In general, two main methods have successfully achieved high capacities for highly expandable materials. One approach involves introducing pores in the fibers where the particles are placed. This clearance between the particles and fibers is filled by the expansion of the nanoparticles after lithiation, thus decreasing the overall volume change of the anode [95], [96], [97], [98]. The other method involves constraining the volume change of the particles by encapsulating them in a carbon matrix [26], [26], [99], [100]. These approaches can be implemented in the future to improve the electrochemical performance of centrifugally spun composite-fiber anodes for LIBs. Table 1 illustrates a list of alloy-based materials used in the preparation of composite-fiber anodes via CS for LIBs.

Table 1. Alloying based materials used in the preparation of composite carbon fibers via centrifugal spinning for use as anodes in LIBs.

Composite Fiber Anode Material	Polymer Precursor(s), Additive(s), and Solvent(s)	Spinning Conditions	Stabilization and Carbonization	Electrochemical Performance (tested at 100 mA g^{-1})	Reference
Si/C	14 wt.% PVA/DI water + 19% Si/DI water	5000 rpm for 5 min,	Partially carbonized by acid treatment followed by carbonization at 800 °C for 30 min.	758 mAh g^{-1} after 50 cycles	[12]
Sn/C	[12 wt.% PAN (15% Sn)]/DMF	8000 rpm	Stabilized at 280 °C for 5 hrs. and carbonized at 800 °C for 2 hrs.	715 and 724 mAh g^{-1} after 50 cycles for nano and microparticles, respectively	[24]
Sn/C	[12 wt.% PAN (15% Sn)]/DMF	8000 rpm	Stabilized at 280 °C for 5 hrs. and carbonized at 800 °C for 2 hrs.	675 mAh g^{-1} after 100 cycles with a ten minutes rest between each discharge cycle.	[90]
Sb/C	[4g PVB + 5g SbCl3]/40.0 mL methanol	Not Specified	Carbonized at 600 °C for 2 hrs.	315.9 mAh g^{-1} after 100 cycles	[101]
Sb/C	[4g PVB + 4g SbCl3]/40.0 mL methanol	Not Specified	Carbonized at 600 °C for 2 hrs.	254.4 mAh g^{-1} after 100 cycles	[101]
Sb/C	[4g PVB + 6g SbCl3]/40.0 mL methanol	Not Specified	Carbonized at 600 °C for 2 hrs.	131.1 mAh g^{-1} after 100 cycles	[101]

3.2.3. Transition Metal Oxide Materials for LIBs

Metal oxides can host Li-ions either by alloying, intercalation, or conversion. In some cases, metal-oxides exhibit a two-step reaction in which a conversion reaction first forms a lithium oxide layer, followed by the alloying mechanism (alloying or intercalation) of the transition metal. In this collection of materials, metal oxides comprise the largest group of materials implemented in centrifugally spun composite fibers. Table 2 shows a summary of the different materials prepared via CS and their electrochemical performance.

Table 2. Transition metal oxides used in the preparation of composite carbon fibers via centrifugal spinning for use as anodes in LIBs

Composite Fiber Anode Material	Polymer Precursor(s), Additive(s), and Solvent(s)	Spinning Conditions	Stabilization and Carbonization	Electrochemical Performance (tested at 100 mA g^{-1})	Reference
CuO/C	[12 wt.% PAN (15 wt.% CuO)]/DMF	7,000 rpm	Stabilized at 280 °C for 5 hrs. and carbonized at 700 °C for 2 hrs.	~ 160 mAh g^{-1} after 100 cycles	[102]
MoO$_2$/C	[12 wt.% PAN (50, 60, 70, and 80 wt.%. MoO$_2$)]/DMF	6,800 rpm	Stabilized at 280 °C for 5 hrs. and carbonized at 700 °C for 2 hrs.	629, 575, 597, 710 mAh g^{-1} during the first cycle, respectively.	[103]
Fe$_3$O$_4$/C	[12 wt.% PAN (15 wt.% FeACAC)]/DMF	7,000 rpm	Stabilized at 280 °C for 4 hrs. and carbonized at 600 °C for 6 hrs.	300 mAh g^{-1} after 100 cycles	[92]
TiO$_2$/C	[15 wt.% PVP (17:4 wt. ratio Titanium/PVP)]/[10:1 wt. ratio ethanol/acetic acid	7,000 rpm	Stabilized at 280 °C for 5 hrs and carbonized at 550 °C for 5 hrs.	228.9 mAh g^{-1} after 100 cycles	[27]
TiO$_2$/C	(5 g PVP + 3 g TBOT)/[40 mL methanol]	20,000 to 30,000 rpm (0.1 mm diameter aperture)	Dried at 60 °C for 12 h. Pre-oxidized at 300 °C for 2 h. carbonization at 600 °C for 2 h.	150 mAh g^{-1} after 200 cycles.	[104]
α Fe$_3$O$_4$/C	[28 wt.% PVP (2g Fe(NO$_3$)$_3$9H$_2$H)]/H$_2$O [12% wt. PAN]/DMF	7000-7500 rpm	PVP - Stabilization at 600 °C for 1 hr. PAN - Stabilized at 240 °C for 30 mins. and carbonized at 800 °C for 1 hr.	505 mAh g^{-1} after 100 cycles	[31]
Fe$_3$O$_4$/Fe$_3$C /C	(5 g PVP + 3 g Fe(acac)$_3$)/[40 mL methanol]	20,000 to 30,000 rpm (0.1 mm diameter aperture)	Dried at 60 °C for 12 h. Pre-oxidized at 300 °C for 2 h. carbonization at 600 °C for 2 h.	400 mAh g^{-1} after 200 cycles.	[104]

α-Fe$_2$O$_3$/ TiO$_2$/C	[15 wt.% PVP (1 g titanium (IV) butoxide, 1.5 g iron (III) acetylacetonate)]/ethanol/acetic acid (10:1)	7000 rpm	PVP – Stabilization at 200 C for 2 h carbonization at 550 °C for 5 h.	340 mAh g^{-1} after 100 cycles.	[14]
Fe$_3$O$_4$/Fe$_3$C /TiO$_2$/C	5 g PVP/[40 mL methanol + 3 mL TBOT]	20,000 to 30,000 rpm	Dried at 60 °C for 12 h. Pre-oxidized at 300 °C for 2 h. carbonization at 600 °C for 2 h.	700 mAh g^{-1} after 400 cycles	[104]
NiO/C	[12 wt.% PAN (15 wt.% NiO)]/DMF	7,000 rpm	Stabilized at 280 °C for 5 hrs. and carbonized at 700 °C for 2 hrs.	~ 200 mAh g^{-1} after 100 cycles	[102]
SnO$_2$/C	[12% wt.% PAN (15% SnO$_2$)]/DMF	7,000 rpm	Stabilized at 280 °C for 5 hrs. and carbonized at 700 °C for 2 hrs.	211 mAh/g after 50 cycles	[102]
SnO$_2$/NiO/ C	[12% PAN (15 wt.% Sn 2-ethylhexanoate, 10 wt.% Nickel (II) acetate tetrahydrate)]/D MF	8000 rpm	Stabilized at 280 °C for 5 hrs. and carbonized at 800 °C for 2 hrs.	633 mAh/g after 100 cycles with a ten minutes rest between each discharge cycle.	[90]
ZnO/C	[12 wt.% PAN (15 wt.% ZnO)]/DMF	7,000 rpm	Stabilized at 280 °C for 5 hrs. and carbonized at 700 °C for 2 hrs.	~ 235 mAh/g after 80 cycles	[102]

3.2.4. Transition Metal Sulfides Materials for LIBs

There are only two metal sulfide materials so far utilized in the production of composite carbon fibers via centrifugal spinning for LIB applications. Table 3 contains the materials discussed in the following subsections.

Table 3. Transition metal sulfides used in the preparation of composite carbon fibers via centrifugal spinning for use as anodes in LIBs

Composite Fiber Anode Material	Polymer Precursor(s), Additive(s), and Solvent(s)	Spinning Conditions	Stabilization and Carbonization	Electrochemical Performance	Reference
MoS_2/C	[12 wt.% PAN (80% MoS_2)] /DMF	Not Specified	Stabilized at 155 °C for 75 mins then Stabilized at 280 °C for 75 mins and carbonized at 810 °C for 1 hr.	250 mAh g^{-1} after 100 cycles (tested at 100 mA g^{-1})	[103]
TiS_2/C	[12 wt.% PAN (30 wt.% TiS_2)]/DMF	Not Specified	Stabilized at 280 °C for 5 hrs. and carbonized at 800 °C for 2 hrs.	250 mAh g^{-1} after 100 cycles (tested at 50 mA g^{-1})	[105]

3.2.5. Discussion on Composite Carbon Fibers for LIBs

Multiple nanostructures such as nanoparticles, quantum dots, nanorods, and nanosheets have been integrated into electrospun composite CFs since this has been the most adopted method used in laboratory research. However, there is plenty of room in CS for the implementation of active materials with different nanostructure configurations. In most cases, the capacity of the electrospun anodes is higher due to their smaller average diameter. However, future implementation of centrifugal spinning to fabricate fibers could help optimize the surface area of fibers and, in turn, improve the performance of the centrifugally spun fibers to match and exceed the performance of the more widely implemented electrospun fibers.

3.3. Centrifugally Spun Anode Materials for Sodium ion Batteries

3.3.1. Carbon Nanofibers for SIBs

Research to develop compatible materials for SIBs has seen increasing interest over recent years [106], [107], [108]. One of the major challenges is the larger ion size. Na$^+$ has an ion radius of 0.98 Å compared to the smaller Li$^+$ radius of 0.69 Å [10]. In fact, the smaller ion size of

Li$^+$ was the key parameter that stimulated a higher interest in LIBs when both materials were initially proposed [107]. Consequently, Na-ions are less capable to intercalate/alloy into the host material. SIBs with a graphitic anode exhibit low capacities of $\sim$ 35 mAh g^{-1} due to the sluggish intercalation of Na$^+$ into graphite [109]. CFs prepared by centrifugal spinning and subsequent thermal treatment have been prepared with the objective to alter the structure of the CFs and improve intercalation kinetics between Na$^+$ and carbon. The produced CFs were used as anodes in Na-ion half-cells and delivered a reversible capacity of 88 mAh g^{-1} after 100 cycles [28]. Even after modifying the structure of the CFs to favor Na$^+$ intercalation, the carbon-fiber anode delivered less than half the capacity of centrifugally spun CF anode for LIBs. Among the efforts to overcome the challenges that SIBs face, centrifugally spun composite fibers have been developed for use as anodes in SIBs.

3.3.2. Alloying Based Materials for SIBs

There are limited available results on the use of alloying based materials as precursors for centrifugally spun composite-fiber anodes in SIBs. The material composition, additives, heat treatments, and the electrochemical performance of these composite-fiber anodes are compiled in Table 4.

Table 4. Alloying based materials used in the preparation of composite carbon fibers via centrifugal spinning for use as anodes in SIBs.

Composite Fiber Anode Material	Polymer Precursor(s), Additive(s), and Solvent(s)	Spinning Conditions	Stabilization and Carbonization	Electrochemical Performance (tested at 100 mA g^{-1})	Reference
SnSb/C	[15 wt.% PAN (50 wt.% SnO2/Sb2O5)]/ DMF	Not Specified	Stabilized at 250 °C for 2.5 hrs. and carbonized at 700 °C for 2 hrs.	359 mAh g^{-1} after 50 cycles	[110]
SnSb/C	[15 wt.% PAN (100 wt.% SnO2/Sb2O5)]/ DMF	Not Specified	Stabilized at 250 °C for 2.5 hrs. and carbonized at 700 °C for 2 hrs.	345 mAh g^{-1} after 50 cycles	[110]
SnSb/C	[15% PAN (100 wt.% SnO2/Sb2O5)]/ DMF (Carbon Coated)	Not Specified	Stabilized at 250 °C for 2.5 hrs. and carbonized at 700 °C for 2 hrs.	781 mAh g^{-1} after 50 cycles	[110]
SnSb/rGO	[13 wt.% PAN (1:1: 2 wt. ratio Sn(CH3COO)/Sb(CH3COO)3/PAN)]/DMF (Carbon Coated)	4000 rpm	Stabilized at 280 °C for 2.5 hrs. and carbonized at 700 °C for 1 hrs.	324.5 mAh/g after 200 cycles (tested at 50 mA g^{-1})	[111]

3.3.3. Transition Metal Oxide Materials for SIBs

Only two metal oxide materials have been used in the preparation of composite-fiber anodes via CS for SIBs. Like in the case of alloying based materials, multiple material compositions, additives, or further treatments were involved. A concise list of this material configuration and their electrochemical performance results are collected in Table 5.

Table 5. Transition metal oxides used in the preparation of composite fibers via centrifugal spinning for use as anodes in SIBs.

Composite Fiber Anode Material	Polymer Precursor(s), Additive(s), and Solvent(s)	Spinning Conditions	Stabilization and Carbonization	Electrochemical Performance	Reference
SnO_2/C	[12 wt.% PAN (15% SnO_2)]/DMF	7,000 rpm	Stabilized at 280 °C for 5 hrs. and carbonized at 700 °C for 2 hrs.	198 mAh g^{-1} after 50 cycles (Tested at 100 mA g^{-1})	[102]
SnO_2 /C	Not Specified	Not Specified	Oxidized at 500 °C for 3 hrs.	158 mAh g^{-1} after 50 cycles (tested at 640 mA g^{-1})	[112]
SnO_2/C & SnO_2/C CVD treated	[13 wt.% PAN (40% $SnCl_2$)] /DMF	4000 rpm	Oxidized at 500 °C for 3 hrs. CVD for 30 60 and 90 mins.	71, 111, 158, 147 mAh g^{-1} after 30 cycles (tested at 40 mA g^{-1})	[113]
SnO_2/C & SnO_2/C CVD treated	[13 wt.% PAN (40% $SnCl_2$)] /DMF	4000 rpm	Oxidized at 500 °C for 3 hrs. CVD for 30 60 and 90 mins.	39, 99, 86, 100 mAh g^{-1} after 50 cycles. (tested at 640 mAh g^{-11})	[113]
MoO_2/C	[12 wt.% PAN (80% wt. MoO2)] /DMF	6,800 rpm	Stabilized at 280 °C for 5 hrs. and carbonized at 700 °C for 2 hrs.	~130 mAh g^{-1} after 100 cycles (tested at 100 mA g^{-1})	[103]

3.3.4. Discussion on Composite Carbon Fibers for SIBs

Compared to LIB anodes, there is more room for innovation in SIBs since not as many materials, fiber structures, or post carbonization treatments have been investigated. The following are some examples of electrochemical performance improvement of electrospun fiber anodes in SIBs by post carbonization treatments and the design of ternary composite materials. The centrifugally spun SnO_2/C composite anodes delivered a specific capacity of 198 mAh g^{-1} after 50 cycles at 100 mAg^{-1} [102]. On the other hand, electrospun fibers with partially reduced SnO_2 nanoparticles were embedded in carbon fibers followed by carbon coating and thermal reduction processes [114]. After 50 cycles at a current density of 100 mA g^{-1}, the SnO_2/C composite-fiber electrode delivered a high specific capacity of 536 mAh g^{-1} at 100 mA g^{-1} [114].

Also, centrifugally spun SnSb/C composite-fiber anodes yielded a capacity of 345 mAh g^{-1} after 50 cycles at a current density of 100 mA g^{-1} [110]. Similar experiments have been conducted by electrospinning. In a study, $SnCl_2$ and $SbCl_3$ were used as precursors for SnSb alloy. Moreover, TEOS was included in the solution as the silica precursor. All these precursors were homogenized in a PVP/DMF solution from which electrospun porous SnSb/SiO2/C CFs were obtained [115]. The incorporation of silica in the carbon matrix helped to buffer the volume change and maintained the structural integrity of the fibers [115]. The SnSb/SiO$_2$/C composite fiber anode exhibited a high specific capacity of 660 mAh g^{-1} at a galvanostatic current density of 200 mA g^{-1} after 100 cycles [115]. As one can observe for the SnSb binder-free anodes, the addition of TEOS resulted in a significant improvement in the electrochemical performance of electrospun composite fibers. These comparisons illustrate how further fiber treatments or ternary composites could also improve the performance of centrifugally spun composite fibers.

CHAPTER IV

METHODOLOGY

4.1. Material Characterization

The morphology of CFs was examined by scanning electron microscopy (SEM; Sigma VP

Carl Zeiss, Germany) coupled with an energy dispersive spectroscopy (EDS) system (EDAX,

Mahwah, NJ, USA) to investigate the elemental composition. To determine the average fiber

diameter, 300 measurements were taken, 60 per image, across a total of 5 different SEM images

scaled on ImageJ software. Similarly, the histograms were produced using the 300 randomly

selected measurements. Thermogravimetric analysis (TGA; 209 F3 Tarsus NETZSCH,

Germany) was conducted in air and nitrogen atmospheres to investigate the effect of annealing

on fiber degradation. Raman spectra of PVP powder and precursor nanofibers prepared from

aqueous PVP solutions of different concentrations (20, 25, and 28 wt. %) were obtained with a

Renishaw InVia confocal spectrometer operating at 785 nm. The surface tension of PVP

solutions was measured using Goniometer, Kyowa-DropMaster series. Finally, the viscosities of

PVP and composite precursor solutions were determined using a programable rheometer

(BROOKFIELD, RVDV-III U).

4.2. Electrochemical Testing

The electrochemical performance of the carbon-fiber anodes was evaluated using CR2032-type coin cells. CFs with a half-inch diameter were punched out and used directly as binder-free anodes. Lithium foil was used as the counter electrode in Li-ion half cells. Similarly, sodium cubes (fisher scientific) were used to prepare the sodium-chip counter electrode for half-cell SIBs. The weight of these anodes ranged between 4-9 mg. The Li-ion and Na-ion half cells (CR2032) were assembled in a glovebox (Mbraun, USA) under a controlled environment with high purity argon. Glass microfibers were used as the separator (9934-AH, Whatman Glass microfibers). 1 M $LiPF_6$ solution in ethylene carbonate (EC)/dimethyl carbonate (DMC) (1:1 v/v) was prepared and used as the electrolyte for LIBs. Sodium Perchlorate ($NaClO_4$) solution in ethylene carbonate (EC)/dimethyl carbonate (DMC) (1:1 v/v) was prepared and used as the electrolyte for SIBs. Cyclic voltammetry (BSC-810 Bio-logic, France) experiments were performed on Li-ion and Na-ion half cells at a rate of 0.1 mV s^{-1} between 0 and 3 V. Galvanostatic charge/discharge experiments were conducted at a current density of 100 mA g^{-1} from 0.05 to 3.0 V (CT2001A Landt, China). The rate performance was evaluated at current densities of 50, 100, 200, 400, 500, and 50 mA g^{-1} (BT 2000 Arbin, US). Electrochemical impedance spectroscopy (EIS) experiments were performed using an Autolab128N at a frequency range of 100 kHz to 0.1 kHz.

CHAPTER V

EXPERIMENTAL

5.1. Materials

Poly(vinylpyrrolidone) (PVP) with an average molecular weight (Mw) of 1,300,000 and

Ethanol (200 proof) were purchased from Sigma-Aldrich USA. Deionized (DI) water, 18 MΩ

cm, was produced in-house (Milli-Q, Millipore Ltd., U.K.). 1 M $LiPF_6$ salt and dimethyl

carbonate (DMC) were purchased from Alpha Aesar. Ethylene carbonate (EC) was purchased

from Sigma Aldrich. Commercial lithium-foil chips were purchased from MTI Corp. USA.

Sodium cubes immersed in mineral oil and Sodium Perchlorate ($NaClO_4$) were purchased from

fisher scientific. Titanium (IV) oxide (TiO_2 anatase, 99.7%, <25 nm,) was purchase from Sigma

Aldrich. Tin nanopowder (Sn, 99.9%, 60-80nm) was purchased from Us Research Nanomaterials

Inc.

5.2. Procedures

5.2.1. Carbon Fibers Preparation

The precursor fibers were prepared from 20g aqueous solutions with PVP concentrations

of 10, 15, 20, 25, and 28 wt.%. The solutions were homogenized by magnetic stirring at 70 °C

for 5 h. Solutions with concentrations of 25 wt.% or higher were subjected to an additional 5 h of

stirring to achieve complete homogenization. The PVP solutions were then spun in laboratory-

scale centrifugal spinning equipment (FiberRio Cyclone L-1000M). The spinneret was equipped

with 30-gauge regular bevel needles (EXELINT, U.S.A). A variety of spinneret rotational speeds

and spinning times were explored for each solution concentration. The centrifugal spinning parameters and solution properties used to prepare the PVP fibers are given in Table 6.

Table 6. Spinning parameters for the fabrication of centrifugally spun PVP fibers.

Polymer concentration (wt.%)	Rotational speed (rpm)	Spinning time (min)	Humidity during successful fiber yield (%)	Fiber formation
10	4000 – 9000	3 – 8	35 - 60	No
15	4000 – 9000	3 – 8	35 - 60	No
20	6000	4	< 40	Yes
25	9000	5	< 60	Yes
28	9000	8	< 60	Yes

Fibers were collected and subsequently annealed at 150 °C for 24 h, in air (1 °C/min) (ELF 11/6 Carbolite Gero, UK). They were left in air to reach room temperature and then placed in a tube furnace (OTF-1200X MTI Corporation, US) to be pre-oxidized in air at 270 °C for 4 h (1 °C/min) followed by carbonization in an Argon atmosphere at 700 °C for 3 h (5 °C/min).

5.2.2. Composite Carbon Fibers Preparation

For the preparation of the precursor solutions discussed in the following sections, the active materials were weighed with respect to the polymer weight. The same three-step heat treatment used to prepare the carbon fibers in section 5.2.1 was used to prepare the carbon fiber composites discussed in this work. Table 7, at the end of this section, summarizes the stirring time and temperature as well as the different spinning parameters used for each solution.

To compare the electrochemical performance of the composite fibers prepared from aqueous and mixture (water:ethanol) PVP-based solutions, TiO_2/C and Sn/C composite fibers were also prepared using ethanol as the solvent and a PVP concentration of 12 wt.%. Active

material concentrations of 15, 25, and 35 wt.% were used for TiO_2 while concentrations of 10 and 15 and 25wt.% were used for Sn. The stirring and spinning parameters used to prepare these solutions are illustrated in Table 7.

5.2.2.1. TiO₂/C Composite Fibers

20g of aqueous solutions with 28 wt.% PVP concentration were prepared by first dispersing, 15, 25, and 35 wt.% of TiO_2 particles in the solvent followed by the addition of the polymer to the solution. Next, the aqueous solutions were homogenized by magnetic stirring at 70 °C for 5 h. The solutions were then cooled down to room temperature and put in a vortex to accelerate their homogenization. Finally, they were put back on a hot plate for 5 more hours of magnetic stirring at 70 °C.

Similarly, 20g solutions with 22 wt.% PVP concentration were prepared by first dispersing, 15, 25, and 35 wt.% TiO_2 particles in a 1:1 water:ethanol (wt./wt.) solvent mixture followed by the addition of the PVP. The solutions were then homogenized by magnetic stirring at 50 °C for 5 h.

5.2.2.2. Sn/C Composite Fibers

Sn/PVP precursor solutions were prepared by first dispersing 10, 15, and 25 wt.% Sn particles in a 1:1 water:ethanol (wt./wt.) solvent mixture followed by the addition of 22 wt.% PVP. The 20 g solutions were then homogenized by magnetic stirring at 50 °C for 5 h.

Table 7. Parameters used to homogenize solutions during magnetic stirring and spin composite fibers by centrifugal spinning.

PVP Concentration wt.%	Solvent	Active Material	Stirring Time (h)	Stirring Temperature (C)	Spinning time (min:sec)	Spinning speed (rpm)
28	DI Water	TiO2	10	70	9	10,000
22	Water:Ethanol	TiO2	5	50	6	9,000
12	Ethanol	TiO2	N/A	25	0:40	7,000
22	Water:Ethanol	Sn	5	50	6	9,000
12	Ethanol	Sn	N/A	25	0:40	7,000

5.2.3. Surface tension

PVP aqueous solutions with concentrations of 20, 25, and 28 wt.% were prepared following the same procedures used to prepare the carbon-fiber precursor solutions. In addition, aqueous solutions with 20 wt.% PVP and active material (Sn and TiO_2) concentrations of 10, 20, and 30 wt.% were prepared by magnetic stirring at 70 °C for 5 h. The density of the solutions was determined by weighing 2 mL of each solution in a close container. Solution droplets were formed using the goniometer. 10 drops were formed for each solution and the surface tension of each drop was measured 10 times for a total of 100 measurements per solution. Finally, the average of these 100 measurements was calculated to determine the surface tension of each solution.

5.2.4. Viscosity measurements

Viscosity was measured by inserting the rheometer's viscosity probe in a 10 mL graduated cylinder containing 10 mL of each solution used to characterize the surface tension. After reaching steady state at angular velocities of 40, 80, 120, 160, 200, and 240 rpm, viscosity measurements were taken. Finally, an average viscosity was determined from the viscosity values taken at different angular speeds.

CHAPTER VI

RESULTS AND DISCCUSIONS

6.1. Material Characterization

6.1.1. Fiber Formation and Morphology of PVP Fibers

Fig. 7 shows the fibers during centrifugal spinning as well as their appearance when collected, annealed, and carbonized. Among the three different PVP concentrations, the 25 wt.% solution had the highest fiber yield (Fig. 7a). In previous studies, the centrifugal spinning of PVP precursor solutions in ethanol with concentrations less than 20 wt.% resulted in bead-free PVP nanofibers with a high yield of fibers [27] [28]. When using water as the solvent, PVP fibers were only produced with polymer concentrations of 20 wt.% or higher. At 25 wt.%, the fiber production rate from an aqueous PVP solution was able to match that from PVP/ethanol precursor solutions. The 20 wt.% PVP solution also produced similar amounts, but at this concentration, the production of fibers became more sensitive to higher humidity levels whereas the 25 and 28 wt.% solutions were unaffected by humidity. Although the 28 wt.% PVP solution was not as sensitive to humidity, it yielded beaded fibers.

The better production rate of the more concentrated solutions can be explained by several factors. It has been hypothesized that solvents with higher volatility lead to higher viscosity during the fiber formation in centrifugal spinning [116]. Therefore, the faster vaporization rate of ethanol leads to a higher viscosity at the tip of the needle before producing a fiber jet.

To compensate for the lower vapor pressure of water, higher polymer concentrations are needed to increase the viscosity of the solution at the tip of the needles [116]. Another observation is that successful fiber production was only achieved at higher spinneret rotational speeds compared to solutions prepared with ethanol only. This is also due to the lower evaporation rate of water. Since increasing rotational speed increases the solvent evaporation rate, faster speeds are needed for the complete depletion of water from the fibers [116].
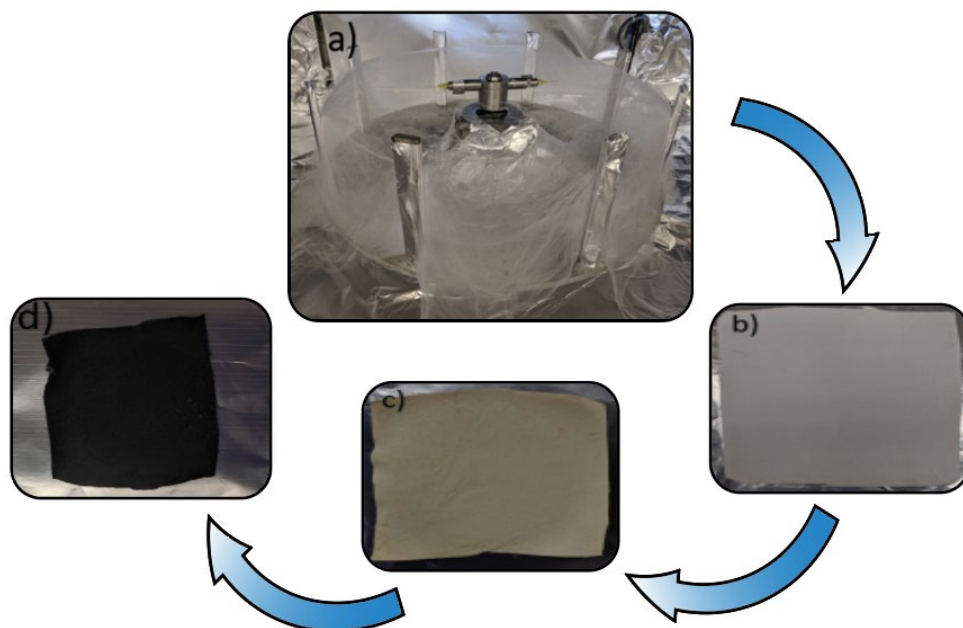

Fig. 7. a) Centrifugal spinning setup, b) pristine collected fiber membrane, c) annealed fiber membrane, and d) carbonized fibers.

The fibrous mats retained a similar overall volume and surface area after annealing, but their appearance, weight, and average fiber diameter changed. The fibers turned from white to a light yellow color and an average of 21.3% weight loss was recorded after annealing. This is attributed to the excess water in the fibers that was removed during annealing. After carbonization, the fibers suffered an average of 63.2% weight loss. Although the fibers shrank due to the carbonization process, they remained flexible. From this point forward, carbon fibers

prepared from aqueous solutions with 20, 25, and 28 wt.% PVP will be referred to as 20C-W, 25C-W, and 28C-W.

Fiber flexibility is crucial because it allows the CFs to be used as binder-free anodes in LIBs. Moreover, these flexible fibers were achieved at a higher carbonization temperature than that in similar studies, which is beneficial electronic conductivity of the fibers [14], [27], [28]. Results on CFs prepared from electrospun PAN precursor fibers and subsequent thermal treatment showed that carbonization temperature plays a central role in increasing conductivity [117]. Achieving such high conductivities enables stand-alone CF anodes to function properly without the addition of conductive fillers or a current collector.

To compare the structure of the CFs obtained from annealed and pristine fibers, both PVP precursor fibers were oxidized and then carbonized using the above-mentioned heat treatment. This comparison corroborated that the annealing process is crucial to produce flexible CFs. Fig. 8 shows the pristine (bottom) and annealed (top) fibers before carbonization and the resultant structure. As shown in Fig. 8, when the carbonization of PVP fibers was performed without the annealing process, brittle carbon fibers were obtained. On the other hand, the annealed fibers reduced fiber shrinkage during carbonization while maintaining a flexible structure.
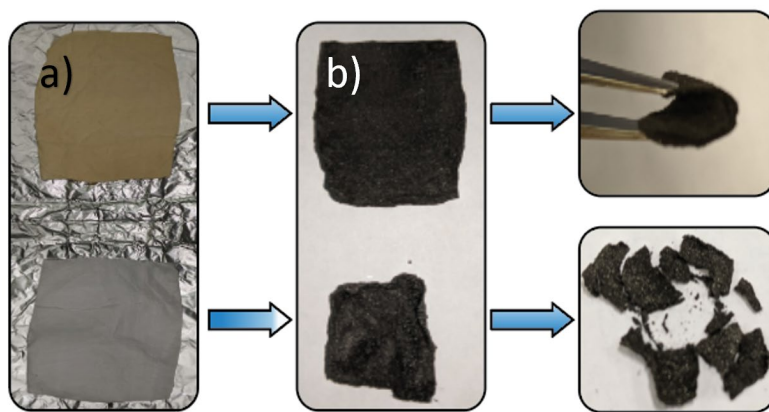

Fig. 8. a) Pristine (bottom) and annealed (top) fibrous membranes, b) Carbonized fibers from pristine (bottom), and annealed (top) fibrous membranes.

Fig. 9 shows the average diameter of the pristine, annealed, and carbonized fibers prepared from PVP precursor solutions with different concentrations of 20, 25, and 28 wt.%. It can be observed in Fig. 9 that even though the 25wt.% solution produced the highest fiber yield, it also produced fibers with the largest diameter. Nevertheless, these fibers still have a smaller diameter than centrifugally spun PVP fiber prepared with ethanol only (1.99 μm) [28].

Fig. 10, Fig. 11, and Fig. 12 show the SEM images, diameter distribution, and histograms of the pristine, annealed, and carbonized fibers prepared from the 20, 25, and 28 wt.% PVP solutions, respectively. A common behavior observed is that the annealing process resulted in increased diameters of the pristine fibers. For the 28 wt.% PVP pristine fibers, one can observe that the fiber diameter not only increased, but a significant change in morphology also took place. The pristine 28 wt.% PVP fibers had a "ramen-like" structure, but their morphology changed to a more homogeneous cylindrical cross-section after annealing. Another observation is that beads are less present in fibers prepared from the 20 and 25 wt.% PVP solutions.
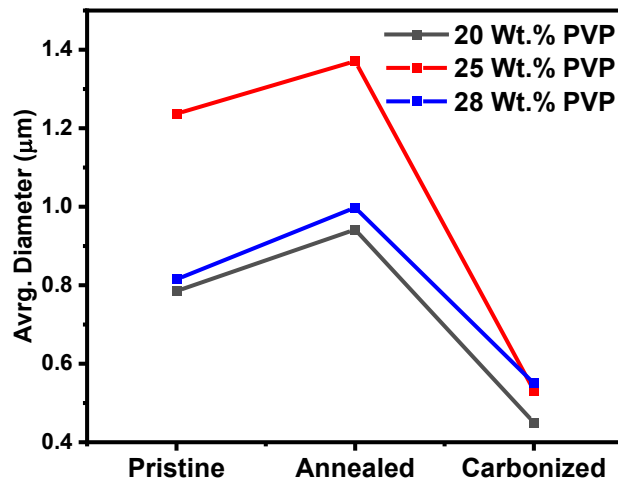

Fig. 9. Average diameters of pristine, annealed, and carbonized fibers prepared from the 20, 25, and 28 wt.% PVP aqueous solutions.
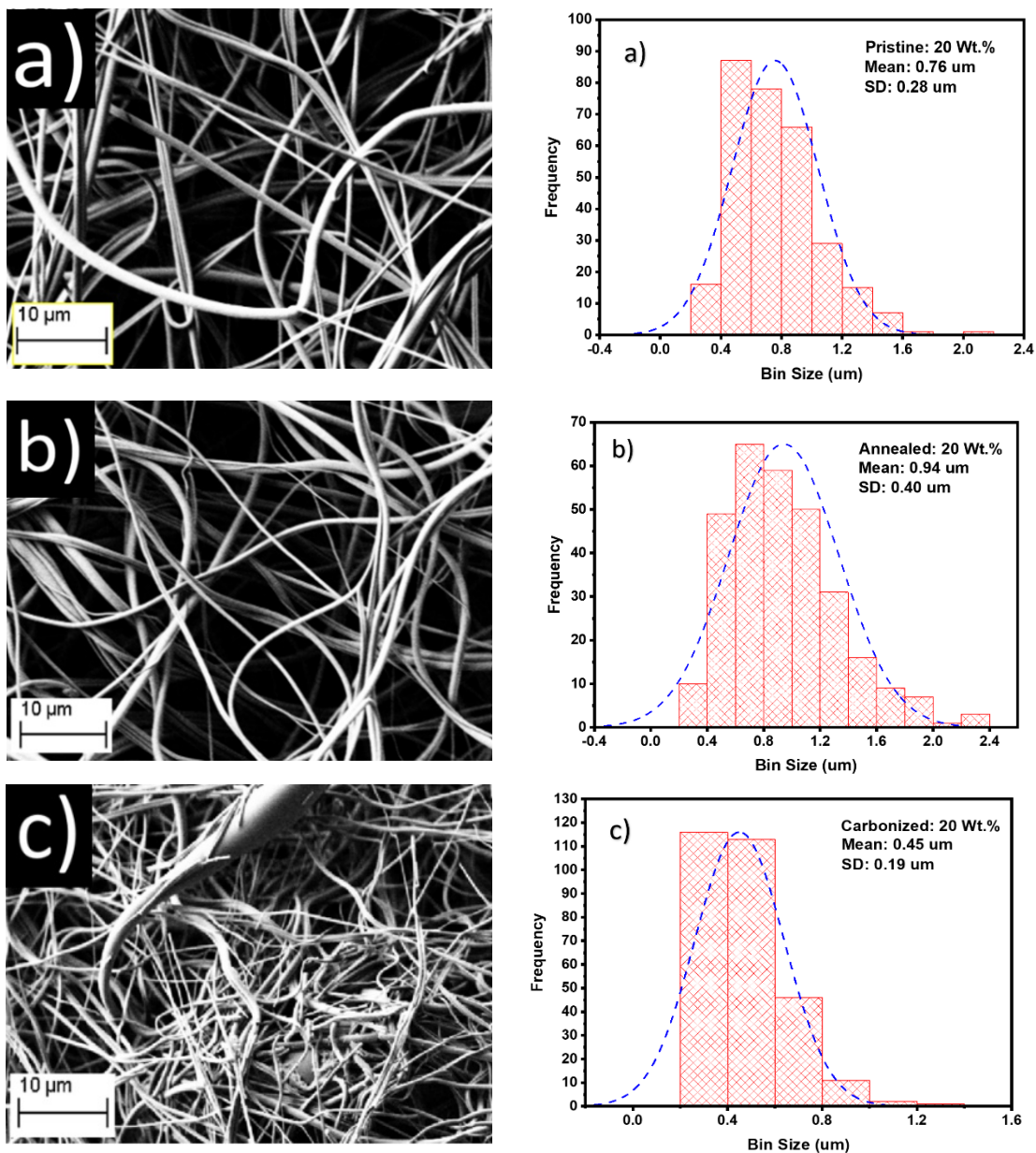
Fig. 10. SEM images of fibers prepared from 20 wt.% PVP precursor solution, fiber diameter distribution, and histogram: a) pristine fibers, b) annealed fibers, and c) carbon fibers.

Fig. 11. SEM images of fibers prepared from 25 wt.% PVP precursor solution, fiber diameter distribution, and histogram: a) pristine fibers, b) annealed fibers, and c) carbon fibers.
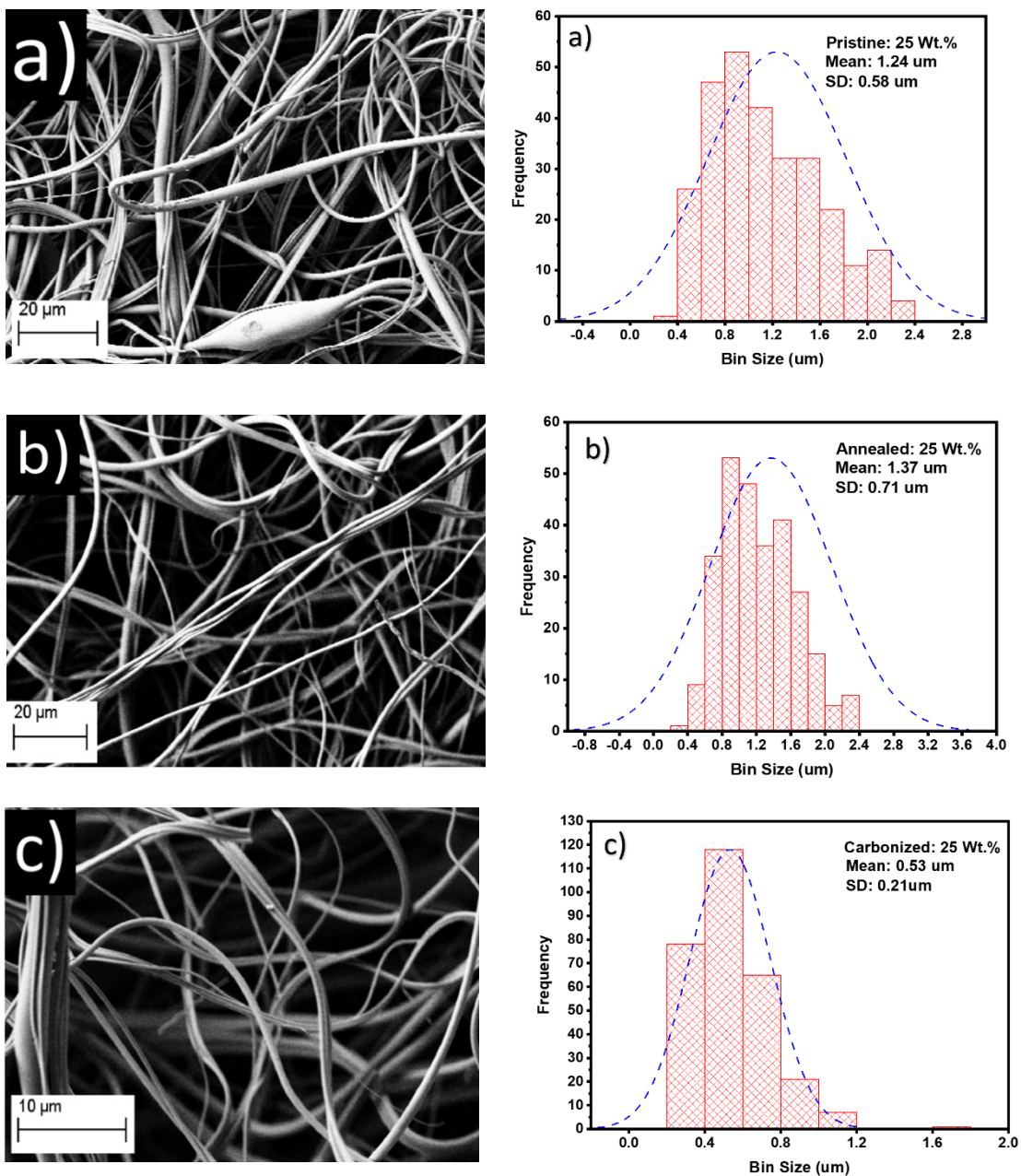
Fig. 12. SEM images of fibers prepared from 28 wt.% PVP precursor solution, fiber diameter distribution, and histogram: a) pristine fibers, b) annealed fibers, and c) carbon fibers.
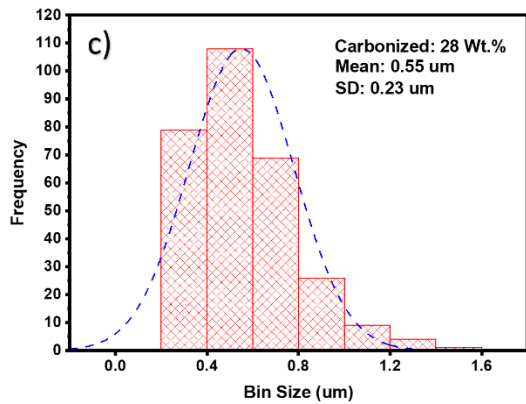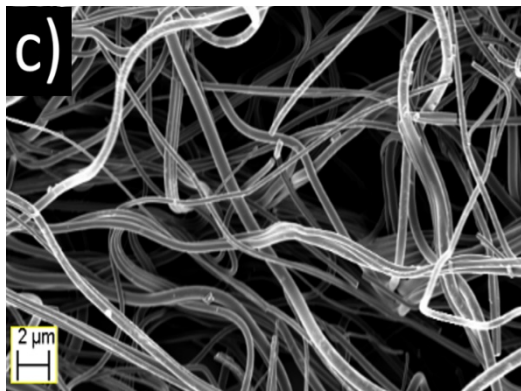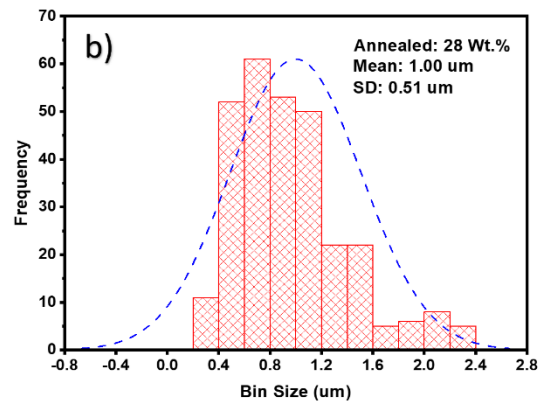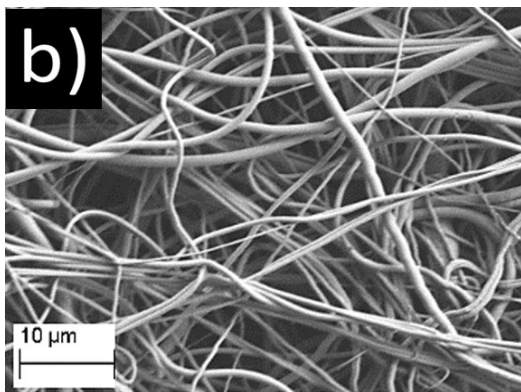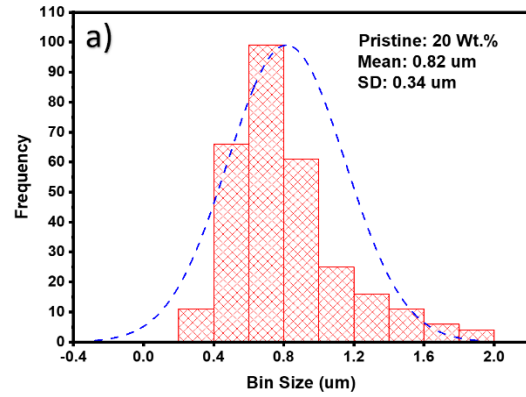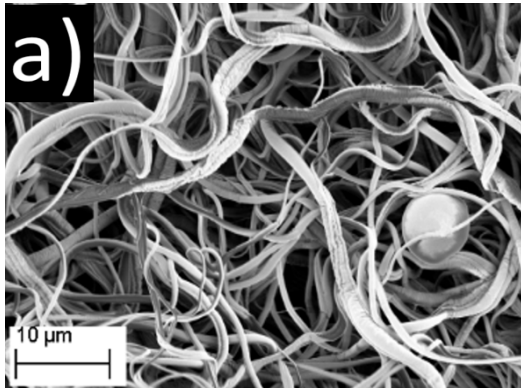
6.1.2. Fiber Formation and Morphology of Composite Fibers

PVP aqueous solutions with different concentrations of 10, 15, 20, 25, and 28 wt.% were

prepared with active material loading of 10, 15, and 25 wt.% for Sn, and 15, 25, and 35 wt.% for

TiO_2. A wide range of angular velocities (1000 – 10,000 rpm) and spinning times ($\leq$ 9 min)

were explored to determine the spinning parameters needed for the formation of composite

fibers. Nonetheless, the fiber production rate needed to collect an entire fibrous mat was not

achieved in the case of solutions with Sn. PVP/TiO_2 fiber membranes were successfully spun at

higher rates in PVP aqueous solutions with a 28 wt.% PVP. However, the fiber diameter of these

fibers was large, and beads were found (Fig. 13). In addition, the fiber formation was

inconsistent and no distinct solution attribute for successful fiber formation could be recognized.

Fibers with 15, 25, and 35 wt.% of TiO_2 were subsequently carbonized to prepare the TiO_2/C

composite-fiber anodes. These composite carbon fibers will be referred to as 28C/15TiO_2-W,

28C/25TiO_2-W, and 28C/35TiO_2-W from this point forward. The diameter distribution

(histograms) for these carbon fiber composites are shown in Figures A1 through A3 in the
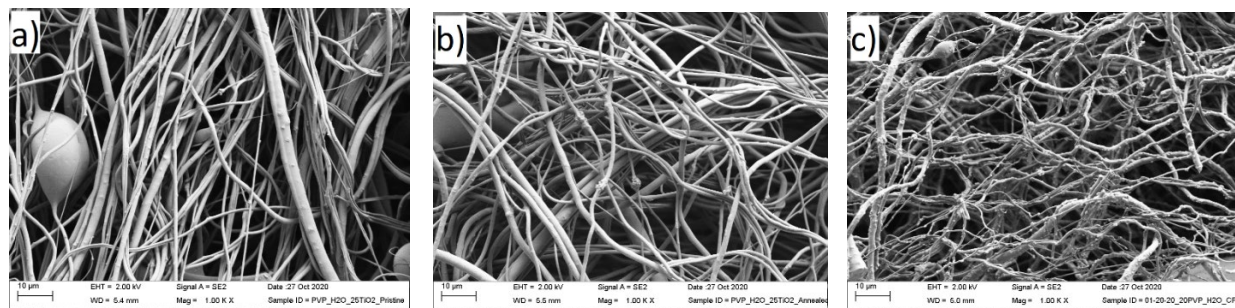
appendix.

Fig. 13. Fiber Morphology of a) pristine, b) annealed, and c) carbonized fibers prepared from 28 wt.% PVP precursor solution with 25 wt.% TiO2.

In order to consistently produce composite fibers at higher rates, the vapor pressure of the

precursor solution must be increased by adding a volatile solvent. In this work, ethanol was

chosen as the volatile solvent due to its higher vapor pressure compared to that of water [118].

Raoult's law was used for water/ethanol solvent mixtures at different ratios to approximate the

increase in vapor pressure [119]. As an illustration, the following calculations show the

procedure followed to estimate the vapor pressure of a 10g water/ethanol mixture at 25 °C with

10 wt.% water.

$$1g\ H_2O * \frac{1\ mol\ H_2O}{18.01\ g} = 0.0555\ moles\ of\ H_2O\ in\ 1g\ of\ water = n_{water}$$

$$9g\ C_2H_6O * \frac{1\ mol\ C_2H_6O}{46.08\ g} = 0.1953\ moles\ of\ C_2H_6O\ in\ 9g\ of\ ethanol = n_{ethanol}$$

$$X_{water} = \frac{n_{water}}{n_{water} + n_{ethanol}} = 0.2213$$

$$X_{ethanol} = \frac{n_{ethanol}}{n_{water} + n_{ethanol}} = 0.7787$$

Ethnol partial pressure: $P_{ethanol} = X_{ethanol} * P^o_{ethanol} = 45.7876$ mm Hg

where $P^o_{ethanol}$ is the pressure of pure ethanol: 58.8 mm Hg

Water partial pressure: $P_{water} = X_{water} * P^o_{water} = 5.2670$ mm Hg

where P^o_{water} is the pressure of pure water: 23.8 mm Hg

Solvent mixture vapor pressure: $P_{solvent} = P_{ethanol} + P_{water} = 51.046$ mm Hg

Similar calculations were performed for multiple water compositions to produce the results

shown in Table 8 and Fig. 14. The results in Figure 14 show the vapor pressure (mm Hg) in a

water/ethanol solvent mixture as a function of water wt.% where the vapor pressure of

water/ethanol mixture decreases with increasing water concentration.

Table 8. Vapor pressure of water/ethanol solvent mixtures at different ratio compositions

| Water/Ethanol solution		10 g Solution W/E		Number of Moles		Mole fractions		Partial pressure (mm Hg)		Solution Vapor Pressure (mm Hg)
Water Wt%	Ethanol Wt%	Water Wt. (g)	Ethanol Wt. (g)	Water	Ethanol	Xw	Xe	Pw	Pe	Water/Ethanol
0	100	0	10	0.00	0.22	0.00	1.00	0.00	58.80	58.80
10	90	1	9	0.06	0.20	0.22	0.78	5.27	45.79	51.05
20	80	2	8	0.11	0.17	0.39	0.61	9.28	35.86	45.15
30	70	3	7	0.17	0.15	0.52	0.48	12.45	28.05	40.50
40	60	4	6	0.22	0.13	0.63	0.37	15.00	21.74	36.74
50	50	5	5	0.28	0.11	0.72	0.28	17.11	16.53	33.64
60	40	6	4	0.33	0.09	0.79	0.21	18.88	12.16	31.04
70	30	7	3	0.39	0.07	0.86	0.14	20.38	8.44	28.82
80	20	8	2	0.44	0.04	0.91	0.09	21.68	5.24	26.92
90	10	9	1	0.50	0.02	0.96	0.04	22.81	2.45	25.26
100	0	10	0	0.56	0.00	1.00	0.00	23.80	0.00	23.80
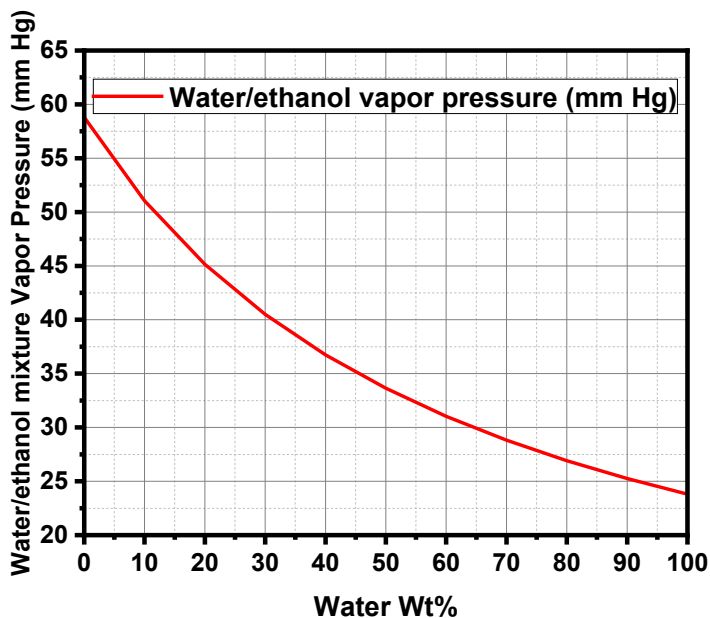
Fig. 14. Vapor pressure vs. water composition for a 10 mg ethanol-water solvent mixture

It is important to mention that although Raoult's law can be used to approximate the

vapor pressure of the solvent mixture, it cannot be used to approximate the vapor pressure of

48

polymer solutions due to the polymer three-dimensional network swelling and the elastic component that gelation introduces to the solution [120] [121].

For aqueous PVP solutions, the material concertation threshold to produce nano/micro fibers was 20 wt.%. Therefore, the required minimum solvent vapor pressure to produce fibers at 15 wt.% was sought after. It was observed that fibers can be produced at 15 wt.% PVP with a maximum water percentage of 70% in ethanol, or minimum vapor pressure of 28.82 mm Hg (Table 8). Similarly, PVP solutions (15 wt.%) with 10 wt.% Sn were prepared with different water concentrations for the precursor solution. It was observed that a minimum of 50 wt.% of water in ethanol produced composite fibers. However, the fiber yield was poor. Moreover, beads and solution droplets were still observed in the fibers and casing of the centrifugal spinning machine, respectively.

Studies on the surface tension of aqueous PVP solutions show that the surface tension decreases with increasing polymer concertation while viscosity exponentially increases [122]. These behaviors are beneficial since the time for bead formation is proportional to viscosity and inversely proportional to surface tension [116]. Hence, increasing the polymer concentration in the solution would increase the time for bead formation due to Rayleigh instabilities and allow a longer evaporation time for fiber formation with a homogeneous cylindrical cross-section. Based on this hypothesis, the water percentage in ethanol was kept at 50% while the polymer concentration was increased to 20 and 25 wt.% PVP while maintaining a 10 wt.% Sn as active material. After some iterations, an optimum polymer concertation of 22 wt.% PVP in 50% water (or 1:1 water: ethanol (wt./wt.)) was determined for the successful production of composite fibers. Solutions with Sn concentrations of 10, 15, and 25 wt.% were prepared. However, only the solutions with 10 and 15 wt.% Sn produced fibers. The carbon fibers formed from these

Sn/PVP precursor fibers will be referred as 22C/10Sn-W:E, and 22C/15Sn-W:E. Similarly, TiO$_2$/C composite fibers prepared from TiO$_2$/PVP precursor solutions using the water:ethanol solvent mixture will be referred as 22C/15TiO$_2$-W:E, 22C/25TiO$_2$-W:E, and 22C/35TiO$_2$-W:E from this point forward. For simplicity, Fig. 15 shows a schematic for carbon and composite carbon fibers nomenclature interpretation.
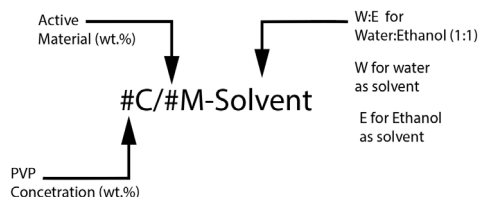

Fig. 15. Interpretation for carbon and composite carbon fibers anodes nomenclature structure.

Despite the successful high fiber yield of composite fibers with the 1:1 water:ethanol solvent, the morphology of the produced fibers was unfavorable. Particles in both cases, pristine and annealed fibers, were seldomly found (Fig. 16a and Fig. 16b; Fig. 17a and Fig. 17b). This lack of particle exposure was attributed to the large fiber diameter obtained due to the addition of ethanol to the solution [41]. In general, particles were only spotted when large agglomerations outgrew the diameter of the fibers. Even though the average fiber diameter decreased after the carbonization process and more particles were exposed on the surface of the carbon fibers, the average diameter of the composite carbon fibers remained larger than desired (Fig. 16c and Fig. 17c). For comparison, the fiber diameters for 28C/TiO$_2$-W and 22C/TiO$_2$-W:E carbon fibers with all three, 15, 25, and 35, active materials loadings are presented in Fig. 18. The histograms with linear distribution curves for the 22C/15TiO$_2$-W:E, 22C/25TiO$_2$-W:E, and 22C/35TiO$_2$-W:E carbon fibers are shown in Figures A4 through A6 in the appendix.
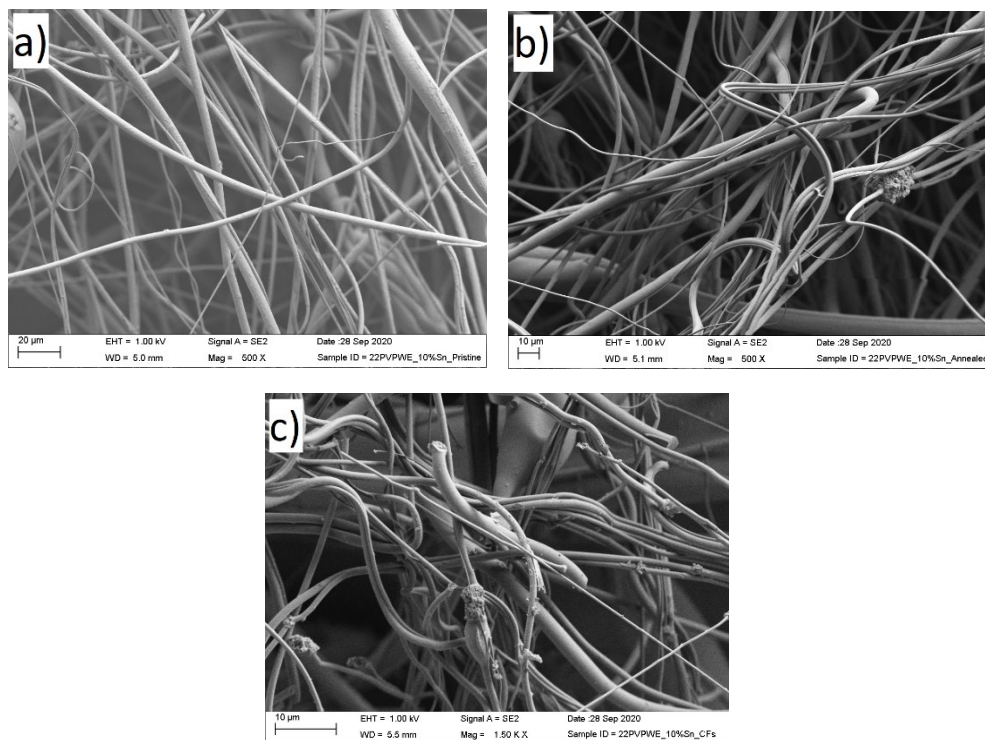
Fig. 16. Fiber Morphology of a) pristine, b) annealed, and c) carbonized 22 wt.% PVP/10 wt.% Sn in 1:1 water:ethanol solvent.
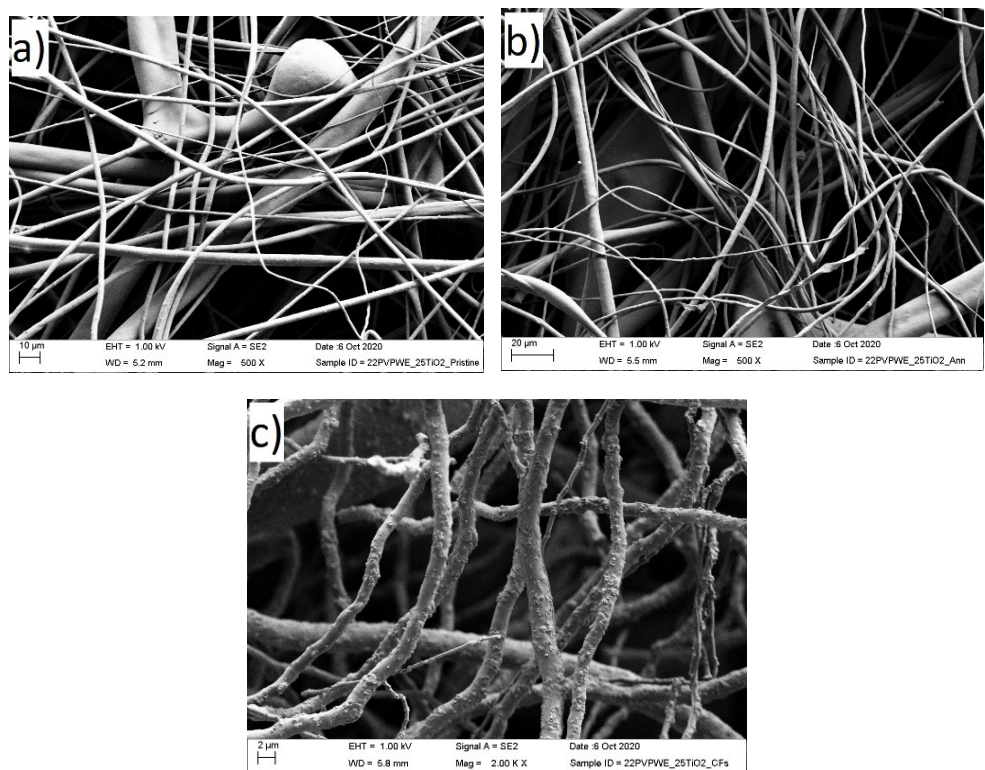

Fig. 17. Fiber Morphology of a) pristine, b) annealed, and c) carbonized 22 wt.% PVP/25 wt.% TiO2 in 1:1 water:ethanol solvent.
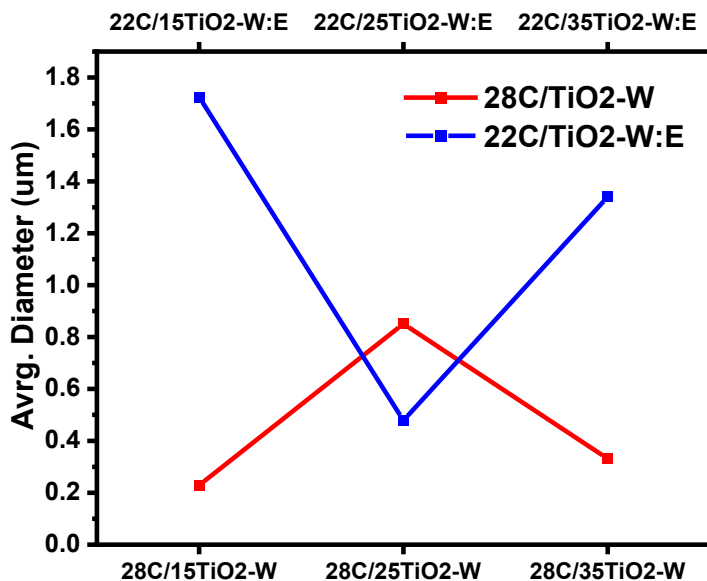
Fig. 18. Average diameter of C/TiO$_2$-W and C/TiO2-W:E carbon fibers.

6.1.3. Viscosity and Surface tension

To corroborate an increase in viscosity and decrease of surface tension with increasing polymer concentration, viscosity and surface tension tests were performed on solutions with different PVP concentrations of 20, 25, and 28 wt.%. The results in Table 8 show that the increase in polymer concentration indeed increased solution viscosity and reduced the surface tension. The effect of nanoparticles on viscosity and surface tension was also investigated by comparing a 20 wt.% PVP aqueous solution to polymer solutions with the same concentration (20 wt.% PVP) and 10, 20, and 30 wt.% Sn or TiO$_2$ loads. The obtained results are also presented in Table 9. In general, the surface tension and solution viscosity decreased with increasing nanoparticle concentration in the solution.

Table 9. Surface tension (mN/m) and Viscosity (cP) measurements for PVP/water and PVP/water/active material solutions.

Material	Surface Tension (mN/m)	Viscosity (cP)	Density (g/cc)	kinematic viscosity (cSt or mm^2/s)	Average Surface Tension	Average Viscosity (cP)
20% PVP - H2O	56.45	4626	0.872	5305.05	N/A	N/A
25% PVP - H2O	55.23	16133	0.883	18270.67		
28% PVP - H2O	49.07	53450	0.847	63105.08		
20% PVP/10% Sn - H2O	54	3635	0.84	4327.38	54.80	6,430.00
20% PVP/20% Sn - H2O	57.02	8455	0.881	9597.05		
20% PVP/30% Sn - H2O	53.37	7200	0.856	8411.21		
20% PVP/10% TiO2 - H2O	52.03	4992	0.85	5872.94	51.84	4,744.67
20% PVP/20% TiO2 - H2O	51.16	4309	0.846	5093.38		
20% PVP/30% TiO2 - H2O	52.32	4933	0.861	5729.38		

As observed in Table 9, an increase in polymer concentration plays a much greater role in viscosity and surface tension than the addition of nanoparticles to the aqueous solution. Thus, other factors that could prevent the production of composite fibers in aqueous solutions were explored. During the viscosity measurement, it was observed that the viscosity at the lower portion of polymer solutions with Sn was slightly lower than the viscosity at the upper portion of the solution. This observation led to the investigation of particle dispersion in water and ethanol solutions. To perform this comparison, 5 wt.% Sn and 5 wt.% TiO$_2$ were dispersed in 10g water and ethanol followed by 30 minutes of ultrasonication and 1 minute of mixing in a vortex. Then, the solutions were left overnight to compare particle sediments the next day in both solutions (Fig. 19). It was evident that particles remained more dispersed in ethanol than in water. Well-

defined particle rich and particle poor layers were observed in the Sn/water solution. This comparison could explain the unsuccessful formation of Sn/C composite fibers from aqueous precursor solutions due to needle clogging. Moreover, this behavior could also explain the irregularity of successful TiO$_2$/PVP composite fibers formation using aqueous solutions because different periods took place between the homogenization of the aqueous TiO$_2$ solutions and their subsequent spinning attempt.

The implementation of nanostructures such as nanoparticles, nanofibers, nanowires, nanorods, or nanosheets in fluids is a new class of lubricants in tribology. This class of fluid lubricants is known as nanofluids [123]. In that field, ceramic and metal nanoparticles are dispersed in base fluids such as water and oil and it has been observed that particle dispersion is a major challenge affecting the effective performance of these nanofluids, especially for metal nanoparticles. In general, some of the techniques that ameliorate particle dispersion in water include intensive use of ultrasonic equipment, variation in pH values, and the addition of surface agents (dispersants and surfactants) [123].
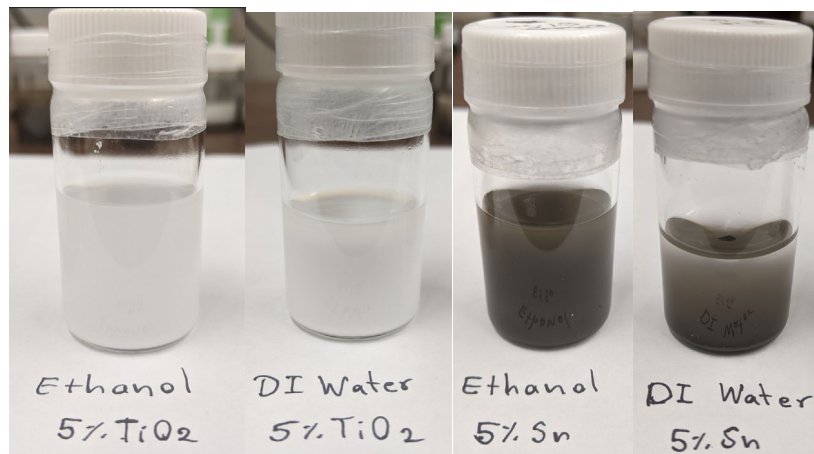

Fig. 19. Comparisons between TiO2 and Sn particle dispersion in ethanol and water ~12hrs after dispersion.

6.1.4. Raman Spectroscopy of Carbon Fibers

The Raman lines of PVP powder and corresponding centrifugally spun nanofibers are shown in Fig. 20. There are no significant differences among these spectra. This was expected as the size of the nanofibers is not sufficiently small to incur confinement effects. In the low Raman shift regions, relatively few broad lines were recorded in the pristine and annealed PVP fibers at 133, 365, and 556 cm^{-1}. They are tentatively assigned to longitudinal acoustic modes or ring vibrations. C-C ring vibrations and breathing modes were reported at 760 and 937 cm^{-1}, respectively [124], [125].

Fig. 21a and Fig. 21b show the effect of the annealing at 150 °C on the PVP nanofibers obtained from the 20 % PVP solution. A detailed analysis showed that the main consequences of the annealing process were manifested by a decrease in the amplitude of the Raman lines and their broadening. It was noticed that within experimental errors, the line positions were not significantly affected by annealing and that all intense lines were still present in the spectrum of the annealed nanofiber. Similar behavior was observed for the annealed nanofibers obtained from 25 % and 28 % PVP solutions.
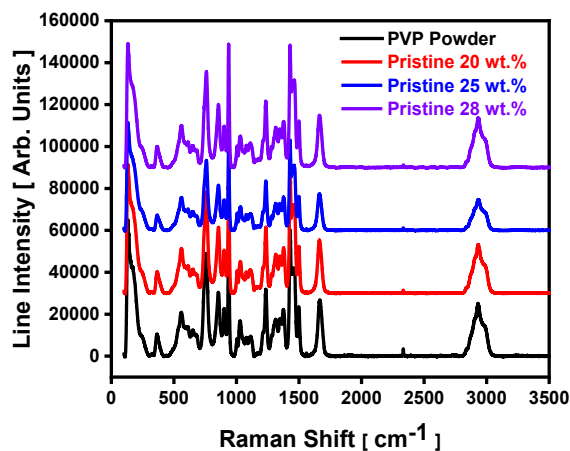

Fig. 20. Raman lines of PVP powder and PVP pristine fibers prepared from solutions with PVP concentrations of 20, 25, and 28 wt.%.
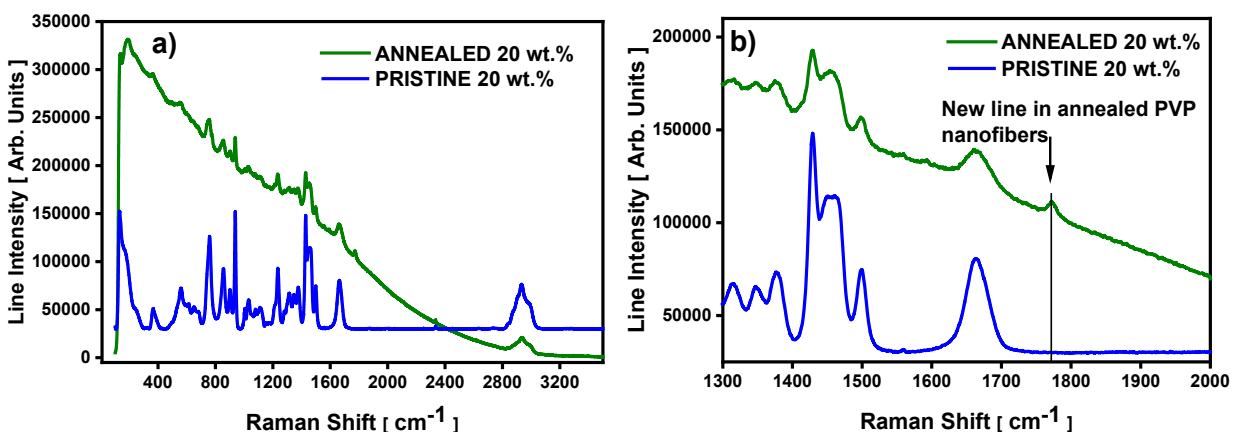
Fig. 21. A comparison between the Raman spectra of pristine and annealed fibers prepared from the 20 wt.% PVP solution in water.

Fig. 22 shows the Raman spectra of the PVP powder and the corresponding pristine, annealed, and carbonized nanofibers obtained from a solution containing 20 wt.% PVP in water. The annealing process of the PVP nanofibers decreased drastically the intensity of the Raman lines while very the carbonization process of the PVP nanofibers at 700 °C produced substantial changes in the Raman spectra of the nanofibers. Most of the lines assigned to PVP powder or nanofibers are completely erased by the carbonization process. Apparently, only the line located at 1235 cm^{-1} survived, although it is slightly shifted and broadened. The most intense line located at 1363 cm^{-1} was identified as the D band in carbonaceous materials [126]. The G line is located at about 1568 cm^{-1} [126], being weak and broad and appears as a shoulder of the D band. Furthermore, the line observed at 1874 cm^{-1} was tentatively assigned to C=O bonds, reflecting the oxidation of the polymer chains, while the line at 2368 cm^{-1} was identified as G' (i.e., as an overtone 2 phonon process) of the D band [126]. Finally, the line at 3269 cm^{-1} may be assigned as an overtone of the G band [126], [127]. Thus, the carbonization process of the PVP nanofibers resulted in the appearance of the D and G bands, a feature that was reported in a previous study [128].
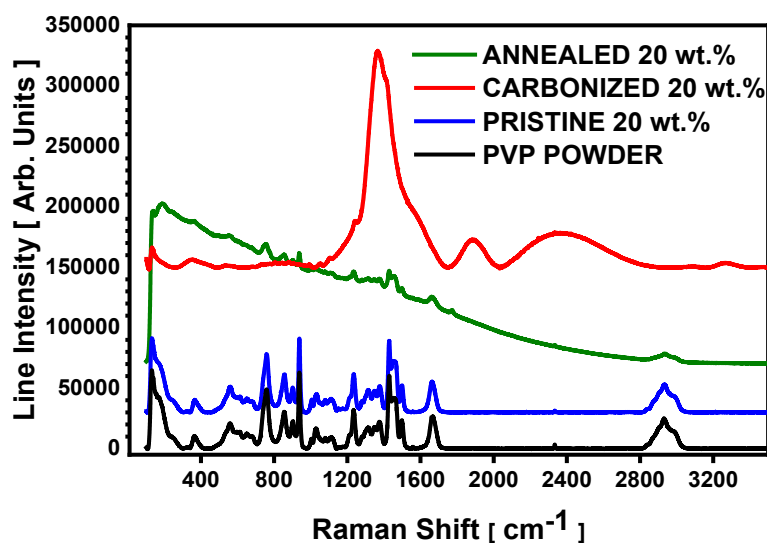
56

Fig. 22. Raman spectra of PVP powder, and PVP pristine, annealed, and carbonized fibers prepared from the 20 wt.% solution.

6.1.5. Thermogravimetric Analysis of Carbon Fibers

TGA was conducted on pristine and annealed PVP fibers in air and nitrogen atmospheres to assess the resilience of annealed fibers to degradation. In this analysis, a heating rate of 5 °C/min was used for all the samples in a range between 25 and 700 °C. In both air and nitrogen atmospheres, the annealed fibers yielded more residue than the pristine fibers. The residual masses for both samples are illustrated in Fig. 23. Under an airflow, the annealed fibers yielded a residual mass of 3% while the pristine fibers only yielded a 0.6%. Thus, the annealed PVP fibers produced about five times more residue than the pristine PVP fibers. When both annealed and pristine fibers were heated in an inert flow (nitrogen), the annealed fibers yielded a residual mass of 11.3 % while the pristine fibers yielded 5.4%. In this case, the annealed fibers produced twice the amount of residue produced by the pristine fibers, indicating that the carbon yield in the annealed fibers is higher. This comparison shows that, indeed, annealed fibers have a higher resistance to degradation. Even though both annealed and pristine fibers reached a degradation plateau at the same temperature (~450 °C under nitrogen and ~650 °C in air), the lower

57

degradation rate in the annealed fibers enabled them to retain more carbon when the degradation

temperature thresholds were reached. Nevertheless, it is crucial to mention that these residual

mass percentages are based on the initial mass (100%) of the fibers at room temperature. In

Figure 10, an initial mass drop was observed in both air and nitrogen atmospheres at

temperatures below the onset of degradation. This initial mass loss is attributed to the

evaporation of water absorbed by the PVP fibers, which is hydrophilic. This is supported by

Raman spectra, which did not reveal the disappearance (or appearance) of new Raman lines upon

annealing. Thus, using the first plateau as the reference of 100% weight, higher percentages of

residual mass for both the pristine and annealed PVP fibers can be determined. Using the TGA

data analyzer software (TG 209 F3 Tarsus, NETZSCH, Germany), the mass changes between the

first and second plateaus were determined as -63.9% and -73.6% for the annealed and pristine

fibers, respectively. Thus, residual masses of 36.1% and 26.5% can be obtained (Fig. 24) for the

annealed and pristine fibers, respectively. Furthermore, these values are congruous with the

average mass losses weighed right after the annealing process (63.2 wt.%). Based on the EDS

analysis performed on the residues obtained from annealed and pristine fibers under nitrogen, the

annealed fibers yielded 85% carbon out of its TGA residue, while the pristine fibers yielded 89%

carbon. Thus, using these adjusted values, the annealed PVP fibers yielded 30.6% carbon while

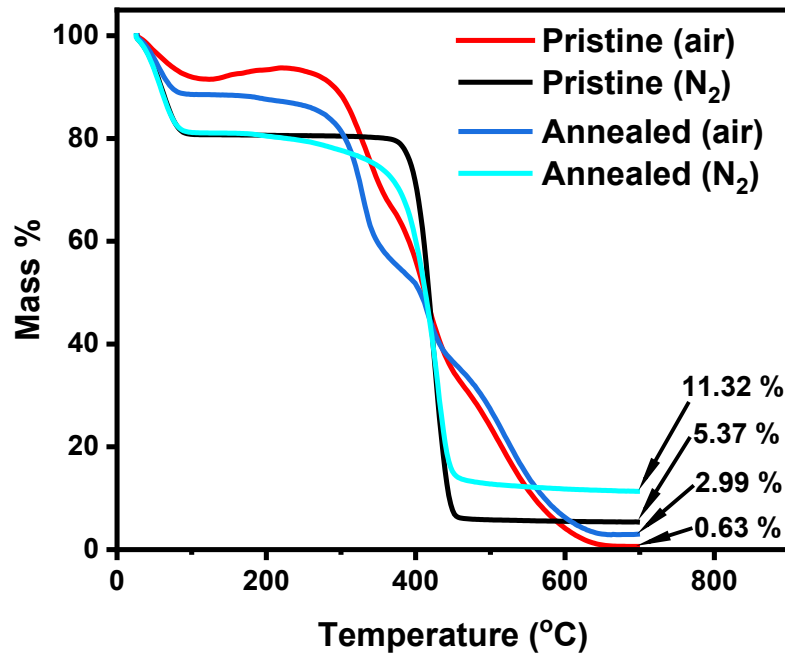the pristine PVP fibers yielded 23.1% carbon.

Fig. 23. TGA analysis of the pristine and annealed PVP fibers in air and nitrogen atmospheres.
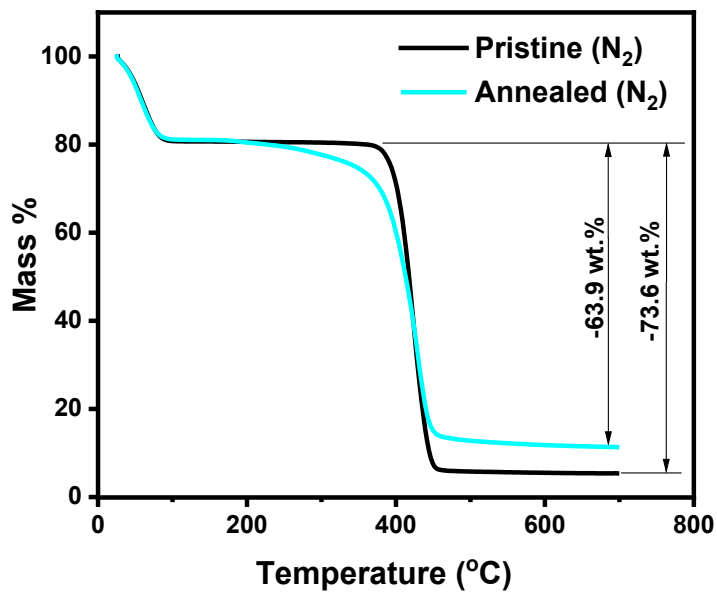

Fig. 24. Mass loss Percentage after removal of water from the pristine and annealed fibers in a nitrogen atmosphere.

The higher mass loss observed in the pristine fibers can be attributed to the lack of fiber stabilization [22]. As a result, the pristine fibers were unable to maintain a long continuous fiber structure due to the high carbonization temperature. Based on heat treatment studies, higher carbonization temperatures turned fibers into rods [32]. This is confirmed by the structure of the pristine derived CFs shown in Fig. 25.
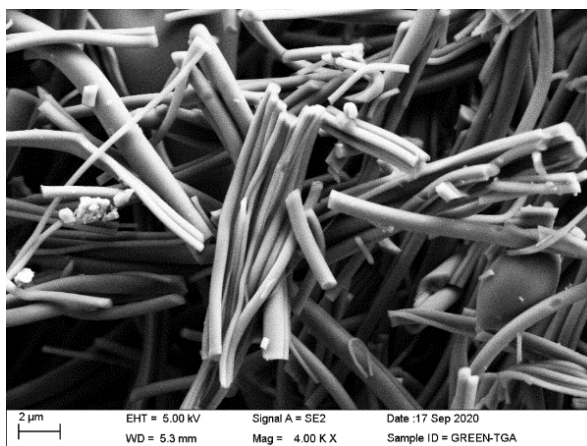

Fig. 25. Carbon fiber structure obtained from pristine PVP nanofibers

6.2. Electrochemical Results

Cycle voltammetry (CV), cycle performance, impedance spectroscopy, and rate performance experiments were conducted on Li-ion and Na-ion half cells using the flexible carbon fibers directly as anodes. TiO$_2$/Cnd Sn/C fiber composite-fiber anodes were also used directly as binder-free anodes in Li-ion half cells.

6.2.1. Cycle Voltammetry

6.2.1.1. Carbon-Fiber Anodes in LIBs

Cyclic voltammetry (CV) tests were performed on the 20C-W, 25C-W, and 28C-W anodes. For all three carbon-fiber anodes, a broad anode oxidation peak was observed at ~0.1V during the anodic scan. Reduction peaks during the cathodic scans appeared in all three anodes at~0.1, ~0.5V, and ~1.5V due to the formation of the solid electrolyte interphase (SEI) and the

60

decomposition of the electrolyte [129]. Fig. 26 shows the CV for the 25C-W carbon fibers. Similar results were obtained for the 20C-W and 28C-W carbon fiber anodes; their CVs can be found in Figures A7a and A7b of the appendix.
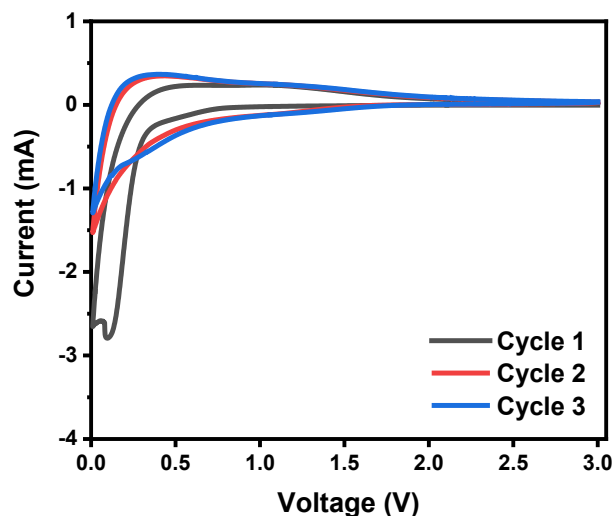

Fig. 26. Cycle voltammetry of 25C-W carbon fibers in half-cell LIBs.

6.2.1.2. Carbon-Fiber Anodes in SIBs

The 20C-W, 25C-W, and 28C-W carbon fibers were also used as anodes in Na-ion half cells. Similar to the CV results of LIBs, the anodes in SIBs exhibited wide oxidation peaks during the anodic scans (~0.1V) and well-defined reduction peaks at ~0.1 and ~0.7V (Fig. 27) due the formation of SEI. In the ordinate axis, a much smaller current range output was observed for these batteries. This was expected since the specific capacity delivered by graphite in SIBs is lower [130] [131]. Although the current output of carbon fibers is lower in SIBs than LIBs, the anodes show consistent CV profiles in both cases. Thus, flat capacity profiles are expected for both SIBs and LIBs. Similar results were obtained for the 20C-W and 28C-W carbon fiber anodes in SIBs; their CVs can be found in Figures A8a and A8b in the appendix.
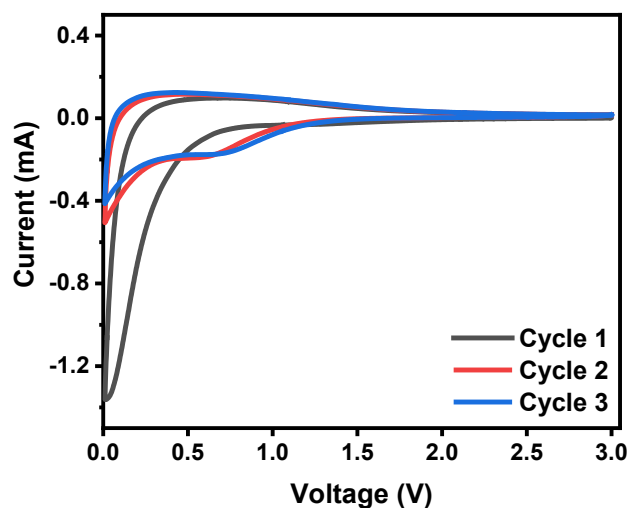
Fig. 27. Cycle voltammetry of 25C-W carbon fibers in half-cell SIBs.

6.2.1.3. Composite TiO₂/C Anodes in LIBs.

It is seen in Fig. 28a, Fig. 28b, and Fig. 28c that oxidation (delithiation) nor reduction peaks (lithiation) characteristic of TiO_2 were not observed in the 28C/15TiO₂-W, 28C/25TiO₂-W, and 28C/35TiO₂-W composite-fiber anodes in Li-ion half-cells. 22C/15TiO₂-W:E, and 22C/35TiO₂-W:E, on the other hand, revealed oxidation (~2.2 V) and reduction peaks (~1.65 V) characteristic of TiO_2 (Fig. 29a and Fig. 29c) [27], [132]. Nonetheless, the overall current range (ordinate axis) corresponding to carbon interaction with the Li-ion is much smaller. This is attributed to the larger fiber diameter in 22C/TiO₂-W:E that reduces the overall carbon surface area available for lithiation/de-lithiation.
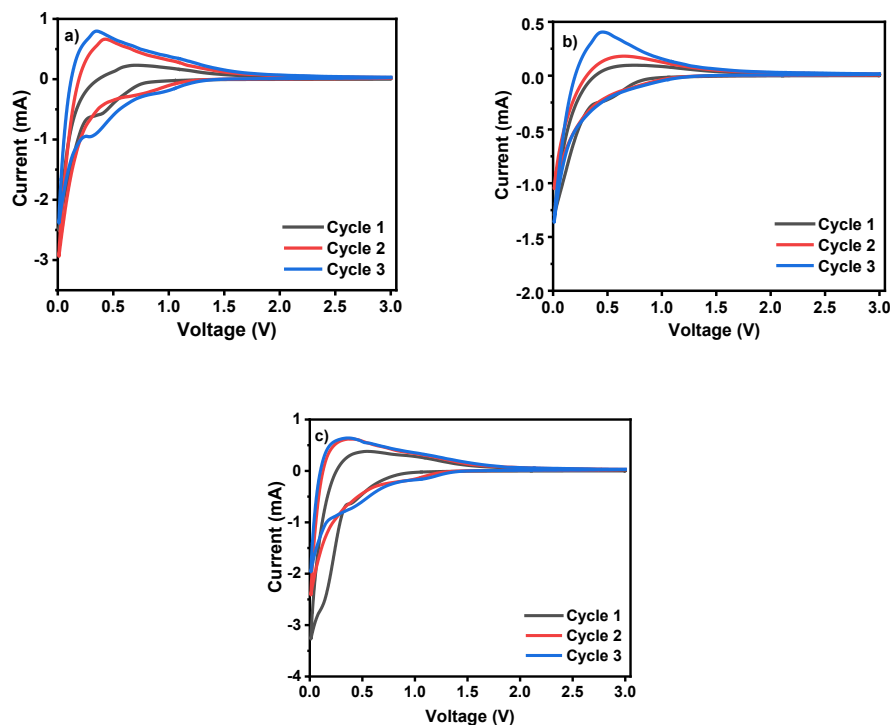
Fig. 28. Cycle voltammetry for the a) 28C/15TiO2-W, b) 28C/25TiO2-W, and c) 28C/35TiO2-W composite- carbon fibers in half-cell LIBs.
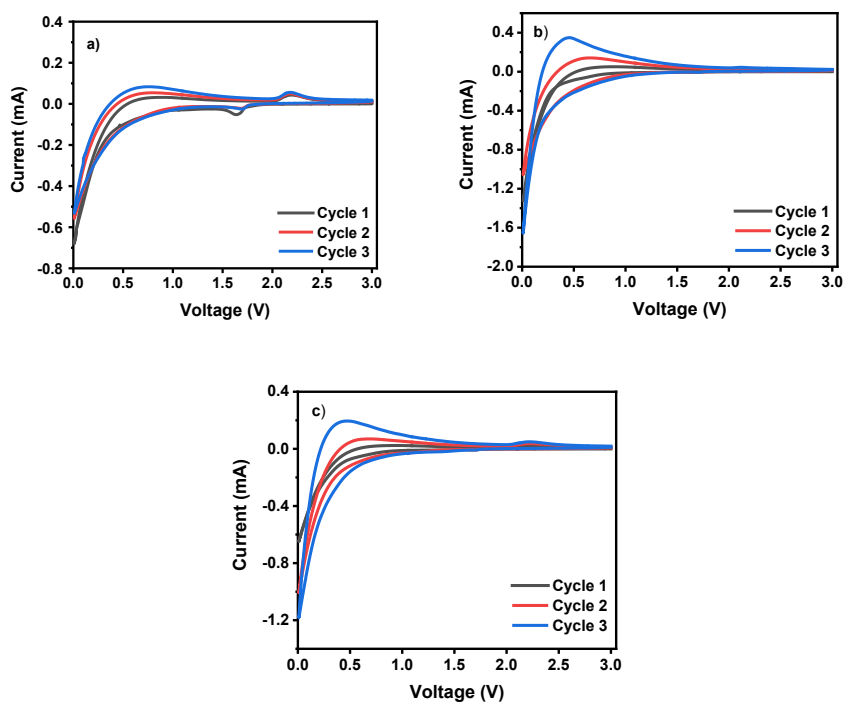

Fig. 29. Cycle voltammetry of a) 22C/15TiO2-W:E, b) 22C/25TiO2-W:E, and c) 22C/35TiO2-W:E composite- carbon fibers in half-cell LIBs.

6.2.1.4. Composite Sn/C Anodes in LIBs

Fig. 30 shows the CV results of the 22C/10Sn-W:E, and 22C/15Sn-W:E composite-fiber anodes. It is observed in Fig. 30 a and Fig. 30b that the CV profile of 22C/Sn-W:E is similar to that of 22C/TiO$_2$-W:E composite-fiber anodes because the characteristic oxidation peaks (~0.4, ~0.6, and ~0.8 V) of Sn are observed in the CV [133], but the overall range of the current output is reduced due to the larger fiber diameter. Nonetheless, distinct Sn reduction peaks (0.34, 0.5, and 0.62 V) were not revealed in the CV results [133]. Finally, the 22C/15Sn-W:E shows a wider current range characteristic of carbon as well as oxidation peaks for the Sn active material. Thus, a higher capacity is expected from these fibers.
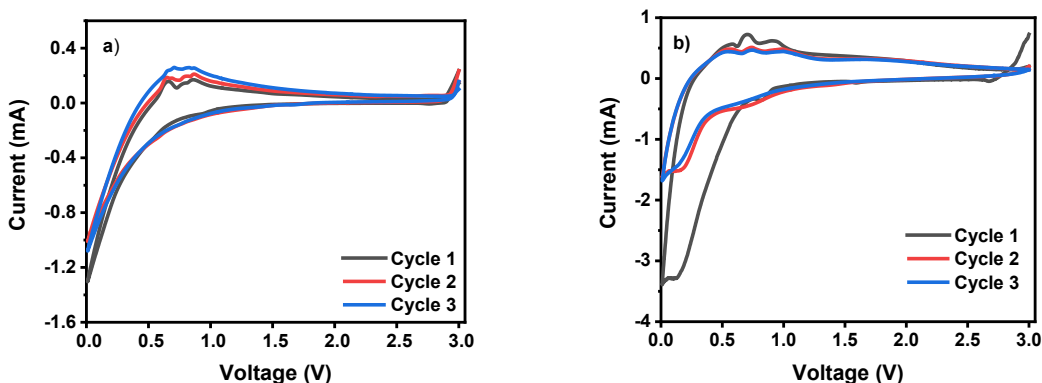

Fig. 30. Cycle voltammetry of a) 22C/10Sn-W:E, and b) 22C/15Sn-W:E composite carbon fibers in half-cell LIBs.

6.2.2. Cycle Performance

6.2.2.1. Carbon fiber Anodes in LIBs

The charge-discharge profiles and cycle performance of the 25C-W carbon-fiber anodes are shown in Fig. 31. The charge-discharge plots and cycle performance for the 20C-W and 28C-W carbon-fiber anodes are shown in the appendix (Figures A9a and A9b, respectively). The galvanostatic charge-discharge experiments were performed at a current density of 100 mA g^{-1}.

At the 1st cycle, the 20C-W, 25C-W, and 28C-W anodes delivered a charge capacity of 205, 189, and 275 mAh g^{-1}, respectively. After the first cycle, the CF anodes maintained a consistent capacity and after 100 cycles, the 20C-W, 25C-W, and 28C-W carbon fiber anodes delivered charge capacities of 185, 194, and 214 mAh g^{-1}, respectively. Fig. 32 shows the charge capacities of the three anodes for 100 cycles at 100 mA g^{-1}. The large drop in capacity after the first cycle can be attributed to the high surface area of the fibers and the growth of the solid electrolyte interphase (SEI) layer on the electrode surface. As a result, the coulombic efficiency at the first cycle for the 20C-W, 25C-W, and 28C-W was 39.8, 34.2, and 44.4 %, while the coulombic efficiencies reached 99.6, 99.3, and 99.6%, respectively, after 100 cycles.
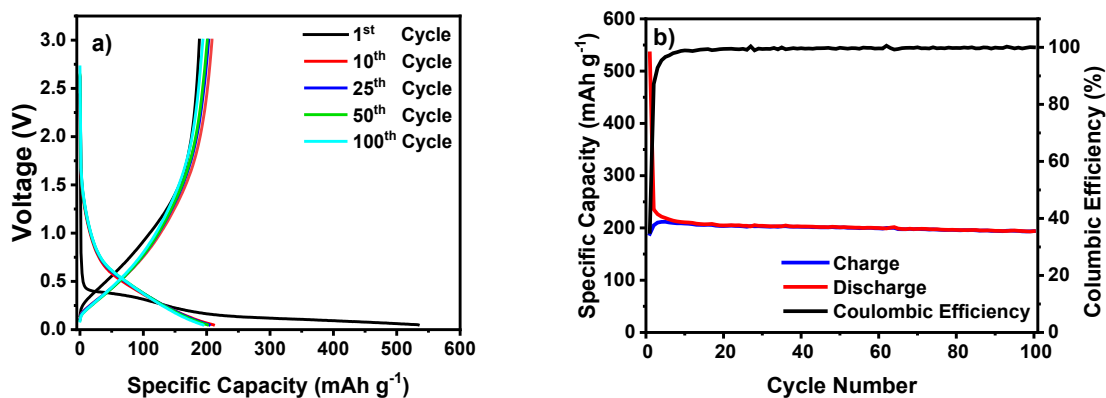

Fig. 31. a) Charge-discharge and b) cycle performance for 25C-W anodes in half-cell LIB.
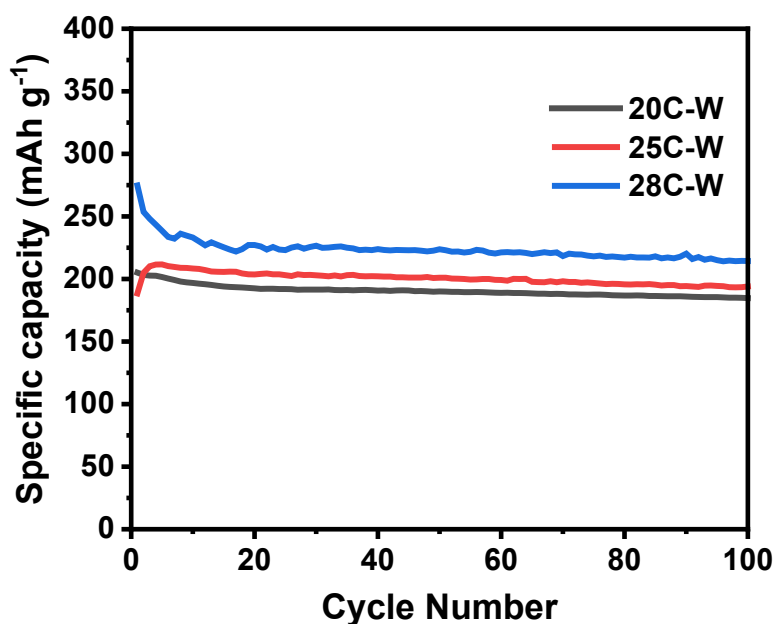
Fig. 32. Specific charge capacity for the 20C-W, 25C-W, and 28C-W carbon fibers in half-cell LIBs.

6.2.2.2. Carbon Fibers Anodes in SIBs

The charge-discharge profiles and cycle performance of the 25C-W carbon-fiber anodes in Na-ion half cells are shown in Fig. 33. The charge-discharge plots and cycle performance for the 20C-W and 28C-W carbon-fiber anodes in SIBs had similar profiles and their plots can be found in Figures A10a and A10b of the appendix. The charge capacity vs. cycle performance plots for the 20C-W, 25C-W, and 28C-W anodes in SIBs are shown in Fig. 34. The galvanostatic charge-discharge experiments were performed at a current density of 100 mA g^{-1}. At the 1st cycle, the 20C-W, 25C-W, and 28C-W anodes delivered a charge capacity of 90, 86, and 95 mAh g^{-1}, respectively. After 100 cycles, the 20C-W, 25C-W, and 28C-W carbon-fiber anodes delivered charge capacities of 54, 56, and 53 mAh g^{-1}, respectively. As expected, the capacity of the SIBs is lower than that observed in LIBs. This can be due to the sluggish Na-ion insertion, the larger size of Na-ions, and SEI formation at the first cycle. Finally, the coulombic efficiency at the first

cycle for the 20C-W, 25C-W, and 28C-W was 40.8, 41.5, and 43.6 %. After 100 cycles, the

coulombic efficiency reached values of 99.8, 99.9, and 99.8%, respectively. In SIBs, the fiber

diameter deviations seemed to not play an impactful role in the electrochemical performance.

Thus, further investigation of the effect of fiber diameter on the sodiation-desodiation process
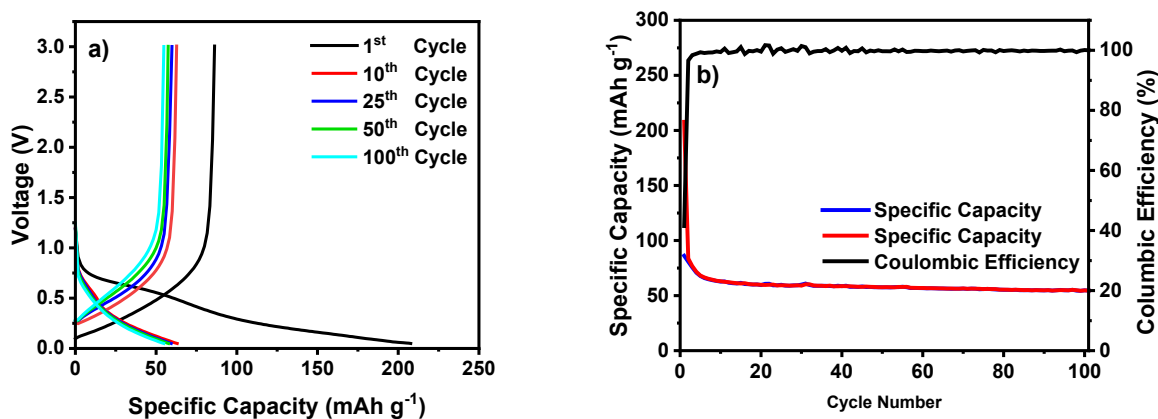
needs to be conducted

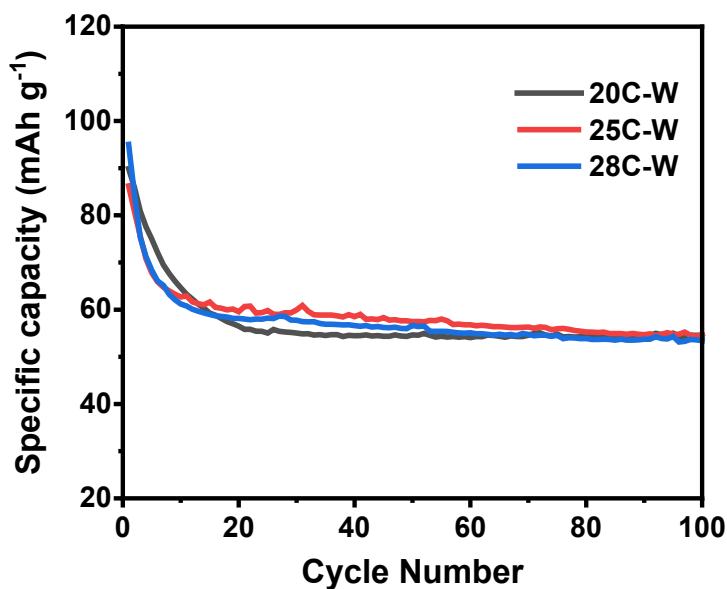**Fig. 33.** a) Charge-discharge and b) cycle performance for 25C-W anodes in Na-ion half-cell.

Fig. 34. Specific charge capacity for the 20C-W, 25C-W, and 28C-W carbon fibers in half-cell SIBs.

6.2.2.3. Composite TiO$_2$/C Anodes in LIBs

The 28C/15TiO$_2$-W, 28C/25TiO$_2$-W, and 28C/35TiO$_2$-W composite-fiber anodes delivered an initial capacity of 228, 148, and 203 mAh g^{-1}, respectively (Fig. 36). After the first cycle, the 22C/TiO$_2$-W composite anodes maintained a consistent capacity and after 100 cycles they delivered charge capacities of 147, 109, and 145 mAh g^{-1}, respectively. On the other hand, the 22C/15TiO$_2$-W:E, 22C/25TiO$_2$-W:E, and 22C/35TiO$_2$-W:E composite-fiber anodes delivered an initial capacity of 43, 20, and 57 mAh g^{-1}, and after 100 cycles, they delivered charge capacities of 103, 85, and 104 mAh g^{-1}, respectively.

Fig. 35a, Fig. 35b, and Fig. 35c show the charge-discharge profiles for 28C/25TiO$_2$-W, 22C/25TiO$_2$-W:E, and 12C/25TiO$_2$-E, respectively, to compare their profiles. It is seen that only the composite fibers prepared with ethanol generated charge profiles characteristic of TiO$_2$. An observation between the capacity profile of 28C/TiO$_2$-W and 22C/TiO$_2$-W:E is the higher capacity output of the 28C/TiO$_2$-W. This is accredited to the smaller fiber diameter rather than the presence of TiO$_2$ in the fibers since there is no capacity plateau at ~2.1V of TiO$_2$ during delithiation [132]. This is also supported by the lack of TiO$_2$ working voltage peaks in the CV plots for the 28C/TiO$_2$-W anodes (Fig. 28a, Fig. 28b, and Fig. 28c). Although interactions between the active material and working electrode can be observed to some degree in the CV plots for the C/TiO$_2$-W:E anodes (Fig. 29a and Fig. 29c), the charge-discharge profiles for 22C/TiO$_2$-W:E did not reveal a plateau for TiO$_2$ in the plots. Even if more active material could have been exposed in C/TiO$_2$-W:E anodes, their larger fiber diameter limited their overall surface area, leading to an overall lower capacity. For further reference, the charge/discharge

plots for 28C/15TiO₂-W and 28C/35TiO₂-W are shown in Figures A11a and A11b while the charge/discharge plots for 22C/15TiO₂-W:E and 22C/35TiO₂-W:E are shown in Figures A12a and A12b. The charge/discharge plots for 12C/15TiO₂-E and 12C/35TiO₂-E are shown in Figures A13a and A13b. Finally, Fig. 36 and Fig. 37 show the charge capacities of all three TiO₂ compositions in C/TiO₂-W and C/TiO₂-W:E anodes, respectively. In general, higher specific charge capacities were delivered by the 28C/TiO₂-W anodes. However, the higher capacity of the C/TiO₂-W composite carbon-fibers is attributed to the smaller diameter of the carbon fibers which in turn increased the carbon surface area readily available for lithiation/delithiation.
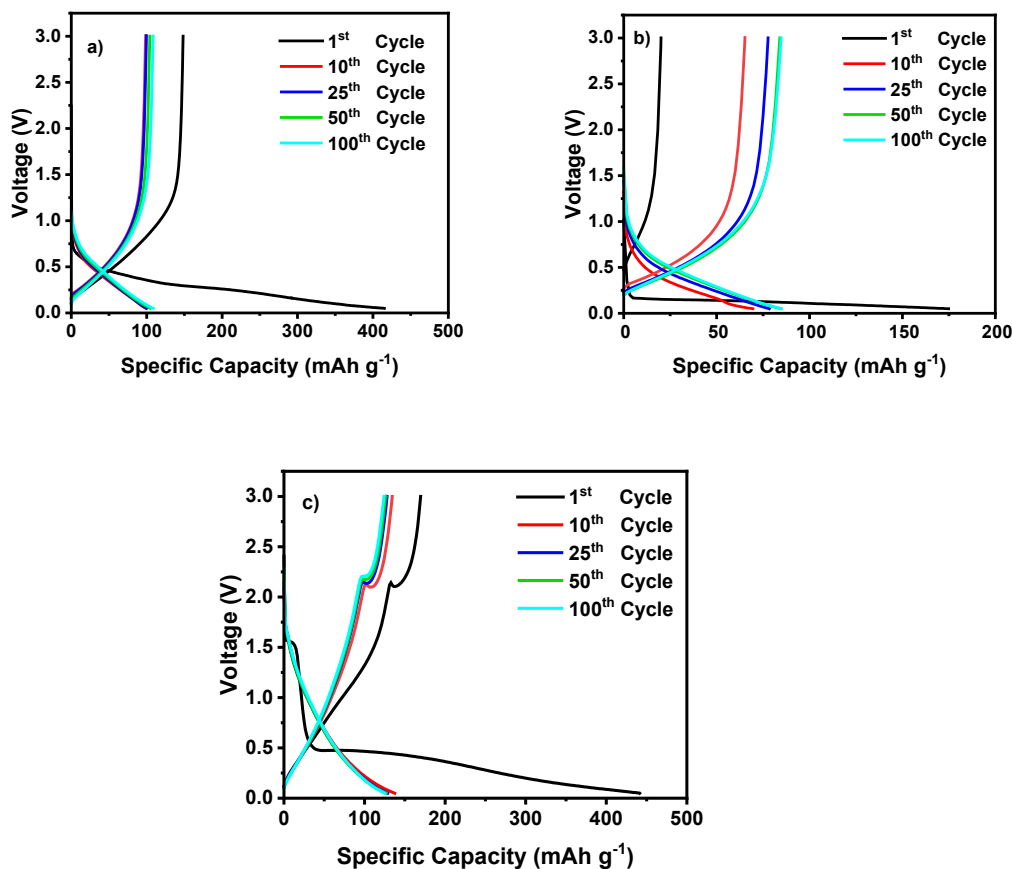

Fig. 35. Charge-discharge profiles of a) 28PVP/25TiO2-W, b) 22PVP/25TiO2-W:E, and c) 12C/25TiO2-E composite fiber anodes in Li-ion half-cells.
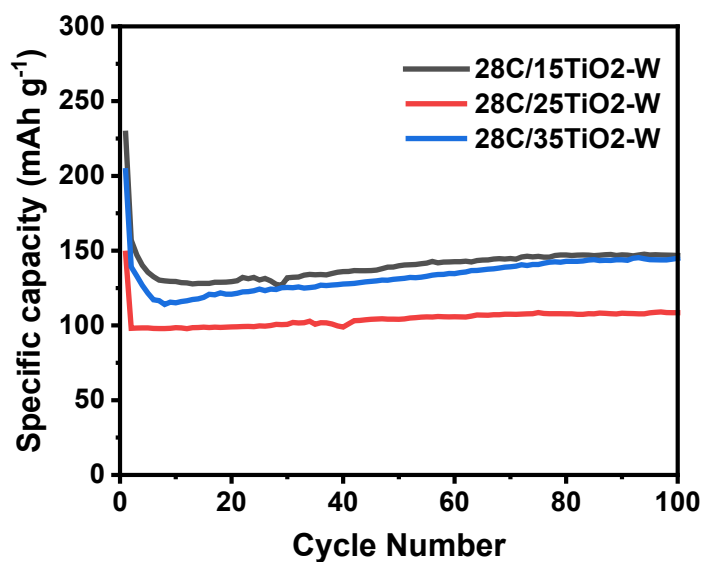
Fig. 36. Specific charge capacity for 28C/15TiO2-W, 28C/25TiO2-W, and 28C/35TiO2-W composite-fiber anodes in Li-ion half-cells.
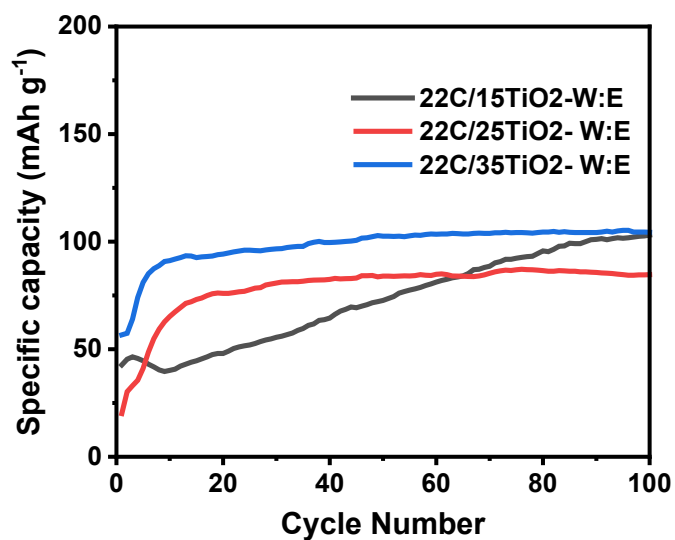

Fig. 37. Specific charge capacity for 22C/15TiO2-W:E, 22C/25TiO2- W:E, and 22C/35TiO2-W:E composite-fiber anodes in Li-ion half-cells.

6.2.2.4. Composite Sn/C Anodes in LIBs

The 22PVP/10Sn-W:E and 22PVP/15Sn-W:E composite-fiber anodes delivered an initial capacity of 49 and 105 mAh g^{-1} (Fig. 39). A capacity increment took place in the following

cycles. After 100 cycles, the 22PVP/10Sn-W:E and 22PVP/15Sn-W:E composite-fiber anodes

delivered a capacity of 142 mAh g^{-1}, and 133 mAh g^{-1}, respectively. For the 22PVP/10Sn-W:E

(Fig. 38a) there were no significant plateaus distinctive of Sn as the active material. This lack of

Sn/Li-ion interaction explains the low initial capacity during the first cycle compared to the

initial capacity of Sn-based anodes reported as reported in the literature [24]. On the other hand,

the 22PVP/15Sn-W:E composite-fiber anodes (Fig. 38b) revealed almost straight charge lines

that validated the presence of Sn particles in the lithiation process. Thus, the higher active

material loading enabled the interaction between the working electrode (Li-ion) and the active

material (Sn). Small plateaus are observed at ~0.6 and ~0.9 V which agrees with results reported

in the literature and the observed oxidation peaks during the anodic scan of CVs in Fig. 30b

[133]. A charge-discharge plot for 12PVP/15Sn-E composite fiber-anodes was also included in

Fig. 38c to compare its charge-discharge profile with the one revealed by the 22PVP/15Sn-W:E

composite carbon-fibers. It can be observed that the 22PVP/15Sn-W:E generated a similar

profile as the 12PVP/15Sn-E. However, the overall delivered capacity was lower in

22PVP/15Sn-W:E than 12PVP/15Sn-E. Previous studies have developed carbon fibers from 15

wt.% PVP in ethanol using centrifugal spinning and these carbon fibers had an average diameter

of 1.99 μm [28]. Thus, the better particle dispersion in ethanol could have improved the

electrochemical performance of the 12PVP/15Sn-E despite the large fiber diameter. Finally, the

charge capacities for the 22PVP/10Sn-W:E and 22PVP/15Sn-W:E composite-fiber anodes in

LIBs are shown in Fig. 39 to compare their capacities as a function of cycle number
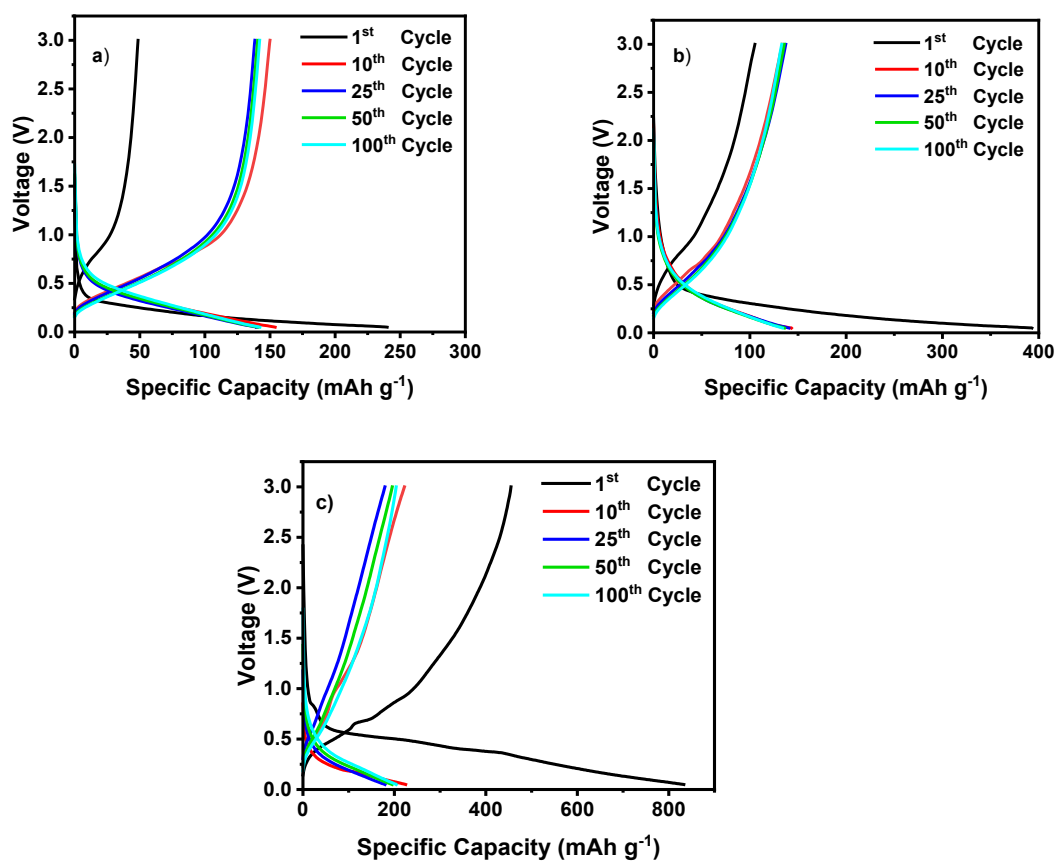
Fig. 38. Charge-discharge profiles of a) 22PVP/10Sn-W:E, b) 22PVP/15Sn-W:E, and c) 12PVP/15Sn-E composite fiber anodes in Li-ion half-cells.
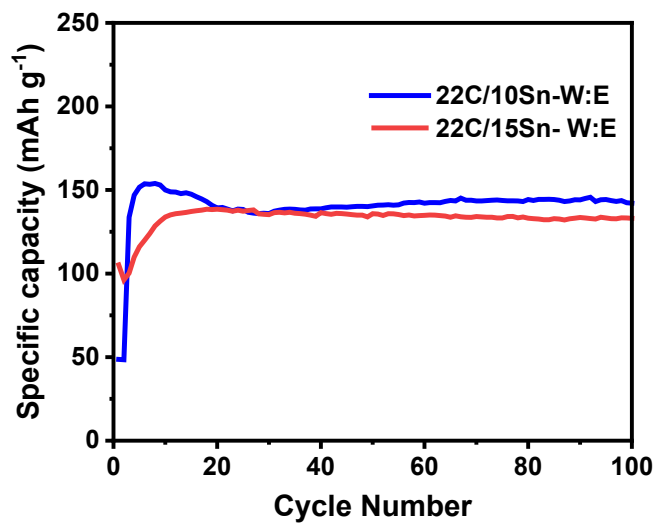

Fig. 39. Specific charge capacity for 22C/10Sn-W:E, and 22C/15Sn- W:E composite-fiber anodes in Li-ion half-cells.

6.2.3. Rate performance

6.2.3.1. Carbon Fiber Anodes for LIBs

Fig. 40 shows the rate performance of the 20C-W, 25C-W, and 28C-W anodes at current densities of 50, 100, 200, 400, 500, and back to 50 mA g^{-1} in a voltage range between 0.01 and 3.0 V. These current densities and voltage range were applied to22 all the anode materials presented in this work. The results show that the charge capacity decreases as the current rate increases due to the faster rates of lithiation/delithiation that overwhelm the pace of insertion/disinsertion of Li-ions into the electrodes. It is also observed that the specific capacity at higher current rates decreases more rapidly for the carbon-fibers anodes prepared from PVP solutions with higher concentrations; this can be attributed to their larger fiber diameter. In these anodes, the larger fibers become a bottleneck during faster rates due to less available surface area for lithiation. Nonetheless, the 28C-W also delivered the highest capacities at lower current densities. It is speculated that the higher polymer concentrations yielded carbon fibers with a higher carbon density. Thus, the higher carbon contents enabled more lithium to diffuse and accommodate in the anode material when the pace of lithiation did not overwhelm the anode's surface area. After cycling back to 50 mA g^{-1}, the 20C-W, 25C-W, and 28C-W carbon-fiber anodes recovered ~96.9, ~94.2, and ~96.9 % of their initial capacity during the first 10 cycles at 50 mAh g^{-1}, respectively. Moreover, the anodes also delivered a flat capacity at each current rate. This was expected since there is not an added active material that could produce anode pulverization after cycling caused by excessive volume change.
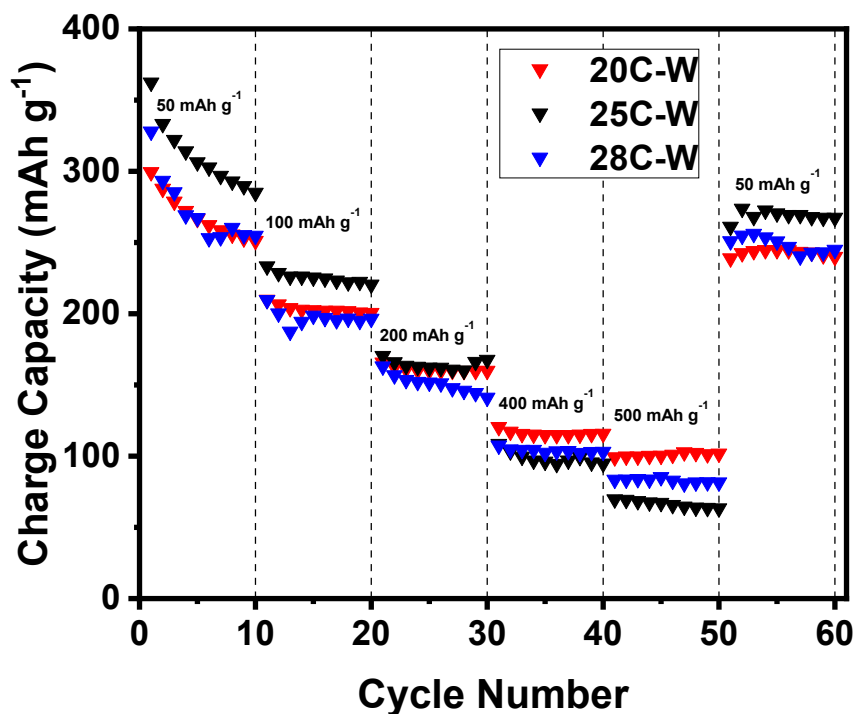
Fig. 40. Specific charge capacity for the 20C-W, 25C-W, and 28C-W carbon fibers in Li-ion half-cells.

6.2.3.2. Carbon Fibers Anodes for SIBs

Fig. 41 shows the rate performance of the 20C-W, 25C-W, and 28C-W anodes in Na-ion half cells. Compared to the rate performance of the C-W anodes in LIBs, the overall charge capacity delivered by the anodes in SIBs is lower at each current density, presumably due to sluggish Na-ion kinetics and its larger ion size. Similar to the anode behavior in LIBs, the 28C-W anode showed the best performance at lower current densities. However, fiber diameter did not increase the rate of capacity loss at higher current densities as it did in LIBs. After cycling back to 50 mA g^{-1}, the 20C-W, 25C-W, and 28C-W carbon-fiber anodes recovered ~122, ~94, and ~89 % of their initial capacity during the first 10 cycles at 50 mAh g^{-1}.
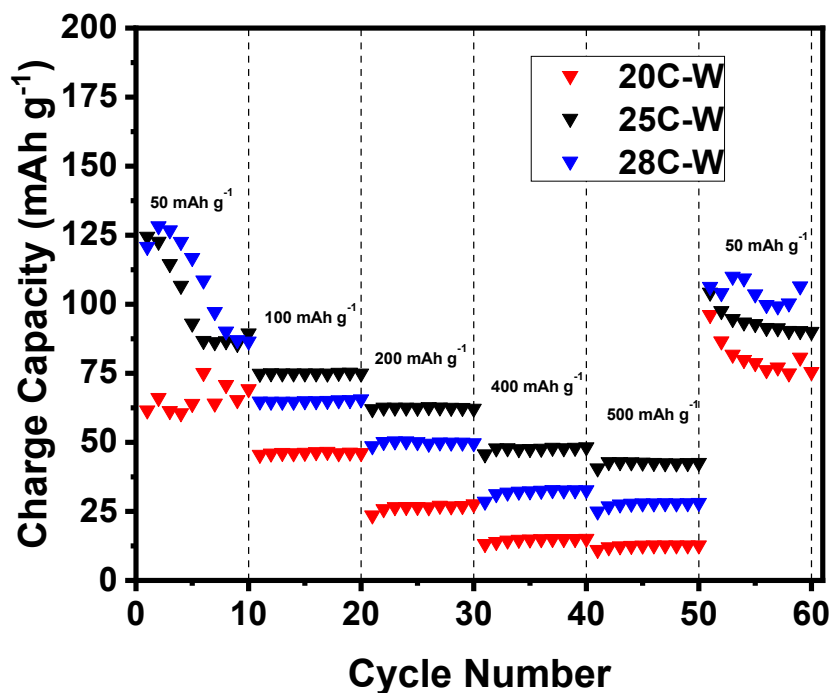
Fig. 41. Specific charge capacity for the 20C-W, 25C-W, and 28C-W carbon fibers in Na-ion half cells.

6.2.3.3. Composite TiO₂/C Anodes for LIBs

Fig. 42 and Fig. 43 show the rate performance for the 28C/TiO₂-W and 22C/ TiO₂-W:E composite-fiber anodes, respectively. After cycling back to 50 mA g^{-1}, the 28C/TiO₂-W composite-fiber anodes recovered ~98, 106, and ~94 % of their initial capacity during the first 10 cycles at 50 mA g^{-1}. Similarly, the 22C/ TiO₂-W:E recovered ~112, ~106, and ~101 %. As seen in the figures, the 22C/ TiO₂-W:E suffered a higher capacity loss at higher current rates due to their larger fiber diameter. Among the 28C/TiO₂-W anodes, the 28C/25TiO₂-W suffered the highest loss in capacity since they had the largest fiber average diameter (Fig. 18). Similarly, among the 22C/ TiO₂-W:E, the 22C/ 15TiO₂-W:E suffered the largest capacity drop due because they possess the largest average diameter (Fig. 18).
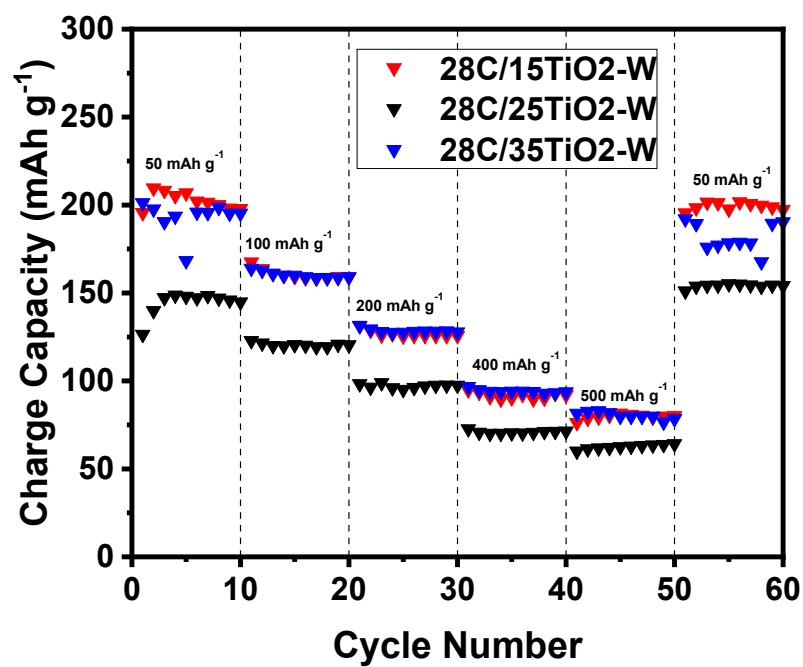
Fig. 42. Rate performance for 28C/15TiO2-W, 28C/25TiO2-W, and 28C/35TiO2-W composite-fiber anodes in Li-ion half cells.
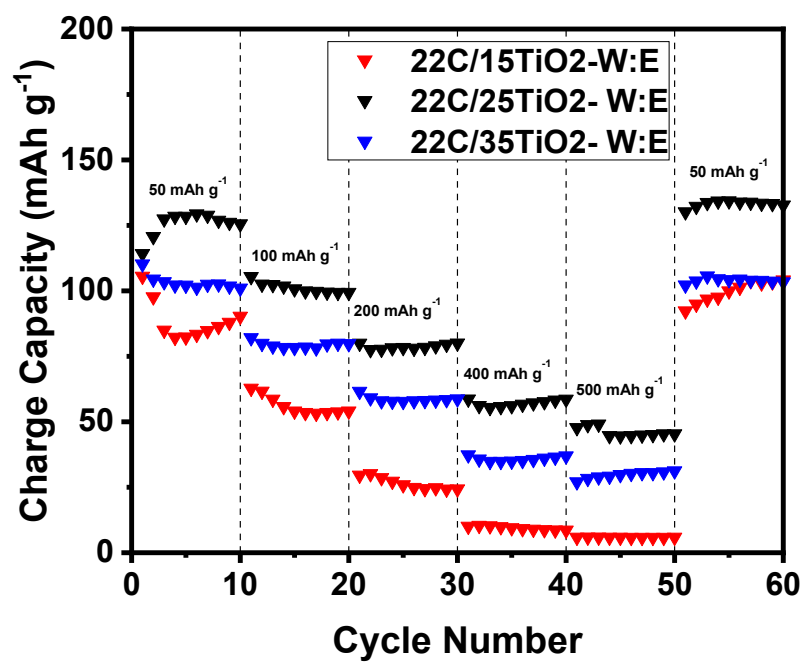

Fig. 43. Rate performance for 22C/15TiO2-W:E, 22C/25TiO2- W:E, and 22C/35TiO2- W:E composite-fiber anodes in Li-ion half cells.

6.2.3.4. Composite Sn/C Anodes for LIBs

The 22C/10Sn-W:E, and 22C/15Sn-W:E composite fiber anodes had a promising start. However, they quickly collapsed after failing to deliver a notable capacity at 200 mA g^{-1} (Fig. 44). This collapse was expected due to the intrinsic large volume expansion of Sn [134], the large fiber diameter, and the lack of as hollow or porous fiber morphology to buffer the volume expansion. The 22C/Sn-W:E anodes were capable of delivering ~72 and ~91% of their initial capacity during the first 10 cycles. Even though these anodes can operate at low current rates, their charging/discharging rate and relatively low specific capacity cannot satisfy the expected performance expected in today's market.
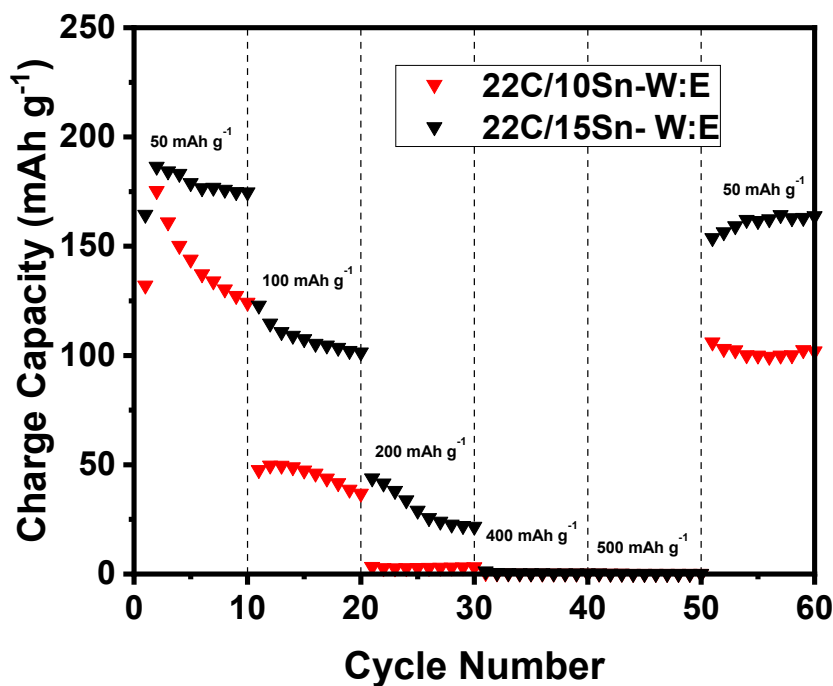

Fig. 44. Rate Performance for 22C/10Sn-W:E, and 22C/15Sn- W:E composite-fiber anodes in Li-ion half cells.

6.2.4. Impedance Spectroscopy

6.2.4.1. Carbon Fiber Anodes for LIBs

The electrochemical impedance spectroscopy (EIS) results for the 20C-W, 25C-W, and 28C-W fiber anodes in LIBs showed a predictable behavior. All these anodes had a similar initial impedance due to ion transfer in the electrolyte solution which occurs before the onset of the semicircles observed in Fig. 45. The diameter of the semicircles in Fig. 45 increases with increasing fiber diameter. This is expected since the lower surface area decreases the space available for electrode/electrolyte interface interactions such as Li-ion/electrolyte solvent separation (forming Li^+ during this process), Li-cation diffusion through the surface of the anode, and finally, Li-cation intercalation with the host material, which is represented by the straight line at the end of the semicircle (i.e., Warburg impedance, diffusion) [135], [136], [134].
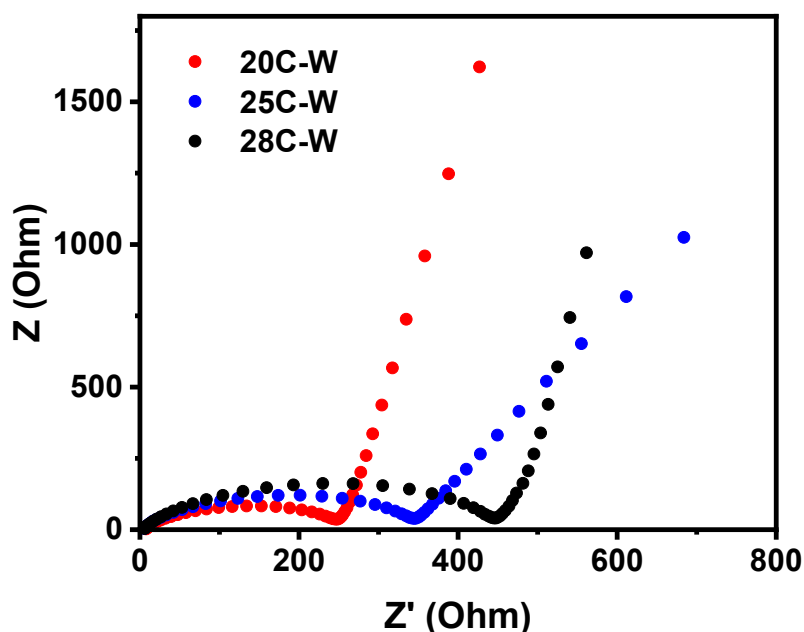

Fig. 45. Impedance spectroscopy for the 20C-W, 25C-W, and 28C-W carbon fibers in Li-ion half cells.

6.2.4.2. Carbon Fibers Anodes for SIBs

The SIBs produced impedance plots with inconsistent range patterns. The impedance plots shown in Fig. 46 were selected because they had the closest ranges to each other. Nonetheless, three consistent behaviors were noticed. The range of the semicircles in SIBs were smaller than in SIBs. Thus, the resistance on the electrolyte/electrode interface was smaller in SIBs than in LIBs. However, the resistance due to ion transfer in the electrolyte becomes a larger portion of the overall electrode transfer resistance. Finally, good electron and ion mobility within the anode material was obtained since the three semicircles intercepted the real axis at the end of their semicircles and steep diffusion lines were formed.
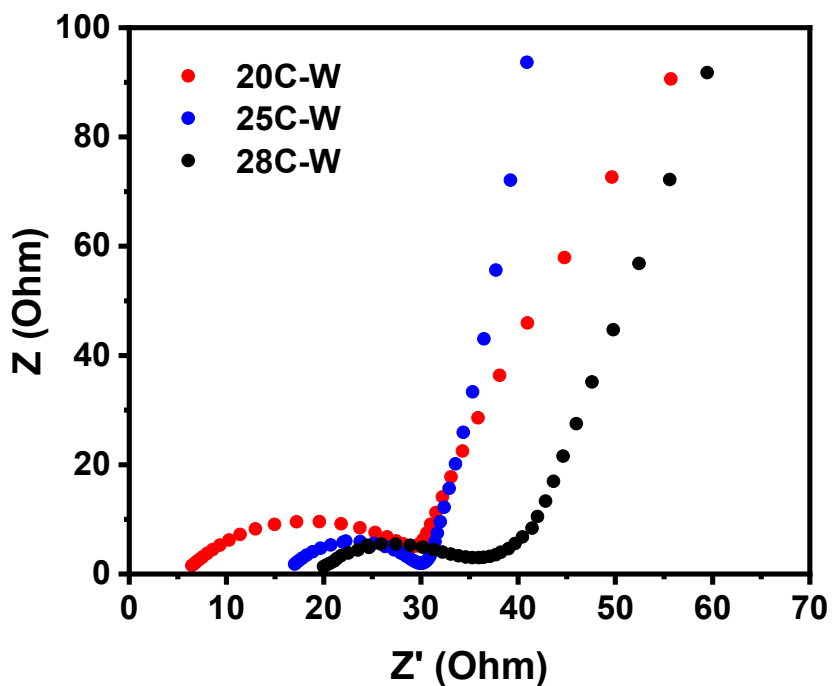

Fig. 46. Impedance spectroscopy for the 20C-W, 25C-W, and 28C-W carbon fibers in Na-ion half cells.

6.2.4.3. Composite TiO$_2$/C Anodes for LIBs

The EIS plots of the 28C/15TiO$_2$-W, 28C/25TiO$_2$-W, and 28C/35TiO$_2$-W composite-fiber anodes in Li-ion half cells had very similar behavior to the carbon-fiber anodes in LIBs. This can be explained by the lack of TiO$_2$/Li-ion interaction observed in their CVs and charge-discharge profiles of these anodes. EIS further corroborates the lack of interaction of these two composite-fiber anodes. The impedance plots for the 22C/15TiO$_2$-W:E, 22C/25TiO$_2$- W:E, and 22C/35TiO$_2$- W:E composite-fiber anodes in Li-ion half cells have a similar range in the real axis to those observed in the 28C/15TiO$_2$-W anodes. However, Fig. 48 shows that Z' intercepts at the end of the semicircles are not achieved due to the electronic flow resistance within the anode materials.
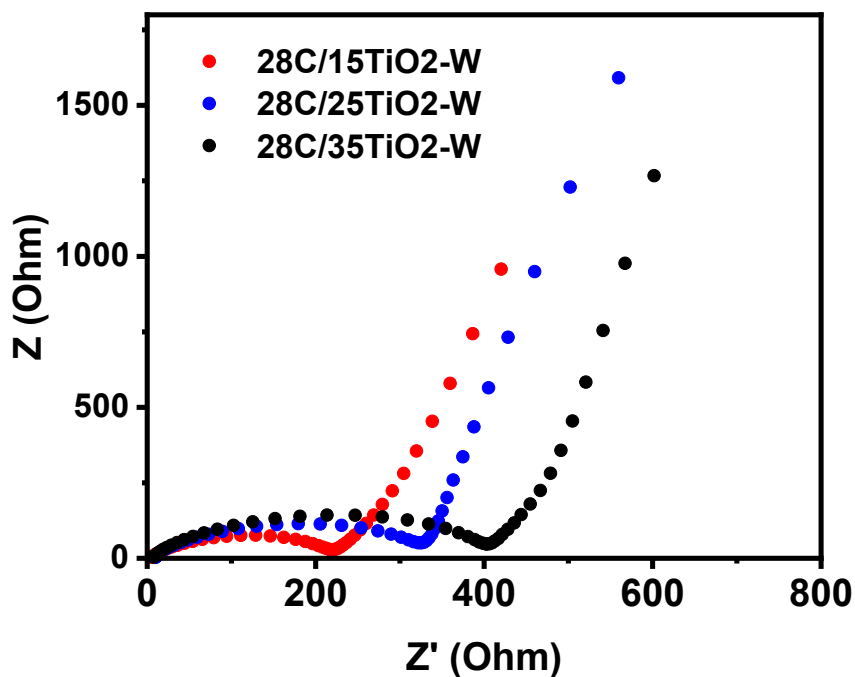

Fig. 47. Impedance spectroscopy for 28C/15TiO2-W, 28C/25TiO2-W, and 28C/35TiO2-W composite-fiber anodes in Li-ion half cells.
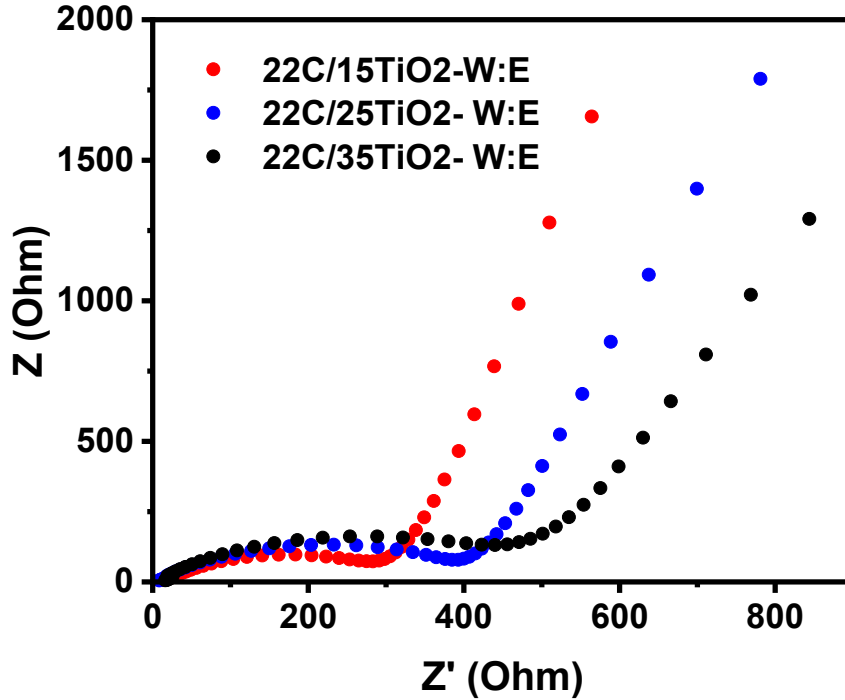
Fig. 48. Impedance spectroscopy for 22C/15TiO2-W:E, 22C/25TiO2- W:E, and 22C/35TiO2-W:E composite-fiber anodes in Li-ion half cells.

6.2.4.4. Composite Sn/C Anodes for LIBs

In the case of the 22C/10Sn-W:E anode, a similar range to those obtained in the 22C/TiO$_2$- W:E anodes was observed. Presumably, the similar impedance profile can also be attributed to the lack of active material interaction with the working electrode and the lower conductivity achieved in the composite fibers fabricated with the solvent mixture. However, in Fig. 49, a slightly smaller semicircle and z' axis intersection are observed for the 22C/15Sn-W:E anode, proving a better electronic conductance in anodes where the presence of Sn played a role. More importantly, the diffusion line is slanted with a smaller angle between the real axis. This sluggish diffusion of the Li-ions in the electrode can be attributed to the slower lithiation mechanism of alloying-based reaction materials such as Sn, whose atomic structure must be modified to host more Li-ions.
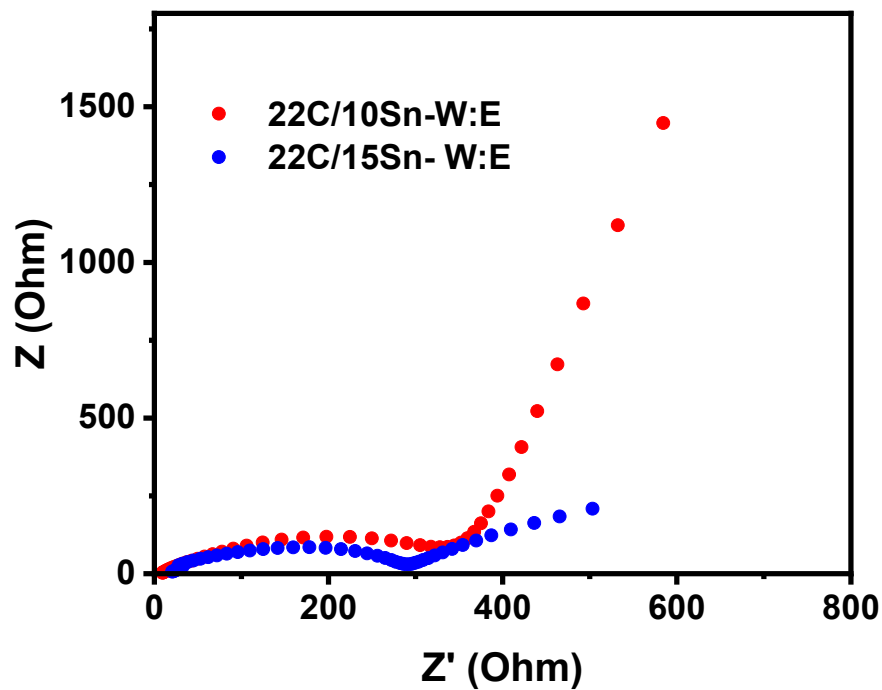
Fig. 49. Impedance spectroscopy for 22C/10Sn-W:E, and 22C/15Sn- W:E composite-fiber anodes in Li-ion half cells.

CHAPTER VII

CONCLUSIONS

In this work, a higher production rate of nanofibers from aqueous PVP solutions was achieved using centrifugal spinning and subsequent thermal treatment. Solutions with PVP concentrations of 10, 15, 20, 25, and 28 wt.% were prepared, of which only the 20, 25, and 28 wt.% produced fibers. Although beads were less apparent in lower concentration solutions, the highest fiber yield was achieved at 25 wt.% PVP. Moreover, at PVP concentration of 25 wt.%, the fiber formation was not affected by higher humidity levels. Flexible carbon fibers were produced from the 20, 25, and 28 wt.% PVP precursor fibers using a novel three-step heat treatment which reduced the volume shrinkage due to the high temperature (700 °C) used during the carbonization process.

Composite carbon fibers were also prepared with TiO_2 in aqueous polymer solutions. However, inconsistent fiber yield during spinning and the unsuccessful production of Sn composite fibers from aqueous polymer solutions led to the implementation of a 1:1 (wt./wt.) water:ethanol solvent mixture to achieve the consistent formation of composite fibers by centrifugal spinning. However, the increase in vapor pressure, due to the addition of ethanol, yielded fibers with a larger than desired diameter and as a result, the electrochemical performance of the batteries decayed. On the other hand, the electrochemical performance of the C/TiO_2 composite-fiber anodes (28C/TiO2-W) prepared from aqueous solutions did not suffer a

decrease in electrochemical performance as large as the anodes prepared with the water:ethanol mixture. However, the higher capacity of 28C/TiO2-W was mainly attributed to their smaller fiber diameters and the interaction of carbon with the working electrode rather than the ceramic nanoparticles.

Among the possible reasons for the unsuccessful formation of Sn and TiO_2 composite fibers, the properties of the aqueous solutions, namely the high surface tension of water and poor particle dispersion in aqueous solutions, are some of the issues encountered during this research.

Nevertheless, successful fiber formation using aqueous PVP solutions was achieved at high production rates, opening the doors for the exploration of composite fiber production from aqueous PVP solutions at high rates. Given these results, a new venue to produce binder-free carbon composite anodes from aqueous polymer solutions at a larger scale can be pursued to reduce the environmental impact and the health hazards encountered during the production of fibers. Moreover, this work lays a foundation for the development of high rate composite nanofibers production using water as the sole solvent.

7.1. Future Work

Future research will be performed on the effect of higher angular velocities to accelerate the solvent's evaporation rate by forced convection without altering the intrinsic properties of water. It is not recommended to try to increase the vapor pressure of the solvent as the larger vapor pressure leads to larger viscosities at the tip of the nozzle during spinning and produces fibers with larger diameters. If the capabilities of the centrifugal spinning equipment do not allow higher than 10,000 rpm, a longer distance between the center of the spinneret to the nozzle tip can be retrofitted in the equipment to increase the solvent's evaporation rate by force convection

without increasing the angular velocity. Alternatively, the evaporation rate of water can be increased by decreasing the humidity of the production environment [118].

In addition, mechanical homogenization before centrifugal spinning is also recommended when using aqueous PVP solutions to increase particle dispersion. Similarly, the mechanical homogenization in mixture based (water:ethanol) solutions before centrifugal spinning is also recommended since 12C/TiO$_2$-E and 12C/Sn-E composite fibers revealed charge-discharge profiles distinctive of TiO$_2$ and Sn despite the large fiber diameter (1.99 μm) of 15C-E carbon fibers reported in the literature [28].

Methods to incorporate nanoparticles in the precursor fibers could also be explored by introducing the nanoparticles in the fiber membrane rather than in the precursor solution. For example, during this research, composite PVP/water and PVA/Si/water fibers were produced using two Forcespining cyclones to prepare multilayer membranes. However, the electrochemical performance of the composite carbon fibers prepared from these membranes collapsed due to the volume expansion of silicon. However, an interesting morphology was observed in SEM images. On some occasions, the different degradation rates of PVA and PVP enabled the merging of composite PVA/Si fibers and PVP fibers after annealing. Nonetheless, the Si/C composite fibers separated from the PVP-based carbon fibers after carbonization.

At the beginning of this work, multiple water-soluble polymers were used to produce composite carbon fibers. PEO was among those options because it is water-soluble and composite fibers have been successfully prepared using centrifugal spinning in the past with this polymer. However, PEO degrades and cannot be carbonized. Thus, multilayer fibers prepared from aqueous PVP and composite PEO aqueous solutions could lead to the dispersion of

particles on PVP-based carbon fibers owing to the complete degradation of PEO on the PVP carbon fibers.

Finally, centrifugally spun porous and hollow fibers prepared from aqueous polymer solutions and their use as binder-free anodes in LIBs and SIBs need to be investigated. Hollow PVP fibers have been previously produced with centrifugal spinning and ethanol as the solvent [27].To achieve this goal, mineral oil was added to the solution to produce a phase separation during the stretching of the solution jet with polymer-rich and polymer-lean phases. However, oil and water are immiscible. Emulsions with oil and water can be achieved using surfactants such as sodium dodecyl sulfate (SDS). Attempts to emulsify oil and water were performed in this work. However, more work needs to be done to determine the optimum oil:water:SDS ratios to avoid producing a wax-like solution that did not produce fibers. As discussed above, there are many alternatives yet need to be explored for the successful production of composite fibers. To achieve this, novel procedures need to be developed.

REFERENCES

[1] Z.G. Yang, J.L. Zhang, M.C.W. Kintner-Meyer, X.C. Lu, D.W. Choi, J.P. Lemmon, J. Liu, Electrochemical Energy Storage for Green Grid, Chemical Reviews, 111 (2011) 3577-3613.

[2] Y.D.I. Abu-Lebdeh, Nanotechnology for Lithium-Ion Batteries, Springer Science+Business Media, Ottawa, 2013.

[3] C.F. Liu, Z.G. Neale, G.Z. Cao, Understanding electrochemical potentials of cathode materials in rechargeable batteries, Mater Today, 19 (2016) 109-123.

[4] F. Keck, M. Lenzen, A. Vassallo, M.Y. Li, The impact of battery energy storage for renewable energy power grids in Australia, Energy, 173 (2019) 647-657.

[5] M.D. Slater, D. Kim, E. Lee, C.S. Johnson, Sodium-Ion Batteries, Adv Funct Mater, 23 (2013) 947-958.

[6] S. Tewari, Potential of Sodium-Sulfur Battery Energy Storage to Enable Further Integration of Wind, 2015.

[7] S. Tewari, Potential of Sodium-Sulfur Battery Energy Storage to Enable Further Integration of Wind,Energy Storage for Smart Grids, DOI (2015) 67-95.

[8] M.A. Munoz-Marquez, D. Saurel, J.L. Gomez-Camer, M. Casas-Cabanas, E. Castillo-Martinez, T. Rojo, Na-Ion Batteries for Large Scale Applications: A Review on Anode Materials and Solid Electrolyte Interphase Formation, Adv Energy Mater, 7 (2017).

[9] N. Yabuuchi, K. Kubota, M. Dahbi, S. Komaba, Research Development on Sodium-Ion Batteries, Chem Rev, 114 (2014) 11636-11682.

[10] Z.F. Dai, U. Mani, H.T. Tan, Q.Y. Yan, Advanced Cathode Materials for Sodium-Ion Batteries: What Determines Our Choices?, Small Methods, 1 (2017).

[11] B.W. Xiao, T. Rojo, X.L. Li, Hard Carbon as Sodium-Ion Battery Anodes: Progress and Challenges, Chemsuschem, 12 (2019) 133-144.

[12] R. Nava, L. Cremar, V. Agubra, J. Sanchez, M. Alcoutlabi, K. Lozano, Centrifugal Spinning: An Alternative for Large Scale Production of Silicon-Carbon Composite Nanofibers for Lithium Ion Battery Anodes, Acs Appl Mater Inter, 8 (2016) 29365-29372.

[13] M. Ramalingam, S. Ramakrishna, Nanofiber Composites for Biomedical Applications, Woodh Publ Ser Biom, DOI (2017) Xvii-Xvii.

[14] L. Zuniga, G. Gonzalez, R.O. Chavez, J.C. Myers, T.P. Lodge, M. Alcoutlabi, Centrifugally Spun alpha-Fe2O3/TiO2/Carbon Composite Fibers as Anode Materials for Lithium-Ion Batteries, Appl Sci-Basel, 9 (2019).

[15] D. De la Garza, F. De Santiago, L. Materon, M. Chipara, M. Alcoutlabi, Fabrication and characterization of centrifugally spun poly(acrylic acid) nanofibers, J Appl Polym Sci, 136 (2019).

[16] V. Lukasova, M. Buzgo, K. Vocetkova, V. Sovkova, M. Doupnik, E. Himawan, A. Staffa, R. Sedlacek, H. Chlup, F. Rustichelli, E. Amler, M. Rampichova, Needleless electrospun and centrifugal spun poly-epsilon-caprolactone scaffolds as a carrier for platelets in tissue engineering applications: A comparative study with hMSCs, Mat Sci Eng C-Mater, 97 (2019) 567-575.

[17] M.D. Calisir, A. Kilic, A comparative study on SiO2 nanofiber production via two novel non-electrospinning methods: Centrifugal spinning vs solution blowing, Mater Lett, 258 (2020).

[18] B.A. Zhang, F.Y. Kang, J.M. Tarascon, J.K. Kim, Recent advances in electrospun carbon nanofibers and their application in electrochemical energy storage, Prog Mater Sci, 76 (2016) 319-380.

[19] L.W. Ji, Z. Lin, M. Alcoutlabi, X.W. Zhang, Recent developments in nanostructured anode materials for rechargeable lithium-ion batteries, Energ Environ Sci, 4 (2011) 2682-2699.

[20] C. Kim, K.S. Yang, M. Kojima, K. Yoshida, Y.J. Kim, Y.A. Kim, M. Endo, Fabrication of electrospinning-derived carbon nanofiber webs for the anode material of lithium-ion secondary batteries, Adv Funct Mater, 16 (2006) 2393-2397.

[21] M. Zhang, J. Wang, S. Chen, F. Wu, Electrospun Composite of Fe(3)o(4)/Cu Nanocrystals Encapsulated in Carbon Fibers as an Anode Material with High Rate Capability for Lithium Ion Batteries, Aer Adv Eng Res, 103 (2016) 380-385.

[22] P.Q. Wang, D. Zhang, F.Y. Ma, Y. Ou, Q.N. Chen, S.H. Xie, J.Y. Li, Mesoporous carbon nanofibers with a high surface area electrospun from thermoplastic polyvinylpyrrolidone, Nanoscale, 4 (2012) 7199-7204.

[23] L.T. Dong, G.W. Wang, X.F. Li, D.B. Xiong, B. Yan, B.X. Chen, D.J. Li, Y.H. Cui, PVP-derived carbon nanofibers harvesting enhanced anode performance for lithium ion batteries, Rsc Adv, 6 (2016) 4193-4199.

[24] V.A. Agubra, L. Zuniga, D. De la Garza, L. Gallegos, M. Pokhrel, M. Alcoutlabi, Forcespinning: A new method for the mass production of Sn/C composite nanofiber anodes for lithium ion batteries, Solid State Ionics, 286 (2016) 72-82.

[25] J. Spender, A.L. Demers, X.F. Xie, A.E. Cline, M.A. Earle, L.D. Ellis, D.J. Neivandt, Method for Production of Polymer and Carbon Nanofibers from Water-Soluble Polymers, Nano Lett, 12 (2012) 3857-3860.

[26] L. Fei, B.P. Williams, S.H. Yoo, J. Kim, G. Shoorideh, Y.L. Joo, Graphene Folding in Si Rich Carbon Nanofibers for Highly Stable, High Capacity Li-Ion Battery Anodes, Acs Appl Mater Inter, 8 (2016) 5243-5250.

[27] L. Zuniga, V. Agubra, D. Flores, H. Campos, J. Villareal, M. Alcoutlabi, Multichannel hollow structure for improved electrochemical performance of TiO2/Carbon composite nanofibers as anodes for lithium ion batteries, J Alloy Compd, 686 (2016) 733-743.

[28] D. Flores, J. Villarreal, J. Lopez, M. Alcoutlabi, Production of carbon fibers through Forcespinning (R) for use as anode materials in sodium ion batteries, Mater Sci Eng B-Adv, 236 (2018) 70-75.

[29] J. Villarreal, R.O. Chavez, S.A. Chopade, T.P. Lodge, M. Alcoutlabi, The Use of Succinonitrile as an Electrolyte Additive for Composite-Fiber Membranes in Lithium-Ion Batteries, Membranes-Basel, 10 (2020).

[30] H.T. Niu, J. Zhang, Z.L. Xie, X.G. Wang, T. Lin, Preparation, structure and supercapacitance of bonded carbon nanofiber electrode materials, Carbon, 49 (2011) 2380-2388.

[31] M. Akia, N. Salinas, S. Luna, E. Medina, A. Valdez, J. Lopez, J. Ayala, M. Alcoutlabi, K. Lozano, In situ synthesis of Fe3O4-reinforced carbon fiber composites as anodes in lithium-ion batteries, J Mater Sci, 54 (2019) 13479-13490.

[32] I.M. Szilagyi, E. Santala, M. Heikkila, M. Kemell, T. Nikitin, L. Khriachtchev, M. Rasanen, M. Ritala, M. Leskela, Thermal study on electrospun polyvinylpyrrolidone/ammonium metatungstate nanofibers: optimising the annealing conditions for obtaining WO3 nanofibers, J Therm Anal Calorim, 105 (2011) 73-81.

[33] Z.J.Z. P. Arora, Battery separators, Chem Rev, DOI.

[34] V.A. Agubra, D. De la Garza, L. Gallegos, M. Alcoutlabi, ForceSpinning of polyacrylonitrile for mass production of lithium-ion battery separators, J Appl Polym Sci, 133 (2016).

[35] X.W. Zhang, L.W. Ji, O. Toprakci, Y.Z. Liang, M. Alcoutlabi, Electrospun Nanofiber-Based Anodes, Cathodes, and Separators for Advanced Lithium-Ion Batteries, Polym Rev, 51 (2011) 239-264.

[36] L.W. Ji, P. Meduri, V. Agubra, X.C. Xiao, M. Alcoutlabi, Graphene-Based Nanocomposites for Energy Storage, Adv Energy Mater, 6 (2016).

[37] M.T. McDowell, S.W. Lee, W.D. Nix, Y. Cui, 25th Anniversary Article: Understanding the Lithiation of Silicon and Other Alloying Anodes for Lithium-Ion Batteries, Adv Mater, 25 (2013) 4966-4984.

[38] J.T. Li, Z.Y. Wu, Y.Q. Lu, Y. Zhou, Q.S. Huang, L. Huang, S.G. Sun, Water Soluble Binder, an Electrochemical Performance Booster for Electrode Materials with High Energy Density, Adv Energy Mater, 7 (2017).

[39] Y. Lu, K. Fu, S. Zhang, Y. Li, C. Chen, J.D. Zhu, M. Yanilmaz, M. Dirican, X.W. Zhang, Centrifugal spinning: A novel approach to fabricate porous carbon fibers as binder-free electrodes for electric double-layer capacitors, J Power Sources, 273 (2015) 502-510.

[40] M. Dirican, X.W. Zhang, Centrifugally-spun carbon microfibers and porous carbon microfibers as anode materials for sodium-ion batteries, J Power Sources, 327 (2016) 333-339.

[41] T. Hou, X.L. Li, Y.S. Lu, B. Yang, Highly porous fibers prepared by centrifugal spinning, Mater Design, 114 (2017) 303-311.

[42] L. Xia, J.G. Ju, W. Xu, C.K. Ding, B.W. Cheng, Preparation and characterization of hollow Fe2O3 ultra-fine fibers by centrifugal spinning, Mater Design, 96 (2016) 439-445.

[43] J.J. Zhang, L.P. Yue, Q.S. Kong, Z.H. Liu, X.H. Zhou, C.J. Zhang, Q. Xu, B. Zhang, G.L. Ding, B.S. Qin, Y.L. Duan, Q.F. Wang, J.H. Yao, G.L. Cui, L.Q. Chen, Sustainable, heat-resistant and flame-retardant cellulose-based composite separator for high-performance lithium ion battery, Sci Rep-Uk, 4 (2014).

[44] M. Yanilmaz, Y. Lu, Y. Li, X.W. Zhang, SiO2/polyacrylonitrile membranes via centrifugal spinning as a separator for Li-ion batteries, J Power Sources, 273 (2015) 1114-1119.

[45] A.P. Wang, S. Kadam, H. Li, S.Q. Shi, Y. Qi, Review on modeling of the anode solid electrolyte interphase (SEI) for lithium-ion batteries, Npj Comput Mater, 4 (2018).

[46] E. Peled, D. Golodnitsky, G. Ardel, Advanced model for solid electrolyte interphase electrodes in liquid and polymer electrolytes, J Electrochem Soc, 144 (1997) L208-L210.

[47] J.B. Goodenough, Electrochemical energy storage in a sustainable modern society, Energ Environ Sci, 7 (2014) 14-18.

[48] X.J. Wang, Y.C. Liu, Y.J. Wang, L.F. Jiao, CuO Quantum Dots Embedded in Carbon Nanofibers as Binder-Free Anode for Sodium Ion Batteries with Enhanced Properties, Small, 12 (2016) 4865-4872.

[49] N.E. Zander, Formation of Melt and Solution Spun Polycaprolactone Fibers by Centrifugal Spinning, J Appl Polym Sci, 132 (2015).

[50] V. Subramanian, H.W. Zhu, B.Q. Wei, High rate reversibility anode materials of lithium batteries from vapor-grown carbon nanofibers, J Phys Chem B, 110 (2006) 7178-7183.

[51] L.W. Ji, Z. Lin, A.J. Medford, X.W. Zhang, Porous carbon nanofibers from electrospun polyacrylonitrile/SiO2 composites as an energy storage material, Carbon, 47 (2009) 3346-3354.

[52] T.H. Cho, M. Tanaka, H. Onishi, Y. Kondo, T. Nakamura, H. Yamazaki, S. Tanase, T. Sakai, Battery performances and thermal stability of polyacrylonitrile nano-fiber-based nonwoven separators for Li-ion battery, J Power Sources, 181 (2008) 155-160.

[53] S.S. Zhang, A review on the separators of liquid electrolyte Li-ion batteries, J Power Sources, 164 (2007) 351-364.

[54] R.H. Lv, Y. Zhu, H.S. Liu, B. Na, Y.H. Huang, X.L. Xie, Poly(vinylidene fluoride)/poly(acrylonitrile) blend fibrous membranes by centrifugal spinning for high-performance lithium ion battery separators, J Appl Polym Sci, 134 (2017).

[55] H. Lee, M. Yanilmaz, O. Toprakci, K. Fu, X.W. Zhang, A review of recent developments in membrane separators for rechargeable lithium-ion batteries, Energ Environ Sci, 7 (2014) 3857-3886.

[56] X.H. Rui, H.T. Tan, Q.Y. Yan, Nanostructured metal sulfides for energy storage, Nanoscale, 6 (2014) 9889-9924.

[57] M.V. Reddy, G.V.S. Rao, B.V.R. Chowdari, Metal Oxides and Oxysalts as Anode Materials for Li Ion Batteries, Chemical Reviews, 113 (2013) 5364-5457.

[58] D. J, Why do Li-ion Batteries die ? and how to improve the situation?, in: E.f. Science (Ed.), 2013.

[59] C.J. Wen, R.A. Huggins, Chemical Diffusion in Intermediate Phases in the Lithium-Silicon System, J Solid State Chem, 37 (1981) 271-278.

[60] C. Liang, M.X. Gao, H.G. Pan, Y.F. Liu, M. Yan, Lithium alloys and metal oxides as high-capacity anode materials for lithium-ion batteries, J Alloy Compd, 575 (2013) 246-256.

[61] D. Larcher, S. Beattie, M. Morcrette, K. Edstroem, J.C. Jumas, J.M. Tarascon, Recent findings and prospects in the field of pure metals as negative electrodes for Li-ion batteries, J Mater Chem, 17 (2007) 3759-3772.

[62] L. Zou, L. Gan, R.T. Lv, M.X. Wang, Z.H. Huang, F.Y. Kang, W.C. Shen, A film of porous carbon nanofibers that contain Sn/SnOx nanoparticles in the pores and its electrochemical performance as an anode material for lithium ion batteries, Carbon, 49 (2011) 89-95.

[63] S.L. P. Poizot, S. Grugeon, L. Dupont, J.-M. Tarascon, Nano-sized transition-metaloxides as negative-electrode materials for lithium-ion batteries, DOI ((2000)) 407

[64] X.H. Huang, J.P. Tu, B. Zhang, C.Q. Zhang, Y. Li, Y.F. Yuan, H.M. Wu, Electrochemical properties of NiO-Ni nanocomposite as anode material for lithium ion batteries, J Power Sources, 161 (2006) 541-544.

[65] X. Xu, W. Liu, Y. Kim, J. Cho, Nanostructured transition metal sulfides for lithium ion batteries: Progress and challenges, Nano Today, 9 (2014) 604-630.

[66] X.B. Hao, Y.C. Zeng, A Review on the Studies of Air Flow Field and Fiber Formation Process during Melt Blowing, Ind Eng Chem Res, 58 (2019) 11624-11637.

[67] V.A. Wente, Superfine Thermoplastic Fibers, Ind Eng Chem, 48 (1956) 1342-1346.

[68] X.S. Huang, Separator technologies for lithium-ion batteries, J Solid State Electr, 15 (2011) 649-662.

[69] J.N. Song, Z.W. Li, H. Wu, Blowspinning: A New Choice for Nanofibers, Acs Appl Mater Inter, 12 (2020) 33447-33464.

[70] T. Kikutani, J. Radhakrishnan, S. Arikawa, A. Takaku, N. Okui, X. Jin, F. Niwa, Y. Kudo, High-speed melt spinning of bicomponent fibers: Mechanism of fiber structure development in poly(ethylene terephthalate)/polypropylene system, J Appl Polym Sci, 62 (1996) 1913-1924.

[71] M. Naeimirad, A. Zadhoush, R. Kotek, R.E. Neisiany, S.N. Khorasani, S. Ramakrishna, Recent advances in core/shell bicomponent fibers and nanofibers: A review, J Appl Polym Sci, 135 (2018).

[72] M.A. Hunt, T. Saito, R.H. Brown, A.S. Kumbhar, A.K. Naskar, Patterned Functional Carbon Fibers from Polyethylene, Adv Mater, 24 (2012) 2386-2389.

[73] J. Sheng, S.H. Tong, Z.B. He, R.D. Yang, Recent developments of cellulose materials for lithium-ion battery separators, Cellulose, 24 (2017) 4103-4122.

[74] J.H. Zhao, W.Q. Han, H.D. Chen, M. Tu, R. Zeng, Y.F. Shi, Z.G. Cha, C.R. Zhou, Preparation, structure and crystallinity of chitosan nano-fibers by a solid-liquid phase separation technique, Carbohyd Polym, 83 (2011) 1541-1546.

[75] L.M. He, Y.Q. Zhang, X. Zeng, D.P. Quan, S. Liao, Y.S. Zeng, J. Lu, S. Ramakrishna, Fabrication and characterization of poly(L-lactic acid) 3D nanofibrous scaffolds with controlled architecture by liquid-liquid phase separation from a ternary polymer-solvent system, Polymer, 50 (2009) 4128-4138.

[76] J.T. Jung, J.F. Kim, H.H. Wang, E. di Nicolo, E. Drioli, Y.M. Lee, Understanding the non-solvent induced phase separation (NIPS) effect during the fabrication of microporous PVDF membranes via thermally induced phase separation (TIPS), J Membrane Sci, 514 (2016) 250-263.

[77] Q.Y. Wu, H.Q. Liang, L. Gu, Y. Yu, Y.Q. Huang, Z.K. Xu, PVDF/PAN blend separators via thermally induced phase separation for lithium ion batteries, Polymer, 107 (2016) 54-60.

[78] H.S. Jeong, D.W. Kim, Y.U. Jeong, S.Y. Lee, Effect of phase inversion on microporous structure development of Al2O3/poly(vinylidene fluoride-hexafluoropropylene)-based ceramic composite separators for lithium-ion batteries, J Power Sources, 195 (2010) 6116-6121.

[79] L.P. Liu, Z. Wang, Z.K. Zhao, Y.J. Zhao, F. Li, L.B. Yang, PVDF/PAN/SiO2 polymer electrolyte membrane prepared by combination of phase inversion and chemical reaction method for lithium ion batteries, J Solid State Electr, 20 (2016) 699-712.

[80] V. Kleivaite, R. Milasius, Electrospinning-100 Years of Investigations and Still Open Questions of Web Structure Estimation, Autex Res J, 18 (2018) 398-404.

[81] W.E. Teo, S. Ramakrishna, A review on electrospinning design and nanofibre assemblies, Nanotechnology, 17 (2006) R89-R106.

[82] M. Abrigo, S.L. McArthur, P. Kingshott, Electrospun Nanofibers as Dressings for Chronic Wound Care: Advances, Challenges, and Future Prospects, Macromol Biosci, 14 (2014) 772-792.

[83] C.J. Luo, S.D. Stoyanov, E. Stride, E. Pelan, M. Edirisinghe, Electrospinning versus fibre production methods: from specifics to technological convergence, Chem Soc Rev, 41 (2012) 4708-4735.

[84] J.W. Jung, C.L. Lee, S. Yu, I.D. Kim, Electrospun nanofibers as a platform for advanced secondary batteries: a comprehensive review, J Mater Chem A, 4 (2016) 703-750.

[85] X.W. Zhang, Y. Lu, Centrifugal Spinning: An Alternative Approach to Fabricate Nanofibers at High Speed and Low Cost, Polym Rev, 54 (2014) 677-701.

[86] H. Jiang, Y.Q. Ge, K. Fu, Y. Lu, C. Chen, J.D. Zhu, M. Dirican, X.W. Zhang, Centrifugally-spun tin-containing carbon nanofibers as anode material for lithium-ion batteries, J Mater Sci, 50 (2015) 1094-1102.

[87] Z. Yang, H.D. Peng, W.Z. Wang, T.X. Liu, Crystallization Behavior of Poly(epsilon-caprolactone)/Layered Double Hydroxide Nanocomposites, J Appl Polym Sci, 116 (2010) 2658-2667.

[88] S. Padron, A. Fuentes, D. Caruntu, K. Lozano, Experimental study of nanofiber production through forcespinning, J Appl Phys, 113 (2013).

[89] J.Y. Lin, B. Ding, J.Y. Yu, Y. Hsieh, Direct Fabrication of Highly Nanoporous Polystyrene Fibers via Electrospinning, Acs Appl Mater Inter, 2 (2010) 521-528.

[90] V.A. Agubra, L. Zuniga, D. Flores, H. Campos, J. Villarreal, M. Alcoutlabi, A comparative study on the performance of binary SnO2/NiO/C and Sn/C composite nanofibers as alternative anode materials for lithium ion batteries, Electrochim Acta, 224 (2017) 608-621.

[91] V.A. Agubra, L. Zuniga, D. Flores, J. Villareal, M. Alcoutlabi, Composite Nanofibers as Advanced Materials for Li-ion, Li-O-2 and Li-S Batteries, Electrochim Acta, 192 (2016) 529-550.

[92] A. Mataz, The use of Fe3O4/Carbon composite fibers as anode materials in lithium ion batteries, MOJ Polymer Science, 2 (2018).

[93] E.S. Pampal, E. Stojanovska, B. Simon, A. Kilic, A review of nanofibrous structures in lithium ion batteries, J Power Sources, 300 (2015) 199-215.

[94] Y. Lu, Y. Li, S. Zhang, G.J. Xu, K. Fu, H. Lee, X.W. Zhang, Parameter study and characterization for polyacrylonitrile nanofibers fabricated via centrifugal spinning process, Eur Polym J, 49 (2013) 3834-3845.

[95] J.C. Guo, A. Sun, C.S. Wang, A porous silicon-carbon anode with high overall capacity on carbon fiber current collector, Electrochem Commun, 12 (2010) 981-984.

[96] X.S. Zhou, L.J. Wan, Y.G. Guo, Electrospun Silicon Nanoparticle/Porous Carbon Hybrid Nanofibers for Lithium-Ion Batteries, Small, 9 (2013) 2684-2688.

[97] M.S. Wang, W.L. Song, J. Wang, L.Z. Fan, Highly uniform silicon nanoparticle/porous carbon nanofiber hybrids towards free-standing high-performance anodes for lithium-ion batteries, Carbon, 82 (2015) 337-345.

[98] J.C. Guo, X.L. Chen, C.S. Wang, Carbon scaffold structured silicon anodes for lithium-ion batteries, J Mater Chem, 20 (2010) 5035-5040.

[99] H.R. Zhang, X.Y. Qin, J.X. Wu, Y.B. He, H.D. Du, B.H. Li, F.Y. Kang, Electrospun core-shell silicon/carbon fibers with an internal honeycomb-like conductive carbon framework as an anode for lithium ion batteries, J Mater Chem A, 3 (2015) 7112-7120.

[100] H.C. Tao, L.Y. Xiong, S.C. Zhu, X.L. Yang, L.L. Zhang, Flexible binder-free reduced graphene oxide wrapped Si/carbon fibers paper anode for high-performance lithium ion batteries, Int J Hydrogen Energ, 41 (2016) 21268-21277.

[101] H.L. Lv, S. Qiu, G.X. Lu, Y. Fu, X.Y. Li, C.X. Hu, J.R. Liu, Nanostructured Antimony/carbon Composite Fibers as Anode Material for Lithium-ion Battery, Electrochim Acta, 151 (2015) 214-221.

[102] M. Inukai, A. Valdez, L. Zuniga, M. Alcoutlabi, Forcespinning: An alternative method to produce Metal-oxides/Carbon composite fibers as anode materials for Lithium-ion batteries, Ecs Transactions, 77 (2017) 383-390.

[103] J.V. A. Valdez, L. Zuniga, M. Alcoutlabi, MoS2 and MoO2 loaded Carbon Microfibers as Anode Materials for LithiumIon and Sodium-Ion Batteries.

[104] H.L. Lyu, J.R. Liu, S. Qiu, Y.H. Cao, C.X. Hu, S.M. Guo, Z.H. Guo, Carbon composite spun fibers with in situ formed multicomponent nanoparticles for a lithium-ion battery anode with enhanced performance, J Mater Chem A, 4 (2016) 9881-9889.

[105] J. Lopez, J. Villarreal, J. Cantu, J. Parsons, M. Alcoutlabi, Metal Sulfide/Carbon Composite fibers as Anode Materials for Lithium Ion Batteries, Selected Proceedings from the 233rd Ecs Meeting, 85 (2018) 275-284.

[106] Y.R. Liang, W.H. Lai, Z.C. Miao, S.L. Chou, Nanocomposite Materials for the Sodium-Ion Battery: A Review, Small, 14 (2018).

[107] H.S. Hou, X.Q. Qiu, W.F. Wei, Y. Zhang, X.B. Ji, Carbon Anode Materials for Advanced Sodium-Ion Batteries, Adv Energy Mater, 7 (2017).

[108] V. Deimede, C. Elmasides, Separators for Lithium-Ion Batteries: A Review on the Production Processes and Recent Developments, Energy Technol-Ger, 3 (2015) 453-468.

[109] J.F. Huang, Z.W. Xu, L.Y. Cao, Q.L. Zhang, H.B. Ouyang, J.Y. Li, Tailoring MoO2/Graphene Oxide Nanostructures for Stable, High-Density Sodium-Ion Battery Anodes, Energy Technol-Ger, 3 (2015) 1108-1114.

[110] H. Jia, M. Dirican, C. Aksu, N. Sun, C. Chen, J.D. Zhu, P. Zhu, C.Y. Yan, Y. Li, Y.Q. Ge, J.S. Guo, X.W. Zhang, Carbon-enhanced centrifugally-spun SnSb/carbon microfiber composite as advanced anode material for sodium-ion battery, J Colloid Interf Sci, 536 (2019) 655-663.

[111] H. Jia, M. Dirican, J.D. Zhu, C. Chen, C.Y. Yan, P. Zhu, Y. Li, J.S. Guo, Y. Caydamli, X.W. Zhang, High-performance SnSb@rGO@CMF composites as anode material for sodium-ion batteries through high-speed centrifugal spinning, J Alloy Compd, 752 (2018) 296-302.

[112] Y. Lu, M. Yanilmaz, C. Chen, M. Dirican, Y.Q. Ge, J.D. Zhu, X.W. Zhang, Centrifugally Spun SnO2 Microfibers Composed of Interconnected Nanoparticles as the Anode in Sodium-Ion Batteries, Chemelectrochem, 2 (2015) 1947-1956.

[113] Y. Lu, K. Fu, J.D. Zhu, C. Chen, M. Yanilmaz, M. Dirican, Y.Q. Ge, H. Jiang, X.W. Zhang, Comparing the structures and sodium storage properties of centrifugally spun SnO2 microfiber anodes with/without chemical vapor deposition, J Mater Sci, 51 (2016) 4549-4558.

[114] Z. Liu, T. Song, J.H. Kim, Z.P. Li, J. Xiang, T. Lu, U. Paik, Partially reduced SnO2 nanoparticles anchored on carbon nanofibers for high performance sodium-ion batteries, Electrochem Commun, 72 (2016) 91-95.

[115] H.K. Wang, Q.Z. Wu, D.X. Cao, X. Lu, J.K. Wang, M.K.H. Leung, S.D. Cheng, L. Lu, C.M. Niu, Synthesis of SnSb-embedded carbon-silica fibers via electrospinning: Effect of TEOS on structural evolutions and electrochemical properties, Mater Today Energy, 1-2 (2016) 24-32.

[116] H.M. Golecki, H.Y. Yuan, C. Glavin, B. Potter, M.R. Badrossamay, J.A. Goss, M.D. Phillips, K.K. Parker, Effect of Solvent Evaporation on Fiber Morphology in Rotary Jet Spinning, Langmuir, 30 (2014) 13369-13374.

[117] C.K. Liu, Y. Feng, H.J. He, J. Zhang, R.J. Sun, M.Y. Chen, Effect of carbonization temperature on properties of aligned electrospun polyacrylonitrile carbon nanofibers, Mater Design, 85 (2015) 483-486.

[118] C.J. Liu, E. Bonaccurso, H.J. Butt, Evaporation of sessile water/ethanol drops in a controlled environment, Phys Chem Chem Phys, 10 (2008) 7150-7157.

[119] R.W. Kugel, Raoult's law: Binary liquid-vapor phase diagrams - A simple physical chemistry experiment, J Chem Educ, 75 (1998) 1125-1129.

[120] P.J. Flory, Priciples of Polymer Chemestry, Cornell University Press1953.

[121] S.J. Hawkes, Raoult's Law Is a Deception, 72.

[122] L.Y. Ren, R. Ozisik, S.P. Kotha, P.T. Underhill, Highly Efficient Fabrication of Polymer Nanofiber Assembly by Centrifugal Jet Spinning: Process and Characterization, Macromolecules, 48 (2015) 2593-2602.

[123] X.Q. Wang, A.S. Mujumdar, A Review on Nanofluids - Part Ii: Experiments and Applications, Braz J Chem Eng, 25 (2008) 631-648.

[124] M. Dumitrascu, V. Meltzer, E. Sima, M. Virgolici, M.G. Albu, A. Ficai, V. Moise, R. Minea, C. Vancea, A. Scarisoreanu, F. Scarlat, Characterization of Electron Beam Irradiated Collagen-Polyvinylpyrrolidone (Pvp) and Collagen-Dextran (Dex) Blends, Dig J Nanomater Bios, 6 (2011) 1793-1803.

[125] I.M. Alibe, K.A. Matori, H.A. Sidek, Y. Yaakob, U. Rashid, A.M. Alibe, M.H.M. Zaid, S. Nasir, M.M. Nasir, Effects of polyvinylpyrrolidone on structural and optical properties of willemite semiconductor nanoparticles by polymer thermal treatment method, J Therm Anal Calorim, 136 (2019) 2249-2268.

[126] D.M. Chipara, A.C. Chipara, M. Chipara, Raman Spectroscopy of Carbonaceous Materials: A Concise Review, Spectroscopy-Us, 26 (2011) 42-47.

[127] M.S. Dresselhaus, G. Dresselhaus, R. Saito, A. Jorio, Raman spectroscopy of carbon nanotubes, Phys Rep, 409 (2005) 47-99.

[128] O. Keri, P. Bardos, S. Boyadjiev, T. Igricz, Z.K. Nagy, I.M. Szilagyi, Thermal properties of electrospun polyvinylpyrrolidone/titanium tetraisopropoxide composite nanofibers, J Therm Anal Calorim, 137 (2019) 1249-1254.

[129] L.W. Ji, O. Toprakci, M. Alcoutlabi, Y.F. Yao, Y. Li, S. Zhang, B.K. Guo, Z. Lin, X.W. Zhang, alpha-Fe2O3 Nanoparticle-Loaded Carbon Nanofibers as Stable and High-Capacity Anodes for Rechargeable Lithium-Ion Batteries, Acs Appl Mater Inter, 4 (2012) 2672-2679.

[130] W. Li, M. Zhou, H.M. Li, K.L. Wang, S.J. Cheng, K. Jiang, A high performance sulfur-doped disordered carbon anode for sodium ion batteries, Energ Environ Sci, 8 (2015) 2916-2921.

[131] N. Sun, H. Liu, B. Xu, Facile synthesis of high performance hard carbon anode materials for sodium ion batteries, J Mater Chem A, 3 (2015) 20560-20566.

[132] X. Zhang, P.S. Kumar, V. Aravindan, H.H. Liu, J. Sundaramurthy, S.G. Mhaisalkar, H.M. Duong, S. Ramakrishna, S. Madhavi, Electrospun TiO2-Graphene Composite Nanofibers as a Highly Durable Insertion Anode for Lithium Ion Batteries, J Phys Chem C, 116 (2012) 14780-14788.

[133] Y.H. Xu, Y.J. Zhu, Y.H. Liu, C.S. Wang, Electrochemical Performance of Porous Carbon/Tin Composite Anodes for Sodium-Ion and Lithium-Ion Batteries, Adv Energy Mater, 3 (2013) 128-133.

[134] X.J. Bai, B. Wang, H.P. Wang, J.M. Jiang, Preparation and electrochemical properties of profiled carbon fiber-supported Sn anodes for lithium-ion batteries, J Alloy Compd, 628 (2015) 407-412.

[135] Q.C. Zhuang, X.Y. Qiu, S.D. Xu, Y.H. Qiang, S.G. Sun, Diagnosis of Electrochemical Impedance Spectroscopy in Lithium-Ion Batteries, Lithium Ion Batteries - New Developments, DOI Book_Doi 10.5772/1358(2012) 189-226.

[136] B.A. Mei, O. Munteshari, J. Lau, B. Dunn, L. Pilon, Physical Interpretations of Nyquist Plots for EDLC Electrodes and Devices, J Phys Chem C, 122 (2018) 194-206.

APPENDIX A

APPENDIX A

HISTOGRAMS WITH LINEAR DISTRIBUTION & ELECTROCHEMICAL PERFORMACE
PLOTS FOR SUPPLEMENTAL CFs & COMPOSITE CFs IN LIBs & SIBs
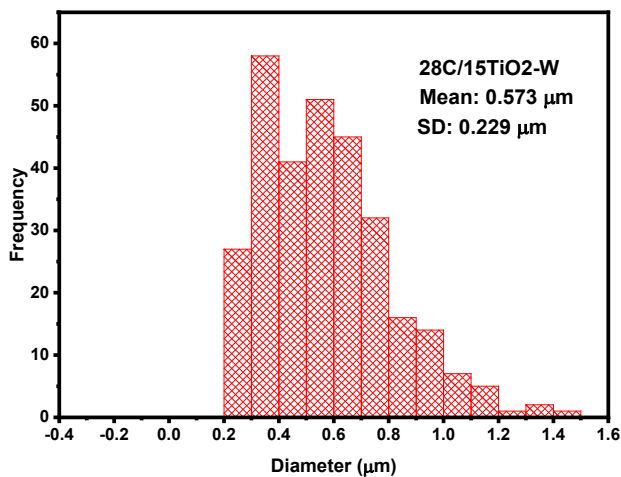
Figure A1: Histogram and linear distribution for 28C/15TiO$_2$-W composite carbon fibers.
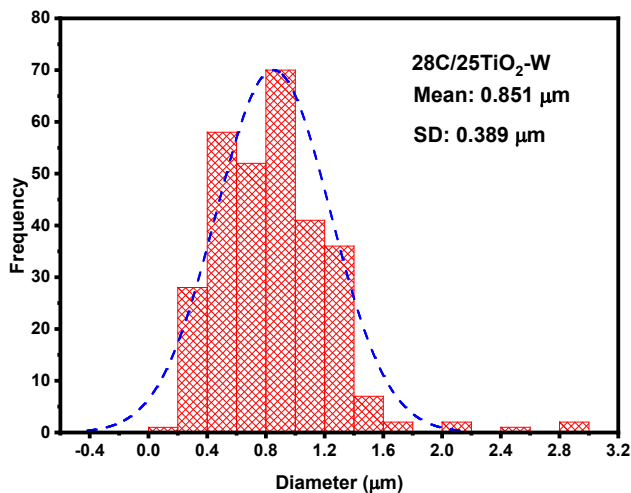
Figure A2: Histogram and linear distribution for 28C/25TiO$_2$-W composite carbon fibers
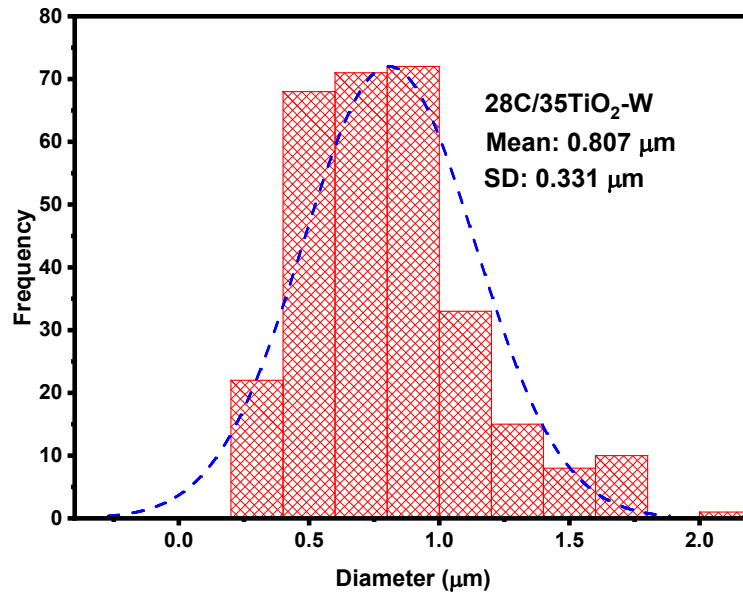
Figure A3: Histogram and linear distribution for 28C/35TiO₂-W composite carbon fibers.
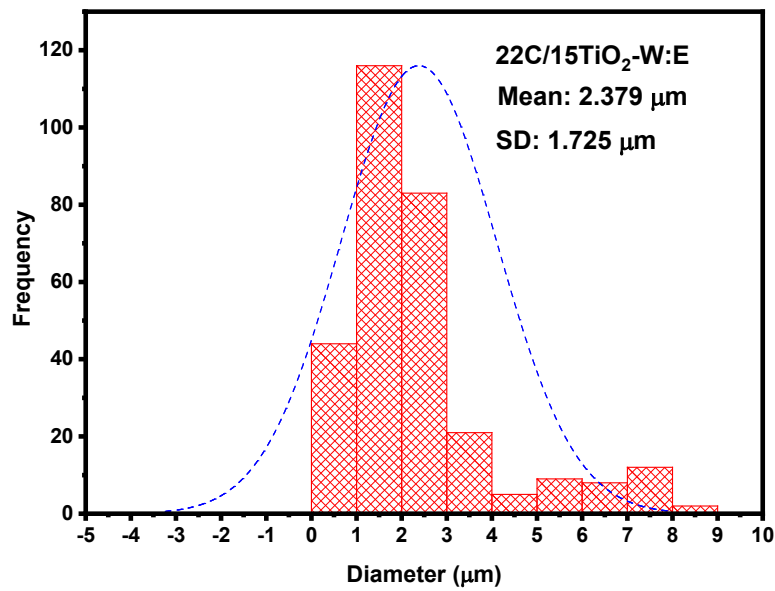
Figure A4: Histogram and linear distribution for 22C/15TiO₂-W:E composite carbon fibers.
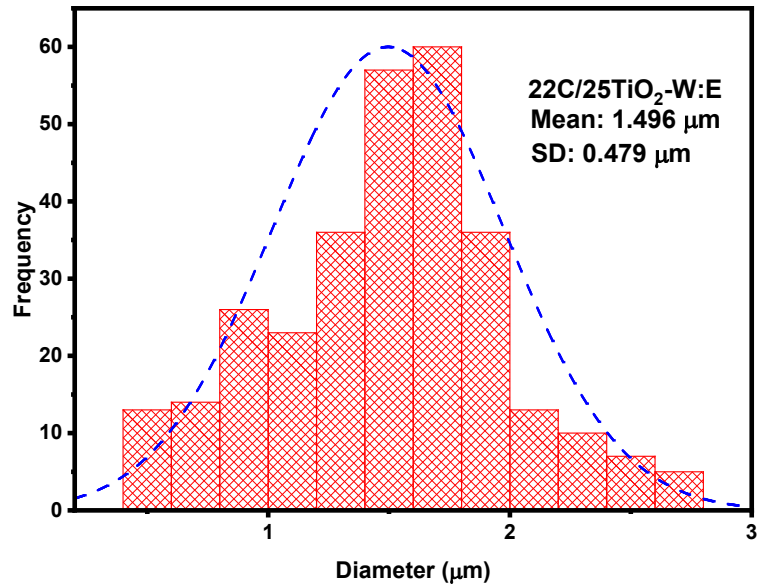
Figure A5: Histogram and linear distribution for 22C/25TiO₂-W:E composite carbon fibers.
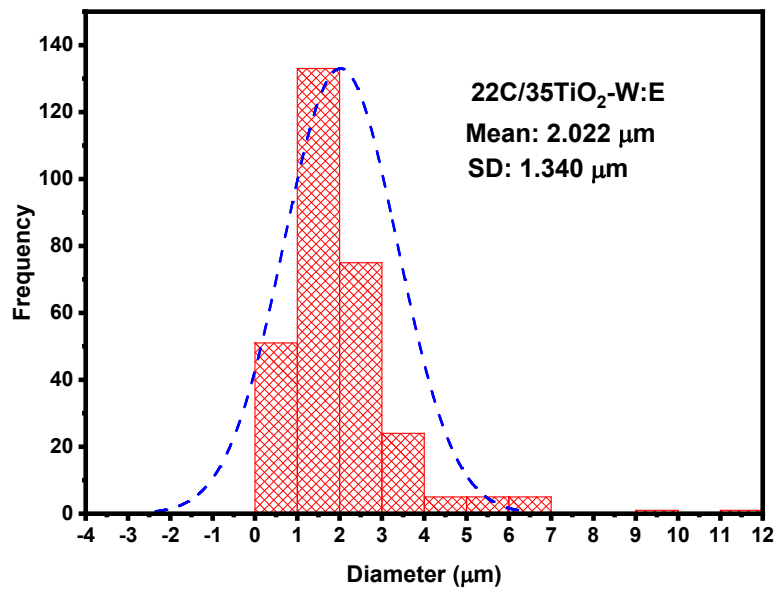
Figure A6: Histogram and linear distribution for 22C/35TiO₂-W:E composite carbon fibers.
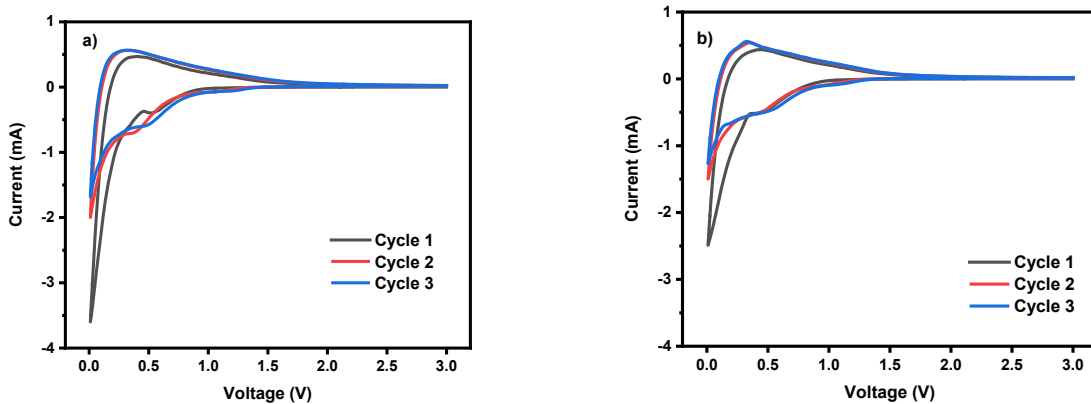
Figure A7. CVs for a) 20C-W and b) 28C-W carbon fiber anodes in Li-ion half cells
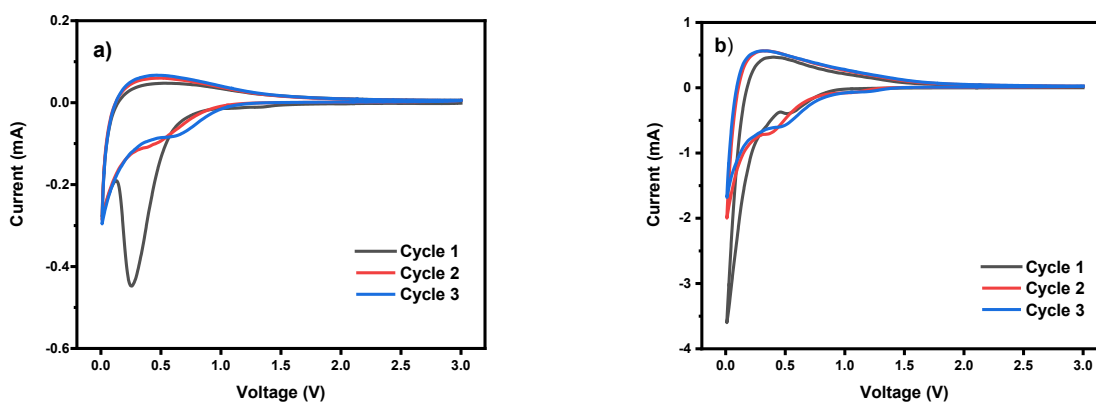
Figure A8. CVs for a) 20C-W and b) 28C-W carbon fiber anodes in Na-ion half cells
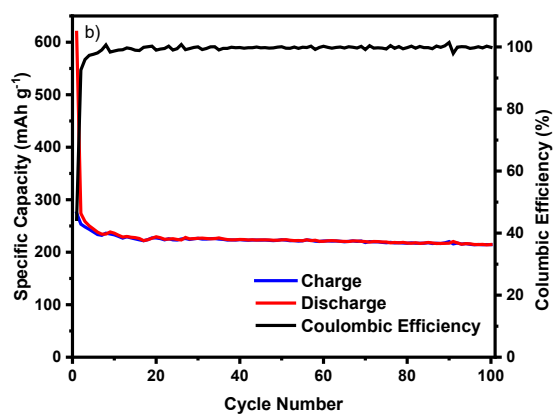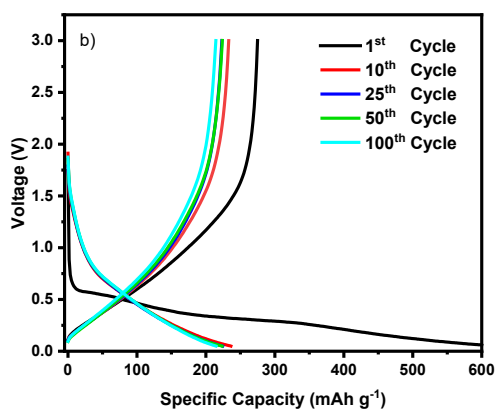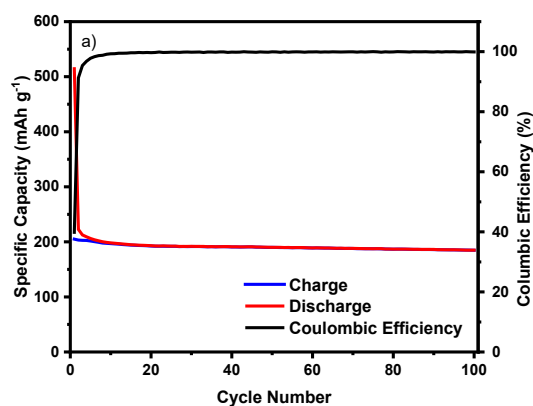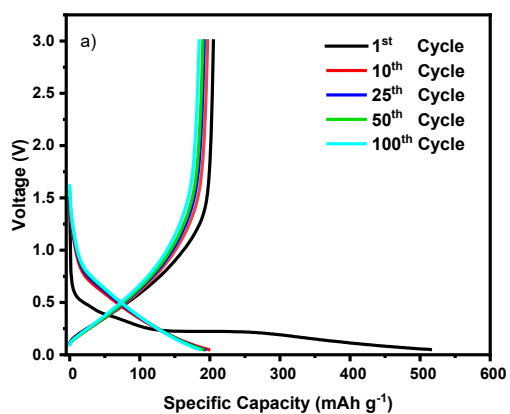
Figure A9. Charge-discharge plots and cycle performance for the a) 20C-W and b) 28C-W carbon-fiber anodes in Li-ion half cells
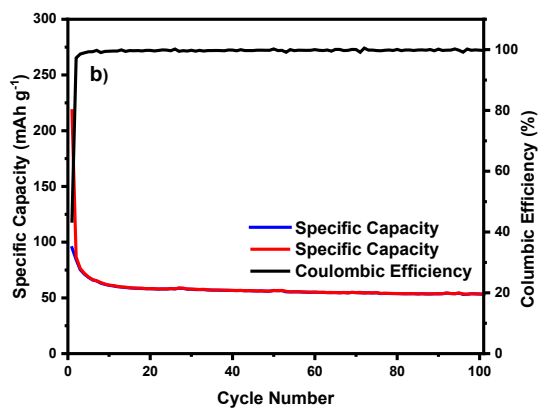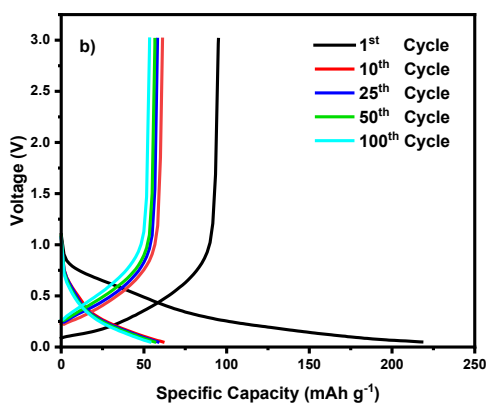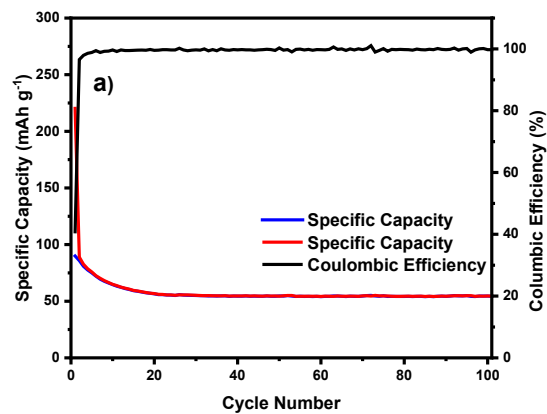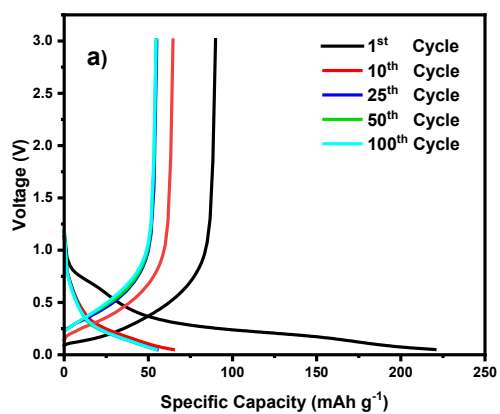
Figure A10. Charge-discharge plots and cycle performance for the a) 20C-W and b) 28C-W carbon-fiber anodes in Na-ion half cells
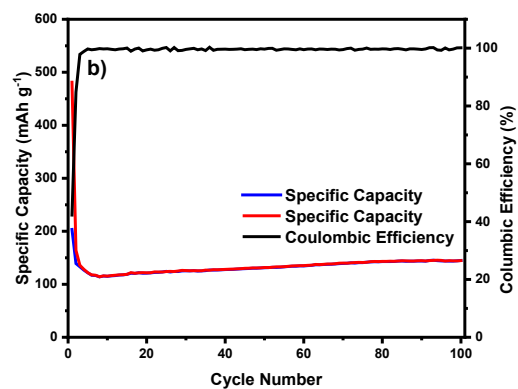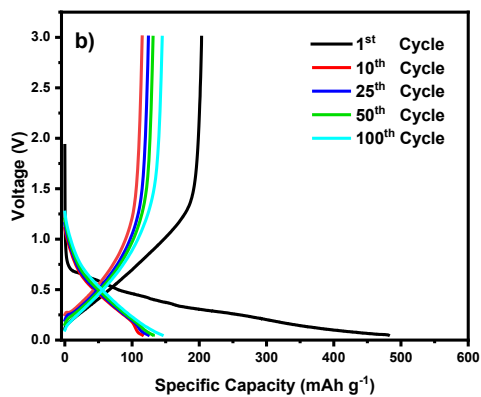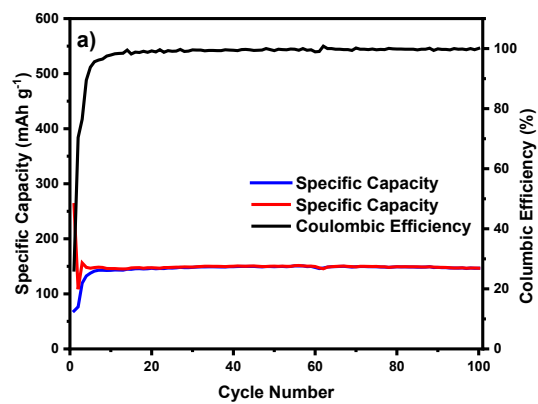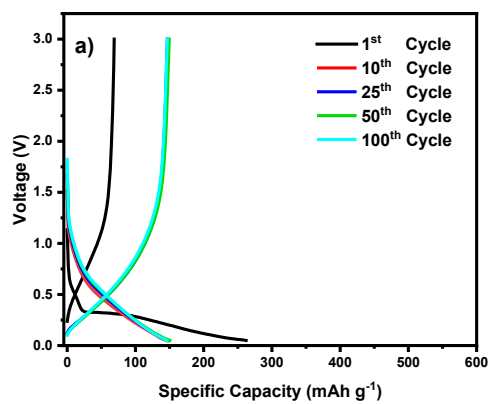
Figure A11. Charge-discharge plots and cycle performance for a) $28C/15TiO_2$-W and b)$28C/35TiO_2$-W composite carbon fibers in Li-ion half cells
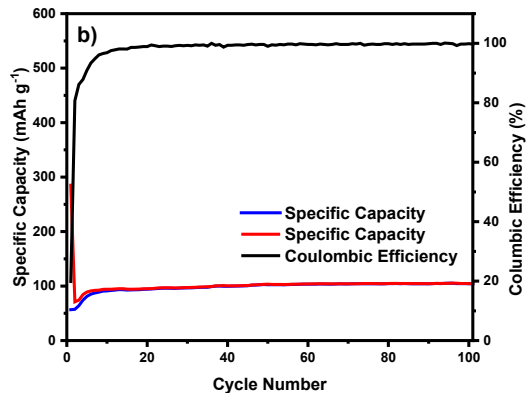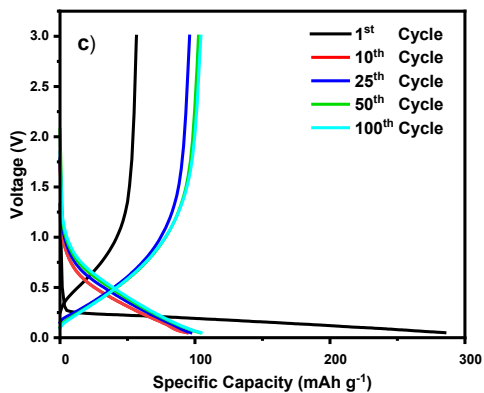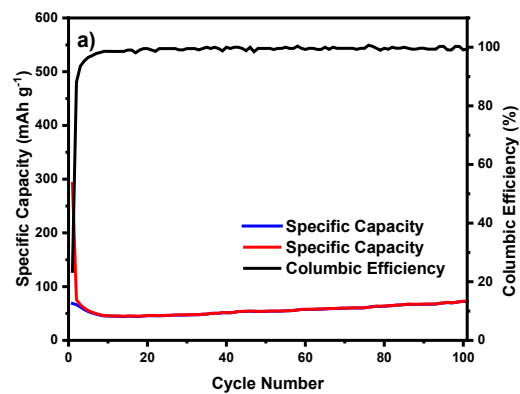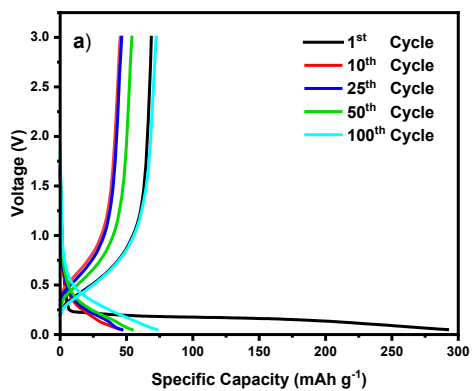
Figure A12. Charge-discharge plots and cycle performance for a) 22C/15TiO$_2$-W:E and b) 22C/35TiO$_2$-W:E composite carbon fibers in Li-ion half cells
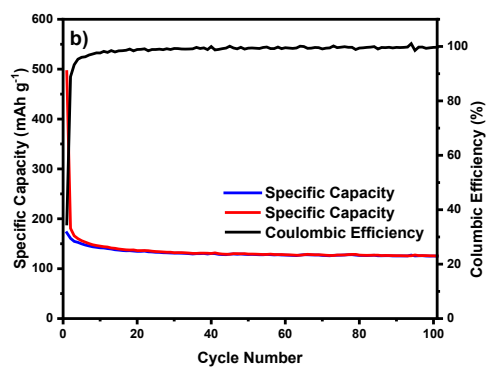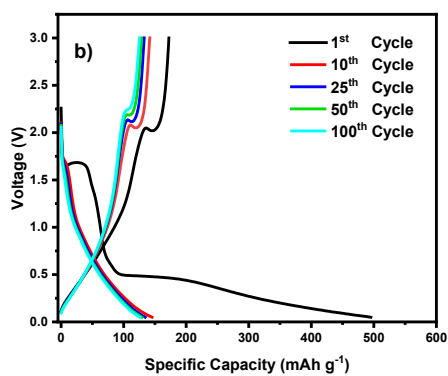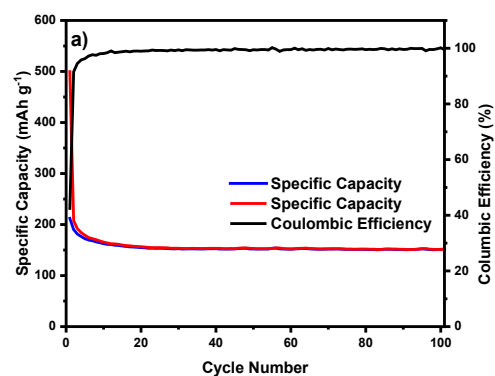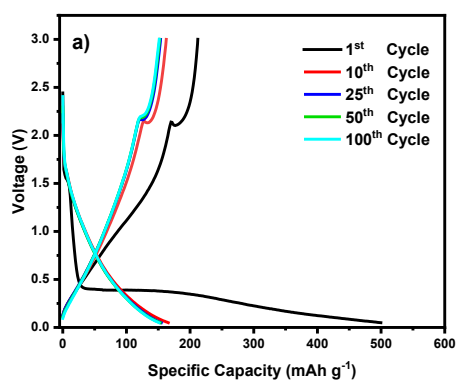
Figure A13. Charge-discharge plots and cycle performance for a) 12C/15TiO$_2$-E and b) 12C/35TiO$_2$-E composite carbon fibers in in Li-ion half cells

Table A1. State-of-the-Art Equipment

Equipment	Purpose	Results Obtained
DSC	Characterize the endothermic and exothermic peaks for my water-soluble fibers	The results were used to calculate the specific heat capacity of the fibers.
SEM/EDS	Used to characterize all materials prepared in this work	Morphology, fiber diameter, and elemental mapping
Forcespinning	Fabricate fibers	Multiple fiber mats used to produce carbon fiber anodes
TGA	Identifying the effect of annealing of fibers on their degradation rate during heat treatment.	The results showed that implementing annealing heat treatment before carbonization yielded more carbon fibers.
MBRAUN Glovebox	Controlling the environment during the battery assembly process	Production of LIB and SIB batteries
LANH	Cycle performance	Plotting up to 100 charge/discharge cycles on batteries.
BioLogic	Cyclic voltammetry (CV)	Used to identify the voltage at which the batteries' active materials go REDOX reaction and ionic diffusion.
Arbin	Rate performance	Charge/discharge cycles at different current rates to observe their delivered capacity.
NOVA	Impedance test	Used to identify the resistance to ion transport and the rate of ions diffusion

Table A2. State-of-the-Art Software

Software	Purpose	Results Obtained
ORIGIN	Plotting electrochemical results, histograms, and normal distribution for fiber diameter measurements.	CV, rate performance, cycle performance, and spectroscopy impedance, normal distribution for as-spun, annealed, and carbonized fibers.
EndNote	Managing and sorting citations in publications and thesis manuscript	Two publications as coauthor. One first-author publication and a review article as first-author
Adobe illustrator	Designing schematics for research papers	Schematics were included in publications and thesis manuscript.
Microsoft Word	Writing research papers/thesis	Two publications as coauthor. One first-author publication and a review article as first-author
PowerPoint	Preparing presentation material	Biweekly PowerPoint presentations to present to my advisor.
Excel	Organizing Data	Used to organize extracted data from electrochemical tests.
NOVA	Impedance Spectroscopy	Used to perform potential static impedance
ARBIN	Rate performance	Used to set up the different current rates and indicate the anode weight.
BT LAB	CV	Used to run the CV test on BioLogic.
LANH	Cycle performance	Used to set up cycle performance properties such as current density, number of cycles, rest or non-rest cycling, and formation cycles.

BIOGRAPHICAL SKETCH

Roberto Orrostieta Chavez was born in Huetamo, Michoacan, Mexico in 1994. However, he grew up in the neighboring state of Guerrero in a small city named Altamirano. Roberto is the youngest of four sons of Rodolfo Orrostieta and Eva Chavez. Roberto first stumbled upon engineering in his father's workshop. He became very curious about understanding how devices are built and how they function while working alongside his father during his childhood. It wasn't until Roberto attended high school that he became so fascinated with science and engineering as to pursue engineering at a higher academic level. Roberto moved to Morelia, Michoacan, Mexico to complete his high school coursework and attend a university there. Nevertheless, in the pursue of a better quality of life and education, Roberto move to the U.S.A in 2013 with the support of his siblings who resided there. Soon after arriving in the states, Roberto began his college education at the San Antonio Community College. After two years there, he transferred to The University of Texas at San Antonio where he received his B.S. in Mechanical engineering. Fortunately, Roberto was awarded a graduate assistantship at The University of Texas Rio Grande Valley to attend graduate school. Roberto earned a Master of Science in Mechanical Engineering from The University of Texas Rio Grande Valley in December 2020. There, Roberto became well versed in research procedures and galvanized his intention to pursue a Ph. D. in materials science & engineering at Texas A&M University where he aspires to continue growing as a role model student, scientist, engineer, leader, explorer, and friend. He can be reached at rochx360@gmail.com.